FLAW CRITICALITY OF CIRCULAR DISBOND DEFECTS IN COMPRESSIVE LAMINATES

1980-81 INTERIM REPORT

By

John D. Webster

Center for Composite Materials
University of Delaware
Newark, DE 19711

Sponsored by

National Aeronautics & Space Administration
Materials Division, Langley Research Center
Hampton, VA 23665

NSG 1304

June 1981

ABSTRACT

Inherent material flaws in composite laminates may result in substantial performance loss. The complex nature of this strength loss is influenced by several parameters including loading, laminate stacking sequence and thickness, flaw size, and defect type. These various effects have not, however, been fully characterized and hence there exists a need for establishing flaw criticality data. An experimental and analytical study of the compressive behavior of T300/5208 graphite/epoxy laminates containing circular delaminations is performed to determine the flaw criticality of two types of implanted defect, Kapton bag and Teflon film, on several laminate configurations: $[0/\pm45]_{2s}$, $[0/\pm45]_{s}$, $[90/\pm45]_{s}$ and $[\pm45]_{2s}$. Defect size is varied and results are presented in the form of residual strength curves. Results indicated that the Teflon film defect reduced strength more than the Kapton bag defect in the 12-ply samples, but that two laminates, $[\pm45]_{2s}$ and $[90/\pm45]_{s}$ were insensitive to any implanted defect. A clear thickness effect was shown to exist for the $[0/\pm45]_{ns}$ laminate and was attributed to failure mode transition. The analytically predicted buckling loads show excellent agreement with experimental results and are useful in predicting failure mode transition.

ACKNOWLEDGEMENTS

The work presented here was performed under the sponsorship of NASA Grant 1304, Mr. Jerry Deaton, Project Engineer. The contractor was the University of Delaware Center for Composite Materials, and Dr. R. Byron Pipes, Director of the Center, was the principal investigator.

TABLE OF CONTENTS

NOMENCLATURE

Symbol	Meaning
A	Buckling amplitude
A_{ij}	Elements of material extensional matrix
a	One half center span = 9.525 cm (3.75 in.)
B_{ij}	Elements of material coupling matrix
b	One half fixture outer span = 30.5 cm (12 in.)
D	Isotropic plate flexural stiffness
D_{ij}	Elements of material bending matrix
D^{*}_{ij}	Reduced stiffness approximation elements
D_{eff}	Effective buckling resistance
d_{Trans}	Failure mode transition diameter
E	Young's modulus
G_a	Strain energy release rate
h	Core height and average face thickness
M	Moment applied to test section
N_x , N_y , N_{xy}	In-plane stress resultants
P	Machine load
R	Defect radius
S	Rupture area

Symbol	Meaning
a	Area of disbond
T_1	Compressive face thickness
T_2	Tensile face thickness
$T_i u_i$	Work done by i-th component of surface traction
u , v , w	x, y and z displacements
u^o , v^o	Midplane displacements
V	Potential energy
W	Strain energy density
δ	Variation operator
ε'_x , ε'_y , ε'_{xy}	Midplane strains due to bending
γ	Fracture energy (Kachanov)
Γ_o	Fracture energy (Chai)
ν	Poisson's ratio
ω	Beam width

LIST OF FIGURES

LIST OF TABLES

CHAPTER 1

INTRODUCTION

The expanded application of fiber-reinforced composites in industry has created the need for accurate design information. With reliable information the designer can fully exploit the superior strength-to-weight and stiffness-to-weight ratios of today's advanced composites. Some parameters, such as tensile strength and elastic moduli, are easily determined by means of generally accepted test methods. Other properties, such as compressive strength, are often disputed as being functions of the method used in their measurement. Also, some information in areas such as long term exposure or fatigue is just recently becoming available due to the extended test time involved and the continual evolution of advanced composites. The unique multiphase construction of composite materials has also generated additional areas of concern and has made it necessary to tailor some test methods to evaluate these additional problems. One such technique is the use of a composite faced sandwich beam to examine the problem of flaw criticality in compressively loaded laminates containing interlaminar disbond defects.

1.1 Flaw Criticality

One area of concern to the composites designer is the subject of flaw criticality. Inherent material defects and defects induced by operating environment produce stress concentrations which reduce the effectiveness of a component to withstand design loads. If the effect of an internal flaw is such that the component can remain in service without compromising safety, then the damage is deemed noncritical or subcritical. Unfortunately, most operating environments encompass cyclic loading which encourages the growth of defects. When a flaw reaches such a magnitude that it can no longer be tolerated, it must be removed by an appropriate repair technology or the component must be replaced.

In order to determine when a flaw becomes critical an understanding of the factors which influence flaw growth must be developed. Ultrasonic and x-ray methods permit the detection and measurement of defects and growth but are often impractical as they are costly and time-consuming. Analytical techniques, based on fracture mechanics considerations and verified by experiments, must be developed to quantify damage tolerance.

A form of anomaly found in continuous fiber composites is the interlaminar defect. This defect is

characterized as a region of disbond between adjacent layers in a laminate. Interlaminar defects arise as "birth" defects in the fabrication process or may be a result of foreign object impact damage. In order to assess the effect of such flaws on structural performance, man-made defects of selected geometry are introduced into the laminate during fabrication. These laminates are then evaluated under various test conditions to develop a data base to quantify the disbond effect on performance.

In one analysis, developed by Husman, et al. [1] an analogy between damage generated by hard particle impact and damage inflicted by inserting a flaw of known dimensions is discussed. Results of an ongoing study on impact damage tolerance performed at the NASA Langley Research Center [2] support this analogy. The NASA report provides ultrasonic scans which clearly illustrate the impetus behind relating foreign object damage and the effect of implanted defects.

1.2 Sandwich Beam Compressive Test Method

In order to examine a large range of disbond sizes a test technique which involves a large test section must be employed; the sandwich beam is one such technique. The beam is loaded in four-point bending with the result being a state of uniform moment across the center span. The

sandwich panel is a structure which consists of two thin facesheets adhesively bonded to a thick, low density core. The facesheets may be of different materials with one often being high strength steel or titanium. The core is chosen for its low bending stiffness and high shear strength, and is most commonly constructed of expanded honeycomb. The core serves to separate the facesheets and provide support to prevent localized buckling. Under application of a bending moment the two facesheets resist bending by developing in-plane loads. For a reasonably deep sandwich beam ($\sim$4 cm) the variation of stress across the face thickness is negligible. Also, along the center span of a four-point bending geometry the shear force is zero. Shuart [3] has verified by finite element modeling that a state of uniform stress exists in the facesheets for a sandwich constructed with 38 mm (1.5 in.) thick, low density aluminum honeycomb core. The amount of load carried by the core was found to be negligible.

The sandwich beam test specimen represents one specialized component in a field of many applications; for a more complete treatment on the subject the author suggests the books by Plantema [4] and Allen [5].

The thrust of this work is an experimental program designed to evaluate the compressive performance of various

graphite/epoxy laminates containing interlaminar defects. The sandwich beam in four-point bending is utilized as the compressive test method. Also, since instability plays an important role in compressive performance, a Rayleigh-Ritz technique is used to approximate defect buckling loads. Orthotropic materials are considered and the added effects of bending-twisting coupling are accounted for by the use of the reduced bending stiffness approximation.

CHAPTER 2

ANALYSIS OF DELAMINATION BUCKLING

The failure of compression laminates with implanted interlaminar defects is intimately related with buckling fo the disbond. Prior to buckling the entire laminate supports the applied load and little interlaminar crack propagation occurs under static load. With the onset of disbond instability the portion of the laminate above the disbond exhibits reduced extensional stiffness and hence some portion of the load it carried will be transferred to the surrounding laminate. If the stable portion of the laminate cannot support this additional load, failure initiates in the form of stable or unstable crack propagation or catastrophic laminate failure.

2.1 Buckling Considerations

Calculation of the exact buckling load for the disbond geometry (shown in Figure 2.1) is not a trivial excercise. The problem at hand differs in two important respects from that analyzed by Timoshenko [6], Dym [7] or Chia [8]. First, a laminated material is considered, which in

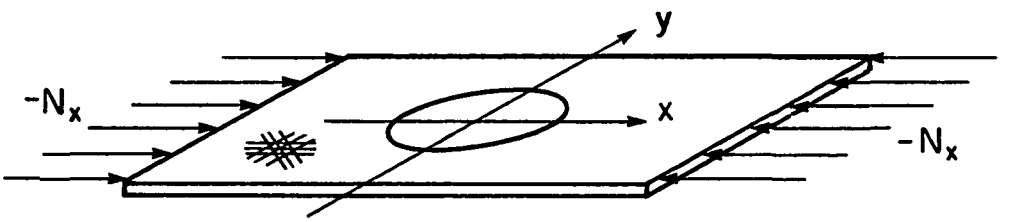

FIGURE 2.1 DISBOND LOAD GEOMETRY

Chia's terminology is rectilinearly orthotropic. That is, the material symmetry can be described in a rectangular Cartesian coordinate system. This precludes use of governing equations described in cylindrical coordinates. Also, since the region above the disbond represents only a portion of the laminate it is, in general, not balanced or symmetric and hence exhibits coupling effects. Secondly, the load geometry of interest is not purely radial, since the load is applied as an in-plane force in the "x" direction.

Two researchers, working independently, have produced solutions for nonuniform boundary loading. Durban [9] used an eigenfunction expansion and applied the Galerkin method to produce a stability formulation which then must be solved by numerical techniques. Along similar lines Yamaki [10] used a Rayleigh-Ritz procedure and produced comparable results for an example case, which both authors examined, of a disk loaded by two point loads. Unfortunately neither author included the possibility of anisotropic materials and hence that difficulty still presents itself.

2.2 Stationary Potential Energy

2.2.1 Development of Energy Equations

The potential energy of an elastic body neglecting body forces is [11]:

$$V = \int_{\text{Volume}} W dV - \int_{\text{Surface}} T_i u_i dS \tag{2.1}$$

where W is the strain energy density function:

$$W = \tfrac{1}{2}(\sigma_x \varepsilon_x + \sigma_y \varepsilon_y + \sigma_z \varepsilon_z + \sigma_{xy} \varepsilon_{xy} + \sigma_{xz} \varepsilon_{xz} + \sigma_{yz} \varepsilon_{yz}) \tag{2.2}$$

and $T_i u_i$ represents the work done by the i-th component of the surface traction.

In solving the stability problem the theorem of minimum potential energy is used to determine the condition of equilibrium between the potential energy due to bending and that due to in-plane loads. This relationship can be expressed as

$$\delta V = 0 \tag{2.3}$$

which implies that the functional V is stationary.

The potential energy due to the in-plane loads is

$$\int_{\text{Surface}} T_i u_i dS = \int_{\text{Surface}} (N_x \varepsilon'_x + N_y \varepsilon'_y + N_{xy} \varepsilon'_{xy}) dS \tag{2.4}$$

where N_x , N_y , N_{xy} are the applied in-plane loads and ε'_x , ε'_y , ε'_{xy} are the midplane strains due to bending.

$$\begin{aligned} \varepsilon'_x &= \tfrac{1}{2}(\partial w/\partial x)^2 \\ \varepsilon'_y &= \tfrac{1}{2}(\partial w/\partial y)^2 \\ \varepsilon'_{xy} &= \frac{\partial w}{\partial x}\frac{\partial w}{\partial y} \end{aligned} \tag{2.5}$$

"w" is the out-of-plane displacement. Hence the potential energy due to in-plane loads is:

$$\int_{\text{Surface}} T_i u_i dA = \tfrac{1}{2}\int_{\text{Surface}} \left[N_x\left(\frac{\partial w}{\partial x}\right)^2 + N_y\left(\frac{\partial w}{\partial y}\right)^2 + 2N_{xy}\left(\frac{\partial w}{\partial x}\frac{\partial w}{\partial y}\right)\right] dS \tag{2.6}$$

The strain energy density (Eq. 2.2) can be written in terms of displacements by using the strain-displacement equations and the constitutive equations for an anisotropic plate [12]. The potential energy can be expressed as:

$$\begin{aligned} V = \tfrac{1}{2}\iint_{\text{Surface}} \Big(& A_{11}u_x^{o\,2} - 2A_{12}u_x^o v_y^o + A_{22}v_y^{o\,2} \\ & + 2A_{16}(u_x^o u_y^o + u_x^o v_x^o) + 2A_{26}(v_y^o u_y^o + v_y^o v_x^o) \\ & + A_{66}(u_y^o + v_x^o)^2 - B_{11}u_x^o w_{xx} \\ & - 2B_{12}(v_y^o w_{xx} + u_x^o w_{yy}) - B_{22}v_y^o w_{yy} \\ & - 2B_{16}(u_y^o w_{xx} + v_x^o w_{xx} + 2u_x^o w_{xy}) \\ & - 2B_{26}(u_y^o w_{yy} + v_x^o w_{yy} + 2v_y^o w_{xy}) \\ & - 4B_{66}(u_y^o w_{xy} + v_x^o w_{xy}) \\ & + D_{11}w_{xx}^2 + 2D_{12}w_{xx}w_{yy} + D_{22}w_{yy}^2 \\ & + 4D_{16}w_{xx}w_{xy} + 4D_{26}w_{yy}w_{xy} + 4D_{66}w_{xy}^2 \\ & + N_x w_x^2 + N_y w_y^2 + 2N_{xy}w_x w_y \Big) dS \end{aligned} \tag{2.7}$$

$$= \text{Stationary Value}$$

where u^o and v^o are midplane displacements and subscripts on u, v, w denote respective partial derivatives.

In determining buckling loads by the Rayleigh-Ritz technique variation with respect to the undetermined displacement amplitudes of the assumed deflection function is required. When performing the variation the terms involving only midplane strains (terms multiplied by elements of the $[A_{ij}]$ matrix) represent a constant and hence vanish. The coupling terms, represented by terms involving the $[B_{ij}]$ matrix, remain and add considerable complexity to the solution. It is important to account for these coupling effects because an interlaminar defect of the geometry considered divides the laminate into two half plates, each of which is unsymmetric.

An approximate method, discussed by Ashton and Whitney [13] is the reduced bending stiffness approximation. In this method the coupling effects are absorbed into the bending stiffness matrix by the transformation

$$[D]^* = [D] - [B][A]^{-1}[B] \tag{2.8}$$

where [A], [B] and [D] are the constitutive matrices [14] and $[D]^*$ is the reduced stiffness matrix. Employing this technique the expression for the potential energy becomes:

$$V = \tfrac{1}{2}\int_S \Big[D_{11}^* w_{xx}^2 + 2D_{12}^* w_{xx} w_{yy} + D_{22}^* w_{yy}^2 + 4D_{16}^* w_{xx} w_{xy} + 4D_{26}^* w_{yy} w_{xy} + 4D_{66}^* w_{xy}^2 + N_x w_x^2 + N_y w_y^2 + 2N_{xy} w_x w_y \Big] dS \qquad (2.9)$$

= Stationary Value

The particular problem of interest involves a single in-plane load N_x. The remaining in-plane loads are retained in order to check the approximate results with exact solutions.

2.2.2 Buckling of an Isotropic Disk Under a Uniaxial Load Using a Rayleigh-Ritz Approximation

For an isotropic material no coupling exists; hence

$$[D^*] = [D] \qquad (2.10)$$

and

$$D_{16} = D_{26} = 0 \qquad (2.11)$$

By comparing elements of the stiffness matrix, we have for an isotropic material

$$D_{11} = D_{22} = D$$
$$D_{12} = \nu D \qquad (2.12)$$
$$D_{66} = \frac{(1-\nu)}{2} D$$

where D is the plate flexural stiffness:

$$D = \frac{Eh^3}{12(1-\nu^2)} \tag{2.13}$$

Inserting Equations 2.12 into the energy expression (Eq. 2.9) yields the familiar form of the potential energy for an isotropic plate with a single in-plane load.

$$\tfrac{1}{2}\int_S \Big\{ D[(w_{xx}+w_{yy})^2 - 2(1-\nu)(w_{xx}w_{yy}-w_{xy}^2)] + [N_x w_x^2] \Big\} dS = \text{Constant} \tag{2.14}$$

The Rayleigh-Ritz method involves selecting an expression for the out-of-plane deflection, computing the necessary derivatives, and inserting them into the energy equation (Eq. 2.14). We then integrate and take the variation with respect to the unknown amplitude coefficients. This yields an approximate form for the critical buckling load. The accuracy of the method is dependent on the accuracy of the assumed form of deflection. If the actual deflection shape is inserted into the energy equation, the exact buckling load is computed. In general, however, the exact form of the solution is not known and hence a form is sought which satisfies the geometric boundary conditions and includes any obvious symmetries. The variation of the

energy is actually zero only when the deflection form is exact; any other approximate form yields critical values greater than the true value.

The geometric boundary conditions for this problem are:

$$w(R) = 0$$
$$\frac{\partial w(R)}{\partial r} = 0 \tag{2.15}$$

where R is the plate radius. A deflection of the form

$$w(r) = A\left[1 - \left(\frac{r}{R}\right)^2\right]^2 \tag{2.16}$$

satisfies the boundary conditions and should provide a reasonable result. Equation 2.16 is plotted in Figure 2.2 where A represents the undetermined amplitude. The deflection is assumed axisymmetric as experimental observations indicate that no extensive asymmetries exist. No measurements however were obtained to validate this hypothesis.

Looking ahead to the orthotropic extension, Eq. 2.16 is more conveniently expressed in Cartesian form

$$w(x,y) = A\left[1 - \left(\frac{x^2+y^2}{R^2}\right)\right]^2 \tag{2.17}$$

Page Intentionally Left Blank

Calculating appropriate derivatives, inserting them in the energy equation (Eq. 2.15) and integrating yields

$$N_{x_{crit}} = \frac{-32D}{R^2} \tag{2.18}$$

Details of the derivation are shown in Appendix A.

In an effort to validate the usefulness of Eq. 2.18 another simple case of biaxial compression ($N_x = N_y$) was examined. This load geometry is illustrated in Figure 2.3b. The same boundary conditions are retained. If we consider the resultant force acting on the curved boundary of the circular plate the biaxial loading corresponds to pure radial compression of the disk. This problem is solved in most stability texts such as [15] and the solution is given as

$$N_{R_{crit}} = \frac{-14.68D}{R^2} \tag{2.19}$$

By comparison the Rayleigh-Ritz technique yields

$$N_{R_{crit}} = \frac{-16D}{R^2} \tag{2.20}$$

which is nine percent greater than the exact value.

The fact that the critical load for the biaxial case is one half the result for the uniaxial case is a result of

Page Intentionally Left Blank

symmetric nature of the assumed deflection shape. The relatively good accuracy in the biaxial case does not ensure comparative accuracy in the uniaxial case as is evident in another set of examples examined by Timoshenko [16]. That author calculated the results for the square plate with clamped edges (see Figure 2.4a). The result for the biaxial loading was

$$N_{x_{crit}} = \frac{5.33\pi^2 D}{a^2} \tag{2.21}$$

which was only one percent from the exact solution. And similarly (due to the symmetry of the assumed deflection):

$$N_{x_{crit}} = \frac{10.67\pi^2 D}{a^2} \tag{2.22}$$

for the uniaxial case (Figure 2.4b) which varies from the exact solution of

$$N_{x_{cr\text{-}exact}} = \frac{10.07\pi^2 D}{a^2} \tag{2.23}$$

by six percent.

In principle the accuracy of the current predictions can be improved by adding to the form of the deflection, but each incremental improvement is usually the result of monumental increases in algebraic manipulation. Other techniques

Page Intentionally Left Blank

including series expressions for the deflection and the Galerkin method are commonly used in the solution of stability problems, but as a first estimate for design purposes a deflection form as given in Equation 2.17 will suffice.

2.2.3 Buckling of Disk Under Uniaxial Load -- Extension to Orthotropic Plates

The form of out-of-plane deflection is now substituted into the energy equation (Eq. 2.9) directly. For uniaxial compression N_y and N_{xy} are zero. Upon performing the integrations for the chosen form of deflection the products $w_{xx}w_{xy}$ and $w_{yy}w_{xy}$ vanish; hence the critical buckling load has no dependence on D_{16}^* or D_{26}^*. After simplification:

$$N_{x_{crit}} = \frac{-24}{R^2}\left(\frac{D_{11}^*+D_{22}^*}{2} + \frac{D_{12}^*+2D_{66}^*}{3}\right) \tag{2.24}$$

To verify this result Equations 2.13 are substituted into Equation 2.24. This produces:

$$N_{x_{crit}} = \frac{-24}{R^2}\left(\frac{D + D}{2} + \frac{\nu D + [2(1-\nu)/2]D}{3}\right) = \frac{-32D}{R^2}$$

which is the result for the isotropic disk.

Equation 2.24 produces an approximate value for the critical buckling load for a generally constructed plate. The value of this information should not be discounted, as instability plays a central role in the failure process.

2.3 Fracture Mechanics Considerations

The next step in characterizing the failure of composites by delamination buckling is the analysis of the fracture which begins after the defect instability occurs. In order for the crack to propagate work of rupture is required. The problem of interest is the case where the region beneath the disbond maintains a uniform strain and remains flat when buckling of the exterior region occurs. This behavior occurs for sandwich structures if the core is sufficiently rigid to prevent deflection of the face-sheet which remains attached. For this case, Chai, et al. [17] suggest that the work of rupture is drawn from changes in stored strain energy caused by changes in delamination size. The Griffith criterion is applied to determine the condition for crack extension; that is, if the change in stored energy is greater than the amount of energy required to create a new unit of surface then growth occurs. The Griffith criterion is expressed as

$$G_a(\ell) > \Gamma_o \tag{2.26}$$

where G_a is the strain energy release rate which is a function of the defect dimensions and Γ_o is the fracture energy for the material. The stability of crack growth can be determined from an expression relating G_a to defect size and applied loading. Crack growth is unstable whenever G_a is greater than Γ_o. The growth, which initiates at buckling, may originally be unstable then become stable as the strain energy release rate reduces to the fracture energy or may remain unstable depending on the magnitude of the fracture energy.

Difficulties arise when one attempts to formulate expressions for the strain energy release rate for any but a few special geometries. For the problem of interest the circular disbond extends into an ellipse and hence requires a sophisticated formulation for G_a. Chai, et al. [18] illustrates the two-dimensional elliptical disbond geometry but then confines the analyses to a strip of unit width with delamination length, "ℓ". This geometry is shown in Figure 2.5. Implicit in Chai's analyses is the assumption that the crack propagation occurs along the direction of the load; experimental observations, however, indicate that this is not the initial response.

Page Intentionally Left Blank

The visual monitoring of the compressive face during experimental testing produces a fairly complete description of the crack propagation fallowing defect instability. The crack extension is illustrated in Figure 2.6 and begins with the buckled geometry. The crack initially extends transverse to the load along the centerline of the test section forming a debonded region in the shape of an ellipse. This ellipse extends, with continued loading, outward toward the sample free edges. When the free edges are encountered the crack continues to propagate but now moves parallel to the load direction. This process continues until the elliptical crack front has flattened forming a completely debonded rectangular strip across the entire test section. The debonded strip, which appears to be approximately equal in length to the original defect diameter, represents the geometry examined by Chai. Crack growth now occurs uniformly across the test section in line with what Chai's model suggests. It is the initial crack extension which is of primary interest and presents a considerable analytic challenge.

As Chai indicates, Kachanov [19] had previously addressed several thin film problems. Both Chai and Kachanov neglect the special multiphase laminated nature of composites and examine only isotropic problems. Kachanov does however present solutions for several geometries including the "thin film" case and the case of a disk under

Page Intentionally Left Blank

radial load. Kachanov's method, which equates energy in the initial state to that in the buckled state, allows one to calculate the critical stress necessary to cause buckling for a given geometry. If no delamination exists initially then a rupture work term is involved. For the special case where a delamination is already present then Kachanov's cataloged results produce the classic buckling loads. Although Kachanov does not examine the problem of crack extension he does address the problem by suggesting the use of Griffith's criterion, which he expresses as

$$\frac{\partial V}{\partial S} = 2\gamma \tag{2.27}$$

where V is the potential energy of the buckled layers, S is the area of rupture, and γ is the fracture energy. Application of this technique remains a considerable challenge for complicated geometries.

A second difficulty in the application of the fracture mechanics approach is the availability of information about the fracture energy, γ. The fracture energy represents the work necessary to create a unit of new surface and for most materials is constant. The complex construction of composite laminates, however, may require development of functional relationships between fracture energy and laminate construction details. If information is

unavailable an experimental evaluation of the rupture energy can be performed but should be conducted with identical material to that used in the remainder of any experimental program.

CHAPTER 3

EXPERIMENTAL PROGRAM

The experimental program consisted of constructing, instrumenting and testing to failure forty-eight sandwich beam samples. The program was composed of undamaged geometries for baseline data and beams containing interlaminar flaws for residual strength characterization. The beams containing defects had compressive facesheets supplied by NASA-Langley Research Center. The implanted defects were of circular geometry and ranged in size from one half an inch to two inches in diameter. Two types of defect, Teflon film and Kapton bag, were used in this study. The undamaged beams had facesheets which were constructed at the Center for Composite Materials at the University of Delaware.

Four laminate stacking configurations were employed to generate information concerning the influence of laminate parameters on residual strength and buckling resistance. To examine the effect of laminate thickness on performance two laminates, $[0/\pm45]_{2s}$ and $[0/\pm45]_{s}$, were utilized. To evaluate the contribution of effective properties and stacking sequence, $[90/\pm45]_{s}$ and $[\pm45]_{2s}$ laminates were implemented.

The compressive laminates were all constructed of T300-5208 graphite/epoxy. The corresponding tensile facesheets were designed to limit bending deflections and insure failure in the compressive face. The tensile facesheets were also constructed of graphite/epoxy (T300-5209) in an effort to minimize thermal residual stresses in the sandwich fabrication process which arise due to expansion mismatch. The complete test program is outlined in Table 3.1.

3.1 Sandwich Beam Fabrication

The beams involved in the circular disbond defect study were all fabricated at the University of Delaware Center for Composite Materials during the period December 1979 to July 1980. The beams which contain implanted defects were composed of a compressive facesheet supplied by NASA-Langley, an aluminum honeycomb core obtained from Hexcel, Inc., and a tensile facesheet constructed at Delaware. The undamaged beams consisted of two facings constructed at Delaware, which duplicated the geometry of the facesheets used for the damaged beams and an identical honeycomb core.

The compressive facesheets contained embedded defects of a prescribed size and type. Three defect diameters, 1.27, 2.54 and 5.08 cm (0.5, 1.0 and 2.0 inches) were investigated and two defect types, Kapton bag or Teflon film, were utilized.

TABLE 3.1 EXPERIMENTAL TEST PROGRAM

	Teflon Film Defect			Kapton Bag Defect			No Defect
	2.0 in. Dia.	1.0 in. Dia.	0.5 in. Dia.	2.0 in. Dia.	1.0 in. Dia.	0.5 in. Dia.	
$[0/\pm45]_{2s}$ (12 ply)	F_{12}-1-1* F_{12}-1-2	F_{12}-2-1 F_{12}-2-2	F_{12}-3-1 F_{12}-3-2	F_{12}-6-1 F_{12}-6-2	F_{12}-5-1 F_{12}-5-2	F_{12}-4-1 F_{12}-4-2	F_{12}-0-1 F_{12}-0-2 F_{12}-0-3
$[\pm45]_{2s}$ (8 ply)	F_{8}-3-1 F_{8}-3-2	F_{8}-2-1 F_{8}-2-2	F_{8}-1-1 F_{8}-1-2	F_{8}-6-1 F_{8}-6-2	F_{8}-5-1 F_{8}-5-2	F_{8}-4-1 F_{8}-4-2	F_{8}-0-1 F_{8}-0-2 F_{8}-0-3
$[0/\pm45]_{s}$ (6 ply)	F_{6}-3-1 F_{6}-3-2	F_{6}-2-1 F_{6}-2-2	F_{6}-1-1 F_{6}-1-2	--	--	--	F_{6}-0-4 F_{6}-0-5 F_{6}-0-6
$[90/\pm45]_{s}$ (6 ply)	--	--	--	F_{6}-6-1 F_{6}-6-2	F_{6}-5-1 F_{6}-5-2	F_{6}-4-1 F_{6}-4-2	F_{6}-0-1 F_{6}-0-2 F_{6}-0-3

*Specimen Identification Number

The Teflon film defect consisted of a one mil Teflon sheet cut to the appropriate diameter and inserted in the laminate during fabrication. The Kapton bag defect was composed of two sheets of Kapton film, one half mil thick each, bonded together along the outer edge. The two sheets were cut oversize and a bead of room temperature cure adhesive was applied along the outer edge. Entrapped air was removed by flattening the two sheets together. After the adhesive had cured the edge was trimmed to the correct diameter and the defects were post-cured in a press at 177°C (350°F). The resulting defects contained a bonded region approximately 0.31 cm ($\frac{1}{8}$ inch) along the outer diameter. This defect geometry is illustrated in Figure 3.1.

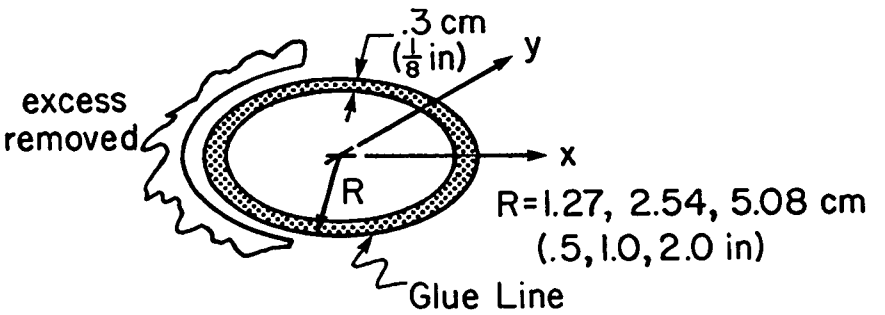

FIGURE 3.1 KAPTON BAG DEFECT GEOMETRY

All defects were inserted at the panel midplane during the fabrication process. Ultrasonic scanning was performed at NASA-Langley to establish exact defect location. The compressive facesheets were all constructed using the T300-5208 graphite/epoxy material system.

The tensile facesheets were constructed of T300-5209 graphite/epoxy. Laminate stacking sequence for the 12-ply and the $[0/\pm45]_s$ 6-ply laminate were identical to the compressive face. The $[90/\pm45]_s$ samples employed a $[0/\pm45]_s$ tensile facesheet because of the extremely low tensile strength of the 90° layers. The $[\pm45]_{2s}$ samples had a $[0°]_{16}$ tensile facesheet to prevent excessive deflections due to the high strain-to-failure of the $[\pm45]_s$ compressive laminate.

The four facesheet combinations are shown in Figure 3.2; effective elastic properties as determined from a laminate analysis code are presented in Appendix B. The constitutive matrices for the half plates used in formulating the reduced bending stiffness matrix are also presented.

The core was chosen to provide shear stiffness and preclude local crushing at the loading pads. A high density (22.1 lb/ft^3) aluminum honeycomb with 0.31 cm ($\frac{1}{8}$ inch) cell size was selected. Core density was constant throughout the beam.

Page Intentionally Left Blank

Core height was 3.80 cm (1.50 inches) and the length and width were cut to approximate size by means of a bandsaw. Since the ribbon direction in the honeycomb corresponded to the long axis of the sample, final specimen width was obtained by stripping away ribbons until the proper width was realized. This had the additional effect of producing a clean, uniform edge. Core preparation was completed by cleaning out individual cells with pressurized water, rinsing in acetone (as a degreasing agent) and allowing the precut honeycomb to air-dry for five days or more prior to use. Cell cleanout is critical to assure a reliable bond between face and core and this method proved effective as no failures could be attributed to laminate-core disbond.

The facesheets were bonded to the core by means of a commercial film adhesive. The adhesive, American Cyanamid FM300M, was cut to size and placed between the core and face. The entire assembly (see Figure 3.3) was placed in an alignment frame which insured that the facesheets did not shift. The alignment frame was vacuum bagged and autoclaved for the bonding process. The manufacturer's recommended cure cycle for the adhesive was followed:

Cure Cycle for FM300M Sheet Adhesive

1) Draw 30 in. Hg vacuum.
2) Apply 40 psi nitrogen.
3) Heat to 175°C. Dwell one (1) hour.
4) Release pressure
5) Cool to ambient.

Page Intentionally Left Blank

The strength of the bonding was investigated using three preliminary test beams and found to be more than adequate for all phases of the program.

3.2 Test Procedures

Following fabrication, the test specimens were instrumented with foil resistance strain gages. A preliminary test sample was instrumented at six locations across and along the center span to verify load uniformity (see Figures 3.4 and 3.5). The specimens containing flaws were instrumented with centrally located gages aligned in the load direction. The unflawed samples included transversely mounted gages to measure the Poisson strain. In all cases strain gages were mounted symmetrically on tensile and compressive facesheets.

A four-point flex fixture was developed to facilitate the wide beams. Placement of the loading pads was chosen to produce a 19.05 cm by 9.53 cm (7.5 inch by 3.75 inch) test section (2:1), with the remaining load pads located as shown in Figure 3.6. The distance between loading pads determines the moment at the center span and for our geometry was

$$M = \left(\frac{P}{2}\right)\left(\frac{24.0 - 7.75}{2}\right) = \left(\frac{65}{16}\right)P \quad \text{(lbs-in)} \qquad (3.1)$$

$$= (10.32)P \quad \text{(kg-cm)}$$

Page Intentionally Left Blank

Page Intentionally Left Blank

Page Intentionally Left Blank

Specimens were loaded in a floor model TTC Instron at a strain rate corresponding to a crosshead speed of 0.05 cm/min. Strain data was recorded by a Vishay Datran II data acquisition system and the maximum load was obtained from the Instron chart recorder. During the tests the compressive face was visually monitored to observe deformation of the defect region. All specimens were loaded through buckling (when applicable) to failure. Test data was transferred to the University computer (Burroughs 7700) where a plotting routine was employed to produce load-strain curves for each sample. From these curves defect buckling is clearly evident as indicated by the response of the compressive strain gage. The experimental equipment is shown in Figure 3.7. A close-up of the test fixture is shown in Figure 3.8.

3.3 Failure Classification

Failure modes are classified as compression, compression buckling, or concentrated load. Each classification indicates the predominant form of failure as combinations of failure modes can most often be discerned.

Compression failure was characterized by fiber breakage (0° plies) normal to the load accompanied by considerable axial splitting of 0° layers. Ultimate failure was abrupt and involved failure of the compressive laminate transverse

Page Intentionally Left Blank

Page Intentionally Left Blank

to the load. Extensive damage was confined to the test section and roughly centered above a kink in the honeycomb core which forms when the laminate crushes. No defect interaction is apparent for this failure. This failure mode is illustrated in Figure 3.9.

The compression buckling failure mode was characterized by extensive midplane delamination along the test section. Defect interaction was clearly evident. The portion of the laminate above the defect buckled and then crack propagation extended the delamination transverse to the load direction until the crack reached the sample free edges. The delamination then proceeded to grow longitudinally until it reached the extent of the test section. The portion of the laminate below the crack sustained the load until it reached its ultimate strength whereupon it failed in compression. This failure may be accompanied by local core crushing if the failure load is high. Compression buckling is illustrated in Figure 3.10.

The third predominant failure mode was due to concentrated loads. Here the laminate failed at or near one of the inside load pads. Failure often occurred outside the center span and is characterized by localized buckling and compressive failure of the laminate. Since this failure was induced by the loading pad and occurred outside the test section,

failure loads corresponding to this mode do not reflect the total capabilities of the facesheet under consideration. A characteristic concentrated load fialure is illustrated in Figure 3.11.

Failure modes are grossly affected by laminate properties and transitions from one failure mode to another over the range of defects is useful in assessing flaw criticality.

Page Intentionally Left Blank

Page Intentionally Left Blank

CHAPTER 4

TEST RESULTS

Typical load-strain curves for each laminate, covering the range of defect diameters, are presented in Appendix C. The appendix gives a brief explanation of several details of the curves and elaborates on the method of determining experimental buckling loads. The load axis represents the machine load, i.e. the load read from the Instron chart. It is necessary to convert this load to an equivalent in-plane stress resultant from which we can calculate compressive stress. An important note which must not be overlooked, however, is the fact that the buckling analysis considers half the machine load, since the buckling problem only accounts for half the thickness of the laminate.

A simple straightforward approach was used to convert machine load (P) to equivalent face stress. Consider the free body diagram shown in Figure 4.1. From equilibrium we have

$$\begin{aligned} \omega N_{x_{comp}} &= \omega N_{x_{tension}} = \omega N_x \\ \omega N_x h &= \frac{P}{2}(b - a) \end{aligned} \tag{4.1}$$

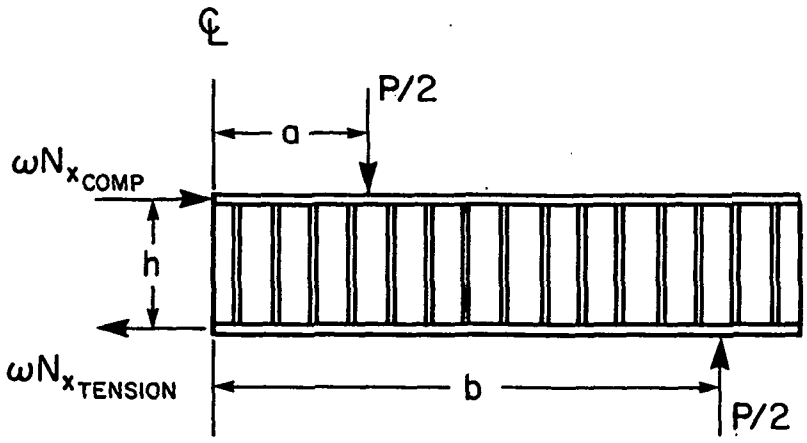

FIGURE 4.1 FREE BODY DIAGRAM OF HALF A SANDWICH BEAM

The moment arms are:

$$h = 3.81 + \frac{T_1+T_2}{2} \text{ cm} \quad \left(1.5 + \frac{T_1+T_2}{2} \text{ inches}\right)$$

$$a = 9.525 \text{ cm} \quad (3.75 \text{ inches})$$

$$b = 30.5 \text{ cm} \quad (12.0 \text{ inches})$$

where T_1 and T_2 are the facing thicknesses, and ω is the width of the beam.

For uniform compression

$$\sigma_{x_c} = \frac{N_x}{T_1} = \frac{P(b-a)}{2h\omega T_1} \tag{4.2}$$

Use of this equation, with appropriate dimensions, allows the calculation of facing stress for a general sandwich beam in four-point bending.

Failure information is presented in Tables 4.1 through 4.4. Buckling loads were determined from load-strain plots as discussed in Appendix C and ultimate load was defined as maximum load attained (as opposed to individual ply failure). The compressive stress at failure was calculated using Equation 4.2 and the predominant failure mode was labeled per section 3.3.

The tabulated failure information is plotted separately in the form of residual strength curves (Figures 4.2 through 4.5). The figures indicated the regions where particular failure modes occurred, as these transitions aid in interpreting results.

Since each figure contains a wealth of information, each one will be explained individually, accounting for unexpected results as they arise.

TABLE 4.1 UNDAMAGED SAMPLE FAILURE INFORMATION

	Sample Identification Number	Ultimate Load kN	(lbs)	Ultimate Compressive Stress MPa	(ksi)	Predominant Failure Mode
12 Ply $[0/\pm45]_{2s}$	F_{12}-0-1	33.34	(7496)	617.36	(89.525)	Comp.*-Comp. Buckling
	F_{12}-0-2	33.58	(7551)	611.34	(88.652)	Compression Buckling
	F_{12}-0-3	30.49	(6856)	574.62	(83.327)	Compression Buckling
8 Ply $[\pm45]_{2s}$	F_8-0-1	10.39	(2337)	276.62	(40.113)	Comp.-Concentrated Load
	F_8-0-2	9.91	(2227)	270.51	(39.227)	"
	F_8-0-3	10.14	(2282)	277.20	(40.198)	"
6 Ply $[0/\pm45]_s$	F_6-0-4	15.59	(3505)	578.72	(83.922)	Compression
	F_6-0-5	15.59	(3505)	578.86	(83.943)	"
	F_6-0-6	14.29	(3214)	531.41	(77.061)	"
6 Ply $[90/\pm45]_s$	F_6-0-1	5.98	(1345)	214.86	(31.158)	Compression Buckling
	F_6-0-2	6.23	(1400)	231.19	(33.526)	"
	F_6-0-3	5.88	(1323)	211.28	(30.638)	"

*Comp. = Compression

TABLE 4.2 12-PLY FAILURE INFORMATION

	Sample Identification Number	Defect Buckling Load (kN)	Ultimate Load (kN)	Ultimate Compressive Stress MPa	(ksi)	Predominant Failure Mode
12-Ply $[0/\pm45]_{2s}$ Samples	F_{12}-1-1	10.32	19.07	328.74	(47.671)	Compression Buckling
	F_{12}-1-2	--*	23.59	406.42	(58.936)	Compression
	F_{12}-2-1	--	26.54	442.87	(64.222)	Compression
	F_{12}-2-2	--	24.18	403.50	(58.513)	Comp.-Comp. Buckling
	F_{12}-3-1	--	30.47	485.43	(70.394)	Compression
	F_{12}-3-2	--	30.47	518.80	(75.128)	Compression
	F_{12}-4-1	--	34.16	569.99	(82.656)	Compression
	F_{12}-4-2	--	33.17	555.19	(80.509)	Compression
	F_{12}-5-1	--	32.93	542.72	(78.701)	Compression
	F_{12}-5-2	--	34.90	574.94	(83.373)	Compression
	F_{12}-6-1	--	28.90	475.99	(69.025)	Compression
	F_{12}-6-2	--	21.33	351.55	(50.979)	Compression Buckling

*No apparent defect buckling prior to failure.

TABLE 4.3 8-PLY FAILURE INFORMATION

	Sample Identification Number	∿Defect Buckling Load (kN)	Ultimate Load (kN)	Ultimate Compressive Stress MPa	(ksi)	Predominant Failure Mode
8-Ply $[\pm 45]_{2s}$ Samples	F_8-1-1	--*	11.95	295.04	(42.784)	Concentrated Load
	F_8-1-2	--	11.32	279.53	(40.536)	Concentrated Load
	F_8-2-1	--	11.99	296.33	(42.971)	Concentrated Load
	F_8-2-2	--	11.99	296.33	(42.971)	Concentrated Load
	F_8-3-1	--	11.20	276.76	(40.134)	Compression Buckling
	F_8-3-2	--	11.15	275.66	(39.974)	Compression Buckling
	F_8-4-1	--	11.50	284.21	(41.214)	Concentrated Load
	F_8-4-2	--	11.50	284.27	(41.227)	Compression
	F_8-5-1	--	11.90	287.31	(41.554)	Compression Buckling
	F_8-5-2	11.41	11.59	279.78	(40.571)	Compression Buckling
	F_8-6-1	--	12.31	304.23	(44.117)	Compression Buckling
	F_8-6-2	--	11.50	284.11	(41.200)	Compression Buckling

*No apparent defect buckling prior to failure.

TABLE 4.4 6-PLY FAILURE INFORMATION

	Sample Identification Number	∿Defect Buckling Load (kN)	Ultimate Load (kN)	Ultimate Compressive Stress MPa	(ksi)	Predominant Failure Mode
6-Ply $[0/\pm45]_s$ Samples	F_6-1-1	4.91	11.50	398.98	(57.857)	Comp.-Comp. Buckling
	F_6-1-2	6.88	11.70	419.03	(60.765)	Comp.-Comp. Buckling
	F_6-2-1	2.80	9.73	337.38	(48.925)	Comp.-Comp. Buckling
	F_6-2-2	1.72	9.93	355.77	(51.591)	Compression Buckling
	F_6-3-1	1.96	7.91	283.37	(41.092)	Compression Buckling
	F_6-3-2	2.36	8.70	311.53	(45.176)	Compression Buckling
6-Ply $[90/\pm45]_s$ Samples	F_6-4-1	5.52	7.40	265.23	(38.461)	Compression Buckling
	F_6-4-2	3.97	6.59	228.92	(33.197)	Compression Buckling
	F_6-5-1	3.12	7.71	267.60	(38.805)	Compression Buckling
	F_6-5-2	N/I*	6.87	296.91	(35.669)	Compression Buckling
	F_6-6-1	--**	6.91	247.49	(35.889)	Compression Buckling
	F_6-6-2	N/I	7.44	258.32	(37.459)	Compression Buckling

*N/I = No information
**No apparent defect buckling prior to failure.

4.1 Influence of Laminate Thickness on Residual Strength

Figure 4.2 presents the results of the 12-ply $[0/\pm45]_{2s}$ and 6-ply $[0/\pm45]_{s}$ Teflon film defect samples. These two laminates had identical effective elastic properties wiht one being twice the thickness of the other. The effective properties, however, did not reflect certain differences which can be seen from the constitutive matrices of Appendix B. Of particular importance is the effective bending stiffnesses of the laminate above the disbond. This can be expressed as

$$D_{effective} = \left(\frac{D_{11}^{*} + D_{22}^{*}}{2}\right) + \left(\frac{D_{12}^{*} + 2D_{66}^{*}}{3}\right) \qquad (4.3)$$

where D_{ij}^{*} are the reduced stiffnesses. When the effective bending stiffness of the two laminates ([0/±45/0/±45] and [0/±45]) are calculated, the thicker laminate was shown to be almost fifteen times stiffer in bending than the thin laminate. This represents a considerable difference from what might be casually estimated; i.e., twice as thick, eight times as stiff. The difference arises from the unsymmetric laminate stacking sequence and the fact that $[0_2/+45_2/-45_2]$ does not have the same bending properties as [0/±45/0 ±45].

Page Intentionally Left Blank

Returning attention to Figure 4.2, the significant details may now be pointed out. The results for both sets of undamaged beams are plotted on the vertical axis and no clear difference in undefected strength was discerned. Hence σ_0 was defined as the average of these six values. The reduced strengths of the damaged beams were plotted and curves were drawn through the average of each data pair. The 12-ply beams exhibited a strength reduction of approximately 35 to 40 percent over the range of defect diameters investigated. The corresponding 6-ply beams showed a strength loss approaching 50 percent at the two-inch diameter defect.

The dashed line on Figure 4.2 divides the graph into regions where particular failure modes occurred. Twelve-ply samples failed by compression almost exclusively with the exception of one two-inch defect sample. Failure in the 6-ply samples was by compression buckling. The undamaged beams failed in mixed modes.

In the compression buckling failure mode the external plies delaminated extensively and exhibited drastically reduced extensional stiffness. As this delamination increased in size its contribution to laminate strength approached zero and hence it is postulated that the residual strength should asymptotically approach $\sigma_0/2$. Although it appeared that the thicker samples had residual strengths approaching

60 percent, it is plausible that a failure mode transition would occur and the 50 percent limit would be realized at some larger defect size.

In summary, then, it appears that there exists a well defined thickness effect on residual strength of laminates containing embedded flaws. This effect is attributed to failure mode transition which arises from the buckling resistance difference between the 6- and 12-ply samples.

4.2 Influence of Defect Type on Residual Strength

The 12-ply and 8-ply samples encompassed both of the defect types. The 6-ply $[0/\pm45]_s$ contained Teflon film defects and the 6-ply $[90/\pm45]_s$ had Kapton bag implants. The residual strength curves for the 12- and 8-ply panels are presented in Figures 4.3 and 4.4.

The 12-ply samples show that Kapton bag defects up to one inch in diameter had a negligible effect on residual strength, whereas a similar Teflon film defect caused a 25 percent strength loss. The trend diminishes at larger defect diameters where the difference between residual strengths was approximately 10 percent and decreased rapidly with defect size. These results indicate the possibility of two distinct failure mechanisms arising from the individual

Page Intentionally Left Blank

Page Intentionally Left Blank

defect characteristics. The nominal thickness of the two defects was the same but the complex construction of the Kapton bag defect may have interacted with the surrounding structure in such a way to produce a smaller stress concentrating effect. If it is asserted that failure initiates around the disbond edge, then the controlling mechanism may well have been the effective radius of the crack which is represented by the implanted defect. Determination of the controlling mechanism represents a sophisticated fracture mechanics problem involving detailed characterization of the implanted defect geometry and as such will not be treated here.

In order to reinforce the results from the 12-ply study, the 8-ply results are examined next. Since the defect in both sets of samples is located between similar layers (.../-45/defect/-45/...), similar behavior would be expected. This was however not the case.

The results for the 8-ply samples indicate that no defect influence on residual strength occurred. Over the range of defect diameters and types no loss of static strength was encountered. The failure underwent a transition from concentrated load and compression modes to compression buckling.

A closer examination of the 8-ply failure surfaces provides additional information. It appears that some form

of laminate buckling occurred in each failure mode. The beams which failed by the loading pads exhibit buckling of the laminate between plies 7 and 8 (eight is bonded to core). This buckling occurred outside the test section so clearly the defect was not of importance. For the Teflon film defect the only failures in the test section occurred for the 2.0 inch defect. These failures occurred between plies 4 and 5 and the defect was clearly visible from the side. The buckled region did not, however, propagate along the length of the test section; when the crack reached the free edges, failure initiated.

The half inch Kapton bag defects did not influence laminate strength as failures occurred away from the disbond region. Both half inch samples did exhibited some form of buckling in their failures with the concentrated load failure again occurring between plies 7 and 8. The one inch defects failed when the crack reached the free edges but the two inch diameter Kapton bag defect failures were of the classic compression buckling mode with the delamination extending along the entire test section. Close examination of the internal structure of the failure showed remnants of the Kapton bag defect still adhered to individual fiber strands. This is in clear contrast to the Teflon film defects which remained intact and in fact could be removed

with tweezers. This difference reinforces the need for a complete characterization of the in situ defect properties including photomicrographs of defect geometries.

From the results presented in Figures 4.3 and 4.4, one can see the range of possible effects of defect type on residual strength. A complex interaction of failure modes overshadows any difference between types for the $[\pm 45]_{2s}$ samples, but the samples did not exhibit reduced strength with defect size. The 12-ply results indicate the need for a comprehensive investigation into the defect characteristics. It is important to carefully analyze the effect of defect type because in modeling a physical problem the closer approximation to the physics of the crack, the more useful the experimental results will be.

4.3 Influence of Stacking Sequence on Residual Strength

Residual strength data for the $[90/\pm 45]_s$ laminate is presented in Figure 4.5. The apparent incrase in strength with the inclusion of even a large defect is attributed to faulty representation of the undamaged strength. As was described earlier, the panels representing the no-defect geometries were fabricated separately using a different material batch. The presence of 90° layers in the laminate tended to highlight matrix material property differences, including those

Page Intentionally Left Blank

which arise due to thermal history. Since identical thermal history could not be duplicated the resulting strength discrepancy has occurred. If we concentrate only on the damaged beams, we can comment on flaw criticality and stacking sequence influence.

As was just seen in the previous sections the Kapton bag defect is considerably less critical than a corresponding Teflon film defect. This remained the case in the $[90/\pm45]_s$ samples, over the range of defect diameters. There was no trend toward reduction in static strength. The failure mode was compressive buckling with the failures occurring predominantly along the midply and secondary delaminations occurring along the facesheet-adhesive interface. Investigation of the delamination surface (midply) showed no physical remains of the defect -- only regions on the third and fourth plies with a smooth, shiny surface indicating the location of the defect.

If the combined results of Figures 4.2 through 4.5 are considered, some inferences can be drawn about stacking sequence influence on residual strength. For the Kapton bag defect little influence of stacking sequence on flaw criticality was observed for all laminates with the exception of the two inch defect in the 12-ply laminate. Since stacking

sequence influences strength and failure mode, documenting these aspects allows us to infer a general influence.

Compression failures generally involved high strength configurations while compression buckling was associated with low loads - low strengths. From this it is inferred that high strength configurations are considerably more flaw sensitive than low strength laminates. This same result was arrived at when considering the sets of beams containing Teflon film defects. Here the flaw sensitivity was greater as is shown in Figure 4.3 for the 12-ply high strength laminate, but the 8-ply results indicated no sensitivity as was observed for the other defect.

An important tool useful in predicting failure modes and flaw criticality is the buckling analysis developed in Chapter 2. The correlation of buckling with flaw criticality is discussed next.

4.4 Comparison of Buckling Results

In order to compare experimental and analytical beuckling loads, the relationship of machine load and stress resultant acting on the debond must be indicated. Experimental buckling loads are determined by monitoring strain reversal of the compressive gage. This method gives the machine

load at which buckling occurs. Using Equation 4.2, with the appropriate dimensions, this can be converted into a buckling stress. For the analytic buckling condition, represented by Equation 2.24, only one half the laminate is considered so an effective buckling stress of twice that which Equation 2.24 indicates is actually applied. The analytic buckling condition becomes:

$$\sigma_{crit} = \frac{N_x}{T_1} = \frac{2N_{x\text{-}crit}}{T_2} = \frac{-48}{T_1 R^2}\left(\frac{D_{11}^{*}+D_{22}^{*}}{2} + \frac{D_{12}^{*}+2D_{66}^{*}}{3}\right) \quad (4.4)$$

where D_{ij}^{*} are the reduced bending stiffness terms, T_1 is the compressive face thickness, R is the defect radius, $N_{x\text{-}crit}$ is the critical buckling load, and N_x is the applied in-plane load. Equation 4.4 is plotted in Figure 4.6 for each compressive laminate configuration.

Figure 4.6 shows that the laminates examined in the experimental program covered a wide range of effective buckling resistances, ranging from the low stiffness of the 6-ply through the highly resistant 12-ply laminate. The figure shows no difference in buckling resistance between the [0/±45] and the [90/±45] laminate. This is simply a reflection of the assumed symmetries in the approximating mode shape.

Unfortunately, the experimental program produced a limited amount of detectable defect buckling. The 12-ply

Page Intentionally Left Blank

samples contained only one instance of buckling prior to failure. The 8-ply $[\pm 45]_s$ samples, although failing by compressive buckling in several instances, also produced only one case of prefailure buckling which could be detected from load-strain results. These two results, a two inch defect 12-ply and a one inch 8-ply sample, are plotted in Figure 4.6 and show excellent agreement with their respective analytic prediction. The difference between experimental and analytical results for these two cases is less than five percent.

The 6-ply laminates had numerous instances of prefailure buckling. These results are plotted in Figure 4.6 and also appear separately in Figure 4.7. The results show that, as predicted, there was no clear delineation between buckling loads for the [0/±45] and the [90/±45] half laminates. This would indicate that the assumption of axisymmetric deflection shapes for the buckled mode is in fact valid. The agreement between experimental and analytic results is very good for the one inch diameter data, but considerable discrepancy exists at the one half and two inch diameter defects. The average buckling stress of the one half inch defect is over fifty percent less than the analytically predicted value while the average buckling stress for the two inch defect is three times greater than the analytic

Page Intentionally Left Blank

result. The discrepancy between results should not be prematurely attributed to the simplified analytical approach as it has been seen that the results for other laminates agree quite well. Rather, the difficulty may lie in the experimental condition of the 6-ply laminates. Seemingly small aberrations in the defect geometry can effect the results substantially.

The 6-ply samples exhibited considerable out-of-plane "prebuckling" as a result of the facesheet bonding process. Although the extent of the prebuckling was not measured it was visually evident, especially for the [90/±45] configuration. The effect of this initial irregularity on critical buckling load would be a reduction in magnitude and may explain the discrepancy between results for the half inch defect. To explain the poor agreement at the larger disbond, however, a different influence must be postulated. Perhaps a small amount of work is necessary to break the interface between the laminate and defect. Possibly the assumption concerning the amount of load which the defect carries contains a small error which is magnified due to the small thickness of the half laminate (0.38 mm (0.015 in.)). These and other influences are easily generated but remain speculative unless a more extensive examination of the defect is performed.

The buckling analysis provides a good estimate of which failure mode dominates and where failure mode transitions may occur. When the buckling load is considerably higher than the undamaged strength (σ_o), failure mode was seen to be predominantly compression or concentrated load. As the buckling load approached the undamaged strength a transition to buckling failure mode occurred. Samples with a buckling load much lower than σ_o generally failed by compression buckling. Figure 4.8 graphically represents this failure mode transition as it relates to undamaged strength.

The $[\pm 45]_{2s}$ laminate showed a clear transition occurring about the one inch defect as was predicted by examining the analytic buckling result. The remaining sets of data shared similar correlation with the exception of the $[90/\pm 45]_s$ samples where the influence of other factors resulted in buckling for even the smallest defect. A comparison of the location of failure transition for all the laminates appears in Table 4.5. The experimental estimates of the location of failure mode transition are based on an examination of only three defect diameters and hence can only be expressed in terms of those diameters.

Page Intentionally Left Blank

TABLE 4.5 LOCATION OF FAILURE MODE TRANSITION

Laminate	Transition Diameter (in.)	
	Experimental	Analytical
$[0/\pm45]_{2s}$	1.0 - 2.0	1.3
$[\pm45]_{s}$	1.0	1.2
$[0/\pm45]_{s}$	< 0.5	0.35
$[90/\pm45]_{s}$	None	0.7

CHAPTER 5

CONCLUSIONS

Laminate residual strength, the prominent quantity used to assess flaw influence, has been shown to be affected substantially by defect size and type and laminate thickness and stacking sequence.

Examination of two similar laminates, $[0/\pm45]_{2s}$ and $[0/\pm45]_{s}$, showed that when delamination buckling was prevented residual strength was increased. The thicker laminate was up to fifteen percent stronger over the range of defect diameters examined.

The $[\pm45]_{s}$ laminate exhibited a failure mode transition at the one inch diameter defect. In line with the $[0/\pm45]_{s}$ and $[0/\pm45]_{2s}$ results, an accompanying strength reduction was anticipated but did not occur. The [±45] samples, although exhibiting all predominant failure modes, showed no reduced strength over the range of defect sizes and types. The $[90/\pm45]_{s}$ samples, which showed no failure mode transition, also were not influenced by any of the examined defects. This information indicates that particular laminate configurations fail by a characteristic

mechanism and the mechanism may be independent of the presence of delamination flaws. One such mechanism may be midplane cracking with subsequent load transfer from the delaminated plies to the interior, core supported laminate. The extent and location of this internal cracking could produce the appearance of any of the described failure modes.

The two defects examined, Kapton bag and Teflon film, produced no discernable difference in the response of the $[\pm 45]_s$ laminate. The results for the $[0/\pm 45]_s$ laminate, however, showed considerable dependence on defect type. The Kapton bag was substantially less critical than a corresponding Teflon defect (20 percent greater strength at the one inch diameter defect). This result highlights the necessity of selecting an appropriate defect construction when modeling a delamination.

It is postulated that the superior bonding of the Kapton to the epoxy matrix promotes less severe conditions at the defect edge by increasing the "toughness" of the edge geometry against crack initiation.

The presence of defect buckling plays an important role in the failure process because the buckled geometry produces additional stress concentration along the edge of

the defect. The Rayleigh-Ritz approximation for the buckling loads of the various laminates showed excellent agreement for several cases. The 6-ply test results indicated that no substantial difference existed between buckling loads of the $[0/\pm45]_s$ and $[90/\pm45]_s$ samples. This supports the assumption of an axisymmetric deflection shape as used in the analysis. The discrepancies between analytic and experimental results for the 6-ply tests may be a result of initial "prebuckling" imperfections or may be attributed to the inaccuracy of using the reduced bending stiffness approximation to account for the bending-twisting coupling of the thin unsymmetric half laminate.

The buckling analysis also proved helpful in predicting failure mode transition. The capability to predict this transition is extremely useful when attempting to establish the important parameters governing the failure of a particular geometry.

It is evident from the results that several quantities must be examined when considering the flaw criticality problem. One obvious fact is that only the high-strength ($[0/\pm45]_{1s-2s}$) laminate showed considerable loss of strength with the inclusion of defects. Since the high-strength laminates are primarily used in applications where in-plane loads may cause

buckling (as opposed to [±45] shear applications), further experimental work should concentrate on these configurations.

Suggestions for Future Work

Throughout this work it has become apparent that several areas encompass possibilities for further study. An in-depth characterization of the in situ defect properties is especially needed. Researchers have been modeling interlaminar disbonds with several defect configurations including Teflon film, Teflon bag and Kapton bag. As our results indicate substantial differences in response can be encountered. A study of various defect configurations should include photomicrographs of sectioned samples, as well as experiments to evaluate the sensitivity of the material to various flaw materials and defect geometries. A comparison to an ideal crack with no thickness could be made through the use of a numerical technique such as the finite element method. Such a comparison would yield estimates of the discrepancy between an unfilled crack and an implanted flaw.

Two other areas of experimental interest would be an extension to defects located other than on the midply, and a nondestructive evaluation of crack growth with loading, including fatigue. The two areas actually are interrelated.

In a typical structure with many plies the defect can occur anywhere throughout the thickness. If the crack occurs near the surface of the laminate only minor strength loss may occur corresponding to failure of the outer plies. If however the damage occurs near midply the effect may not be visible until further crack growth has occurred; then the possibility of gross buckling and catastrophic failure is increased. With any genuine component the defect location is not known a priori and hence some technique such as ultrasonic scanning must be used to determine where the defect occurs and how it is propagating. As has been shown a circular defect does not propagate as a series of concentric circular rings. With the aid of ultrasonic techniques, a sample in a fatigue environment can be monitored and necessary defect growth information can be obtained.

As was shown the present buckling approximation shows excellent agreement for the thicker laminates examined, but some discrepancy was encountered in the 6-ply cases; a program which is designed primarily to produce defect buckling would be invaluable in verifying the buckling approximation. If the additional work produces discord then an examination of the buckling analysis is in order including a check on the approximation involved in the use of the reduced bending stiffness approximation.

Perhaps the most fruitful area for further research is the analysis of the fracture problem which arises after defect buckling. The geometry represents a complicated, two-dimensional extension to Chai's [17] thin film strip analysis. Modeling the crack with finite element techniques is appealing but a large number of degrees of freedom are required and mesh generation is conceptually difficult. The post-buckling fracture may contain the answer to many unanswered questions on flaw criticality and a solution in this area would be a considerable contribution.

REFERENCES

[1] Husman, G. E., Whitney, J. M. and Halpin, J. C., "Residual Strength Characterization of Laminated Composites Subject to Impact Loading," Foreign Object Damage to Composites, ASTM STP568, American Society for Testing and Materials, 1975, pp. 92-113.

[2] Williams, Jerry G., et al., "Recent Developments in the Design, Testing and Impact Resistance of Stiffened Composite Panels," NASA TM80077, April 1979.

[3] Shuart, M. J. and Herakovich, C. T., "An Evaluation of the Sandwich Beam in Four-Point Bending as a Compressive Test Method for Composites," NASA TM78783, September 1978.

[4] Plantema, Frederik J., Sandwich Construction: The Bending and Buckling of Sandwich Beams, Plates and Shells, John Wiley & Sons, New York, 1966.

[5] Allen, Howard G., Analysis and Design of Structural Sandwich Panels, Pergamon Press, New York, 1969.

[6] Timoshenko, S., Theory of Elastic Stability, McGraw-Hill, Inc., New York, 1936, p. 367.

[7] Dym, C. L., Stability Theory and its Application to Structural Mechanics, Nordhoff Int. Publishing, Leyden, The Netherlands, 1974, p. 120.

[8] Chia, Chuen-Yuan, Non-Linear Analysis of Plates, McGraw-Hill, New York, 1980, p. 174.

[9] Durban, David, "Instability of an Elastic Circular Plate Subjected to Nonuniform Loads," AIAA Journal, Vol. 15, No. 3, p. 360.

[10] Yamaki, N., "Buckling of a Circular Plate under Locally Distributed Forces," Institute of High Speed Mechanics, Tokyo University, Japan, Vol. 8, 1957, pp. 13-24.

[11] Vinson, J. R., Structural Mechanics: The Behavior of Plates and Shells, Wiley & Sons, New York, 1974, p. 92.

[12] Ashton, J. E. and Whitney, J. M., Theory of Laminated Plates, Technomic, Inc., Stanford, Connecticut, 1970, pp. 31-34.

[13] Ibid., p. 137.

[14] Ibid., Chapter 1.

[15] Timoshenko, op. cit., p. 367.

[16] Ibid., p. 364.

[17] Chai, Herzl, et al., "On the Failure of Laminated Plates by Delamination Buckling," Graduate Aeronautical Laboratory, Cal. Inst. of Tech., Pasadena, California, July 1980.

[18] Ibid.

[19] Kachanov, L. M., "Separation of Composite Materials," Mekhanika Polimerov (Polymer Mechanics), No. 5, 1976, pp. 918-922 (812-815).

APPENDIX A

Derivation of Critical Buckling Loads

Here the use of the Rayleigh-Ritz method is presented in a detailed manner. The energy equation is first stated then derivatives of the assumed deflection are presented. Finally, these derivatives are incorporated in the two cases, isotropic and orthotropic material symmetry. By appropriate substitutions, the orthotropic case is seen to reduce to the isotropic result.

The general form of the potential energy function is

$$\tfrac{1}{2}\int_S \Big[D_{11}^* w_{xx}^2 + 2D_{12}^* w_{xx}w_{yy} + D_{22}^* w_{yy}^2 + 4D_{16}^* w_{xx}w_{xy} + 4D_{26}^* w_{yy}w_{xy} + 4D_{66}^* w_{xy}^2 + N_x w_x^2\Big]dS = \text{Constant} \tag{A.1}$$

and for an isotropic material

$$D_{11}^* = D_{22}^* = D \qquad D_{12}^* = \nu D$$
$$D_{66}^* = \frac{(1-\nu)}{2} D \qquad D_{16}^* = D_{26}^* = 0 \tag{A.2}$$

where $D = \dfrac{Eh^3}{12(1-\nu^2)}$

This reduces the energy equation to

$$\frac{D}{2}\int_S [(w_{xx}+w_{yy})^2 - 2(1-\nu)(w_{xx}w_{yy}-w_{xy}^2)\,dS + \tfrac{1}{2}\int_S N_x w_x^2\,dS = \text{Constant} \tag{A.3}$$

Assume a buckled deflection of the form

$$w(x,y) = A\left(1-\frac{x^2+y^2}{R^2}\right)^2 = A\left(1-\frac{2(x^2+y^2)}{R^2}+\frac{(x^2+y^2)^2}{R^4}\right) \tag{A.4}$$

where A = undetermined amplitude

R = defect radius

The boundary conditions are

$$w(R) = 0 \qquad \frac{\partial w}{\partial r}(R) = 0 \tag{A.5}$$

for the problem of interest.

The required partial derivatives are

$$w_x = A\left(\frac{-4x}{R^2}+\frac{4x^3}{R^4}+\frac{4xy^2}{R^4}\right) \tag{A.6}$$

$$w_{xx} = A\left(\frac{-4}{R^2}+\frac{12x^2}{R^4}+\frac{4y^2}{R^4}\right) \tag{A.7}$$

$$w_{xy} = A\left(\frac{8xy}{R^4}\right) \tag{A.8}$$

$$w_{yy} = A\left(\frac{-4}{R^2} + \frac{12y^2}{R^4} + \frac{4x^2}{R^4}\right) \tag{A.9}$$

The products of these terms as required for Eq. A.3 are

$$w_x^2 = \frac{16A^2}{R^4}\left(x^2 + \frac{x^6}{R^4} + \frac{x^2y^4}{R^4} - \frac{2x^4}{R^2} - \frac{2x^2y^2}{R^2} + \frac{2x^4y^2}{R^4}\right) \tag{A.10}$$

$$w_{xx}^2 = \frac{16A^2}{R^4}\left(1 + \frac{9x^4}{R^4} + \frac{y^4}{R^4} - \frac{6x^2}{R^2} - \frac{2y^2}{R^2} + \frac{6x^2y}{R^4}\right) \tag{A.11}$$

$$w_{xy}^2 = \frac{16A^2}{R^4}\left(\frac{4x^2y^2}{R^4}\right) \tag{A.12}$$

$$w_{yy}^2 = \frac{16A^2}{R^4}\left(1 + \frac{9y^4}{R^4} + \frac{x^4}{R^4} - \frac{6y^2}{R^2} - \frac{2x^2}{R^2} + \frac{6y^2x^2}{R^4}\right) \tag{A.13}$$

$$w_{xx}w_{yy} = \frac{16A^2}{R^4}\left(1 + \frac{3(y^4+x^4)}{R^4} + \frac{10x^2y^2}{R^4} - \frac{4(x^2+y^2)}{R^2}\right) \tag{A.14}$$

Substituting Equations A.10 through A.14 into the energy equation and combining terms yields:

$$\frac{8A^2D}{R^4}\int_S\left[2(1+\nu) - 8(1+\nu)\left(\frac{x^2+y^2}{R^2}\right) + (10+6\nu)\left[\frac{(x^2+y^2)^2}{R^4}\right]\right]dS$$

$$+ \frac{8A^2N_x}{R^4}\int_S\left[x^2 - 2x^2\,\frac{(x^2+y^2)}{R^2} + x^2\,\frac{(x^2+y^2)^2}{R^4}\right]dS$$

$$= \text{Stationary Value} \tag{A.15}$$

For the assumed deflection taking the variation with respect to the deflection amplitude, A, and incorporating the substitutions $r^2 = x^2 + y^2$, $x = r\cos\theta$ yields:

$$D\int_S \left[2(1+\nu) \; -8(1+\nu)\frac{r^2}{R^2} + (10+6\;)\frac{r^4}{R^4}\right] dS$$

$$+ N_x \int_S \left[r^2 - \frac{2r^4}{R^2} + \frac{r^6}{R^4}\right] \cos^2\theta \, dS \;\; = \;\; 0 \qquad \text{(A.16)}$$

Integrating this expression is most conveniently performed in polar coordinates (recall that $ds = rdrd\theta$). This yields the isotropic result

$$\frac{4}{3} D + \frac{N_x R^2}{24} \;\; = \;\; 0 \quad \text{or} \quad N_{x_{crit}} \;\; = \;\; \frac{-32D}{R^2} \qquad \text{(A.17)}$$

For the orthotropic case the previously calculated derivatives and products can be utilized along with

$$w_{xx} w_{xy} = \frac{16A^2}{R^4}\left[\frac{-2xy}{R^2} + \frac{6x^3 y}{R^4} + \frac{2xy^3}{R^4}\right] \qquad \text{(A.18)}$$

$$w_{yy} w_{xy} = \frac{16A^2}{R^4}\left[\frac{-2xy}{R^2} + \frac{6y^3 x}{R^4} + \frac{2yx^3}{R^4}\right] \qquad \text{(A.19)}$$

Inserting these into the general form of the potential energy (Equation A.1) and evaluating each term separately yields:

$$\int_0^R \int_0^{2\pi} \left[D_{11}^* \left(1 + \frac{r^2}{R^2} (-6\cos^2\theta - 2\sin^2\theta) + \frac{r^4}{R^4} (9\cos^4\theta + \sin^4\theta - 6\sin^2\theta\cos^2\theta) \right) \right] r\,dr\,d\theta = \frac{D_{11}^* \pi R^2}{2}$$

$$\int_0^R \int_0^{2\pi} \left[2D_{12}^* \left(1 - \frac{4r^2}{R^2} + \frac{3r^4}{R^4} + \frac{4r^4\cos^2\theta\sin^2\theta}{R^4} \right) \right] r\,dr\,d\theta = \frac{D_{12}^* \pi R^2}{3}$$

$$\int_0^R \int_0^{2\pi} \left[D_{22}^* \left(1 + \frac{r^2}{R^2} (-6\sin^2\theta - 2\cos^2\theta) + \frac{r^4}{R^4} (9\sin^4\theta + \cos^4\theta + 6\sin^2\theta\cos^2\theta) \right) \right] r\,dr\,d\theta = \frac{D_{22}^* \pi R^2}{2}$$

$$\int_0^R \int_0^{2\pi} \left[8D_{16}^* \left(\frac{r^2}{R^2} (-\sin\theta\cos\theta) + \frac{r^4}{R^4} (3\sin\theta\cos^3\theta + \cos\theta\sin^3\theta) \right) \right] r\,dr\,d\theta = 0$$

$$\int_0^R \int_0^{2\pi} \left[8D_{26}^* \left\{ \frac{r^2}{R^2} (-\sin\theta\cos\theta) + \frac{r^4}{R^4} (3\sin^3\theta\cos\theta + \cos^3\theta\sin\theta) \right\} \right] r\,dr\,d\theta = 0$$

$$\int_0^R \int_0^{2\pi} \left[16D_{66}^* \left\{ \frac{r^4}{R^4} (\cos^2\theta\sin^2\theta) \right\} \right] r\,dr\,d\theta = \frac{2\pi}{3} D_{66}^* R^2$$

$$\int_0^R \int_0^{2\pi} \left[N_x \left(r^2 + \frac{r^4}{R^4} + \frac{r^6}{R^4} \right) \cos^2\theta \right] r\,dr\,d\theta = \frac{\pi N_x R^2}{24}$$

Summing these results gives

$$\frac{D_{11}^*}{2} + \frac{D_{12}^*}{3} + \frac{D_{22}^*}{2} + \frac{2D_{66}^*}{3} = \frac{-N_x R^2}{24}$$

or

$$N_{x_{crit}} = \frac{-24}{R^2} \left(\frac{D_{11}^* + D_{22}^*}{2} + \frac{D_{12}^* + 2D_{66}^*}{3} \right) \qquad \text{(A.20)}$$

To check this result with the isotropic case, Equations A.2 are substituted in Equation A.20 to yield

$$N_{x_{crit}} = \frac{-24}{R^2}\left[\frac{D+D}{2} + \frac{\nu D + 2\left(\frac{1-\nu}{2}\right)D}{3}\right] = \frac{-24}{R^2}\left(\frac{4}{3}D\right) = \frac{-32D}{R^2}$$

APPENDIX B

Effective Elastic Properties

Here we present the results of our laminate analysis, and the A, B, D matrices for the half plates used in the buckling analyses.

The material properties input to the computer routine are:

E_1 = 144.8 GPa (21.0×10^6 psi)

E_2 = 10.9 GPa (1.58×10^6 psi)

ν_{12} = 0.28

G_{12} = 6.2 GPa (0.9×10^6 psi)

The four laminates of interest are:

$[0/\pm 45]_s$

$[0/\pm 45]_{2s}$

$[\pm 45]_{2s}$

$[90/\pm 45]_s$

The effective elastic properties appear in Table B.1.

TABLE B.1 EFFECTIVE ELASTIC PROPERTIES FOR FACESHEETS

Laminate	E_x GPa (Msi)	E_y GPa (Msi)	ν_{xy}	G_{xy} GPa (Msi)
$[0/\pm45]_{2s}$	63.3 (9.18)	27.7 (4.02)	0.69	27.2 (3.94)
$[0/\pm45]_{s}$	63.3 (9.18)	27.7 (4.02)	0.69	27.2 (3.94)
$[\pm45]_{2s}$	21.5 (3.12)	21.5 (3.12)	0.74	37.7 (5.46)
$[90/\pm45]_{s}$	27.7 (4.02)	63.3 (9.18)	0.30	27.2 (3.94)

$$\left[\begin{array}{c|c} \underline{A} & \underline{B} \\ \hline \underline{B} & \underline{D} \end{array}\right] =$$

$$\left[\begin{array}{ccc|ccc} 4.167\times10^{5} & 1.254\times10^{5} & -1.788\times10^{-7} & -1.031\times10^{3} & 3.280\times10^{2} & -3.516\times10^{2} \\ 1.254\times10^{5} & 1.823\times10^{5} & -1.192\times10^{-7} & 3.280\times10^{2} & 3.752\times10^{2} & -3.516\times10^{2} \\ -1.788\times10^{-7} & -1.192\times10^{-7} & 1.417\times10^{5} & -3.516\times10^{2} & -3.516\times10^{2} & 3.280\times10^{2} \\ \hline -1.031\times10^{3} & 3.280\times10^{2} & -3.516\times10^{2} & 4.707\times10 & 1.288\times10 & -2.110 \\ 3.280\times10^{2} & 3.752\times10^{2} & -3.516\times10^{2} & 1.288\times10 & 1.894\times10 & -2.110 \\ -3.516\times10^{2} & -3.516\times10^{2} & 3.280\times10^{2} & -2.110 & -2.110 & 1.465\times10 \end{array}\right]$$

FIGURE B.1 CONSTITUTIVE MATRIX FOR [0/±45/0/±45]
(English Units)

$$\begin{bmatrix} \underline{A} & \underline{B} \\ \hline \underline{B} & \underline{D} \end{bmatrix} =$$

$$\left[\begin{array}{ccc|ccc} 2.084\times10^{5} & 6.268\times10^{4} & -1.788\times10^{-7} & -5.156\times10^{2} & 1.640\times10^{2} & -1.758\times10^{2} \\ 6.268\times10^{4} & 9.115\times10^{4} & -1.192\times10^{-7} & 1.640\times10^{2} & 1.876\times10^{2} & -1.758\times10^{2} \\ -1.788\times10^{-7} & -1.192\times10^{-7} & 7.087\times10^{4} & -1.758\times10^{2} & -1.758\times10^{2} & 1.640\times10^{2} \\ \hline -5.156\times10^{2} & 1.640\times10^{2} & -1.758\times10^{2} & 6.657 & 1.364 & -1.055 \\ 1.640\times10^{2} & 1.876\times10^{2} & -1.758\times10^{2} & 1.364 & 2.086 & -1.055 \\ -1.758\times10^{2} & -1.758\times10^{2} & 1.640\times10^{2} & -1.055 & -1.055 & 1.586 \end{array}\right]$$

FIGURE B.2 CONSTITUTIVE MATRIX FOR [0/45/-45]
(English Units)

$$\left[\begin{array}{c|c} \underline{A} & \underline{B} \\ \hline \underline{B} & \underline{D} \end{array}\right] =$$

$$\left[\begin{array}{ccc|ccc} 1.632\times10^{5} & 1.200\times10^{5} & -2.384\times10^{-7} & 9.313\times10^{-10} & -9.313\times10^{-10} & -3.516\times10^{2} \\ 1.200\times10^{5} & 1.632\times10^{5} & -2.980\times10^{-7} & 0 & 0 & -3.516\times10^{2} \\ -2.384\times10^{-7} & -2.980\times10^{-7} & 1.309\times10^{5} & -3.516\times10^{2} & -3.516\times10^{2} & 9.313\times10^{-10} \\ \hline 9.313\times10^{-10} & -9.313\times10^{-10} & -3.516\times10^{2} & 7.835 & 5.761 & -2.910\times10^{-11} \\ 0 & 0 & -3.516\times10^{2} & 5.761 & 7.835 & -1.455\times10^{-11} \\ -3.516\times10^{2} & -3.516\times10^{2} & 9.313\times10^{-10} & -2.910\times10^{-11} & -1.455\times10^{-11} & 6.285 \end{array}\right]$$

FIGURE B.3 CONSTITUTIVE MATRIX FOR [±45/±45]
(English Units)

$$\left[\begin{array}{c|c} \underline{A} & \underline{B} \\ \hline \underline{B} & \underline{D} \end{array}\right] =$$

$$\left[\begin{array}{ccc|ccc} 9.115\times10^{4} & 6.268\times10^{4} & -2.384\times10^{-7} & 1.876\times10^{2} & 1.640\times10^{2} & -1.758\times10^{2} \\ 6.268\times10^{4} & 2.084\times10^{5} & -1.490\times10^{-6} & 1.640\times10^{2} & -5.156\times10^{2} & -1.758\times10^{2} \\ -2.384\times10^{-7} & -1.490\times10^{-6} & 7.087\times10^{4} & -1.758\times10^{2} & -1.758\times10^{2} & 1.640\times10^{2} \\ \hline 1.876\times10^{2} & 1.640\times10^{2} & -1.758\times10^{2} & 2.086 & 1.364 & -1.055 \\ 1.640\times10^{2} & -5.156\times10^{2} & -1.758\times10^{2} & 1.364 & 4.457 & -1.055 \\ -1.758\times10^{2} & -1.758\times10^{2} & 1.640\times10^{2} & -1.055 & -1.055 & 1.586 \end{array}\right]$$

FIGURE B.4 CONSTITUTIVE MATRIX FOR [90/±45]
(English Units)

TABLE B.2 REDUCED BENDING STIFFNESS TERMS

$$[\underline{D}]^{*} = [\underline{D}] - [\underline{B}][\underline{A}]^{-1}[\underline{B}]$$

Laminate	D_{11}^{*} (lbs-in)	D_{22}^{*} (lbs-in)	D_{12}^{*} (lbs-in)	D_{66}^{*} (lbs-in)
[0/±45/0/±45]	40.82	17.28	11.60	13.21
[0/±45]	3.54	1.26	0.72	0.85
[±45/±45]	6.89	6.89	4.82	5.41
[90/±45]	1.26	3.54	0.72	0.85

APPENDIX C

Load-Strain Data for Representative Samples

Each laminate configuration exhibited unique load-strain response. The beams which did not contain implanted defects were instrumented with transverse gages to measure the Poisson strain. The beams with defects were instrumented in the load direction only.

The load axis for all the curves correspond to the machine load. This machine load, which is the value taken from the Instron chart, can be converted to laminate average stress by considering the geometry of the test fixture and the specimen dimensions. However, the primary interest is not in generating stress-strain data; rather, the main benefit of the load-strain plots is that they allow detection of defect buckling.

The longitudinal gage on the compressive face is mounted centrally over the disbond region. Upon the application of load the gage monitors the compressive strain, and if the defect is initially flat and smooth, uniformly increasing strain is obtained. When the circular region above the

disbond reaches its critical load it buckles outward with a corresponding strain reversal. This strain reversal is clearly evident on the load-strain curve and the appropriate buckling load can be determined.

Representative load-strain curves for each undamaged configuration are presented in Figures C.1 through C.4. The load-strain curves for the 12 ply $[0/\pm45]_{2s}$ and 6 ply $[0/\pm45]_{s}$ exhibit similar characteristics. The curves show the small differences in the elastic properties of the tensile and compressive facesheets (same stacking sequence; different material systems). Also apparent are the large Poisson's ratios for each face (on the order of 0.7). This effect would prove important if designing a sandwich structure for stiffness. The small nonlinearity at higher loads may be attributed to material nonlinearity and possible curvature induced strains.

The $[90/\pm45]_{s}$, 6 ply samples exhibited linear response up until failure. The stiffness differences between the faces is evident and a large Poisson strain is also indicated.

Figure C.4 clearly shows the reasoning behind using a very stiff $[0°]_{16}$ tensile face for the $[\pm45]_{2s}$ tests. The strain to failure for the [±45] laminate is upwards of 0.05

for the tests run. To prevent excessive deflections the 0° tensile face was used to shift the neutral axis of bending. The nonlinear behavior is characteristic of [±45] laminates.

Load-strain curves, covering the range of defect diameters for the 12 ply and 6 ply $[0/\pm45]_{ns}$ samples, are presented in Figure C.5 through C.10. As previously noted, buckling loads are easily determined. Figures C.11 and C.12 present the strain response of two $[\pm45]_{2s}$ test beams. The results show that the response is indistinguishable over the range of disbond diameters and defect types. A clear shift in failure mode occurs about the one inch defect but no influence on ultimate load is detected.

Figure C.13 and C.14 illustrate the response of the $[90/\pm45]_{s}$ laminate and complete the set of examples. The half-inch and one-inch defect samples exhibit less sudden strain reversal than the respective $[0/\pm45]_{s}$ panels but the relative magnitudes are approximately equivalent. The two-inch diameter defect samples exhibited a unique response. This result probably arose from initial irregularities in the disbond shape; i.e., deflections in the circular plate as a result of curing stresses.

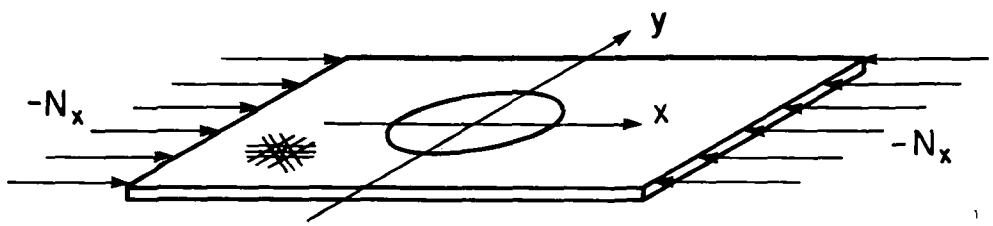

FIGURE 2.1 DISBOND LOAD GEOMETRY

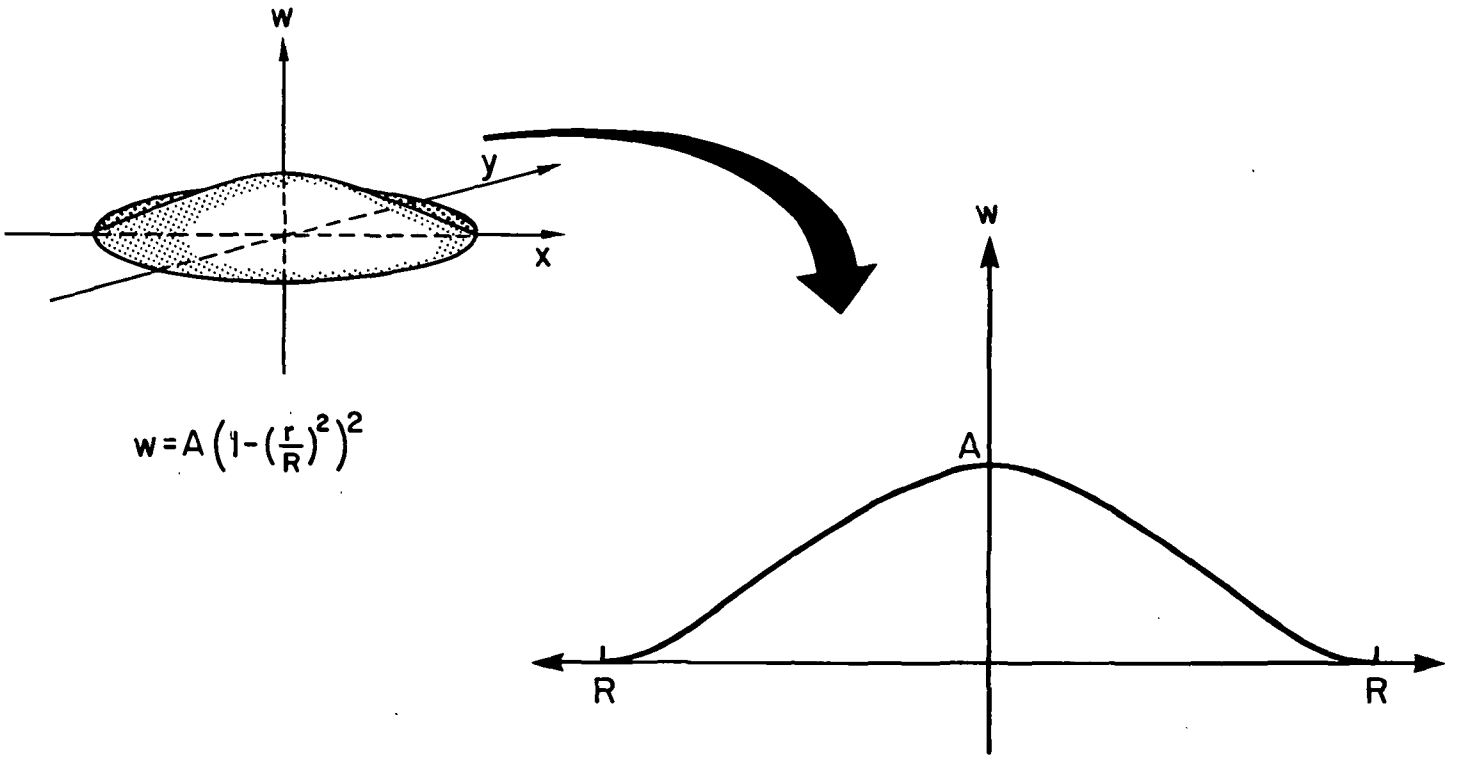

FIGURE 2.2 APPROXIMATE BUCKLING SHAPE FOR RAYLEIGH-RITZ APPROXIMATION

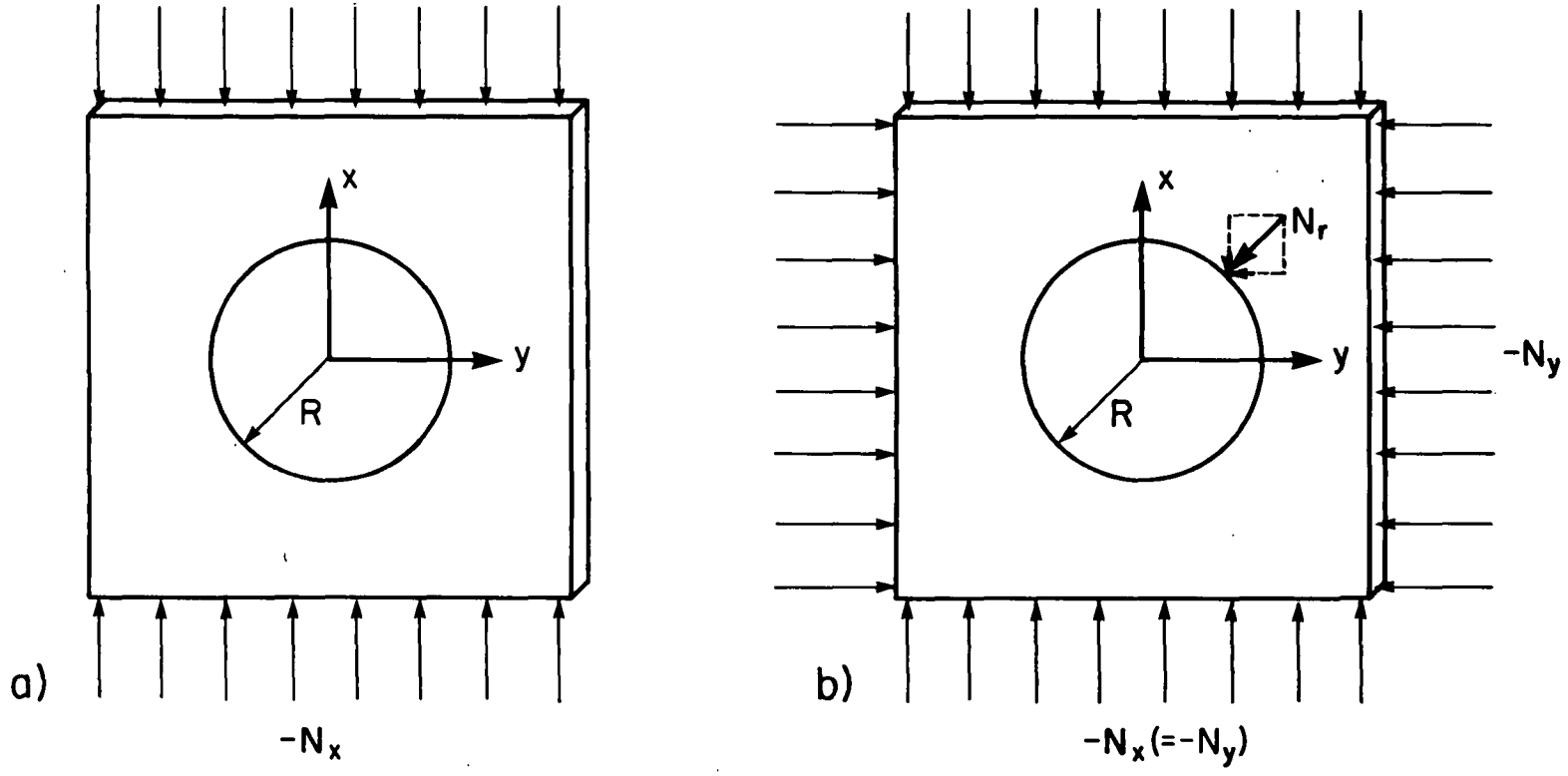

$$N_{x_{approx}} = \frac{-32D}{R^2}$$

$$N_{x_{approx}} = \frac{-16D}{R^2}$$

$$N_{x_{exact}} = \frac{-14.68D}{R^2}$$

FIGURE 2.3 DISK LOAD GEOMETRY AND BUCKLING CONDITIONS

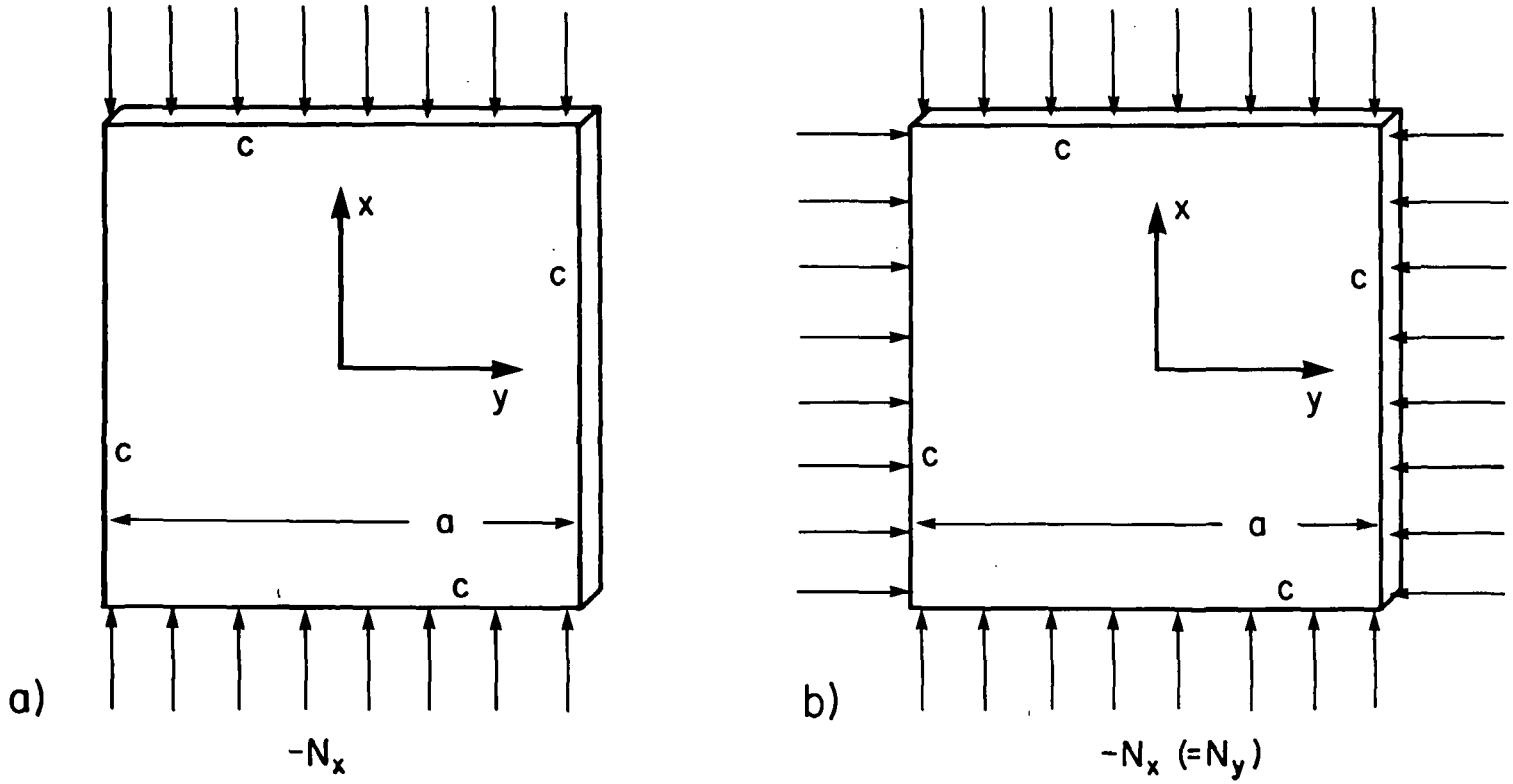

$$N_{x_{approx}} = \frac{-10.67\pi^2 D}{a^2}$$

$$N_{x_{exact}} = \frac{-10.07\pi^2 D}{a^2}$$

$$N_{x_{approx}} = \frac{-5.33\pi^2 D}{a^2}$$

$$N_{x_{exact}} = \frac{-5.31\pi^2 D}{a^2}$$

FIGURE 2.4 BUCKLING LOADS FOR A CLAMPED SQUARE PLATE

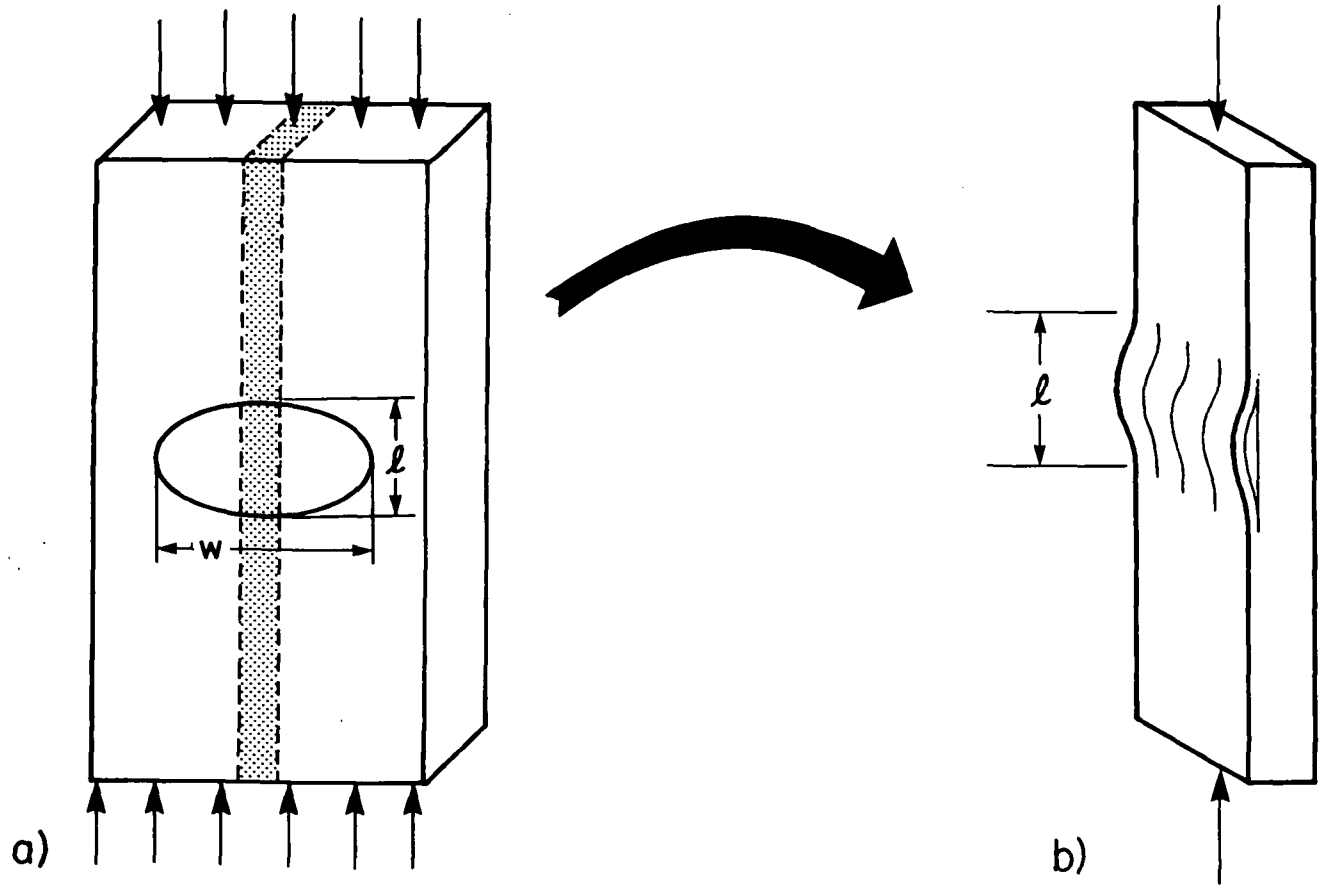

FIGURE 2.5 THIN FILM FRACTURE MECHANICS PROBLEM

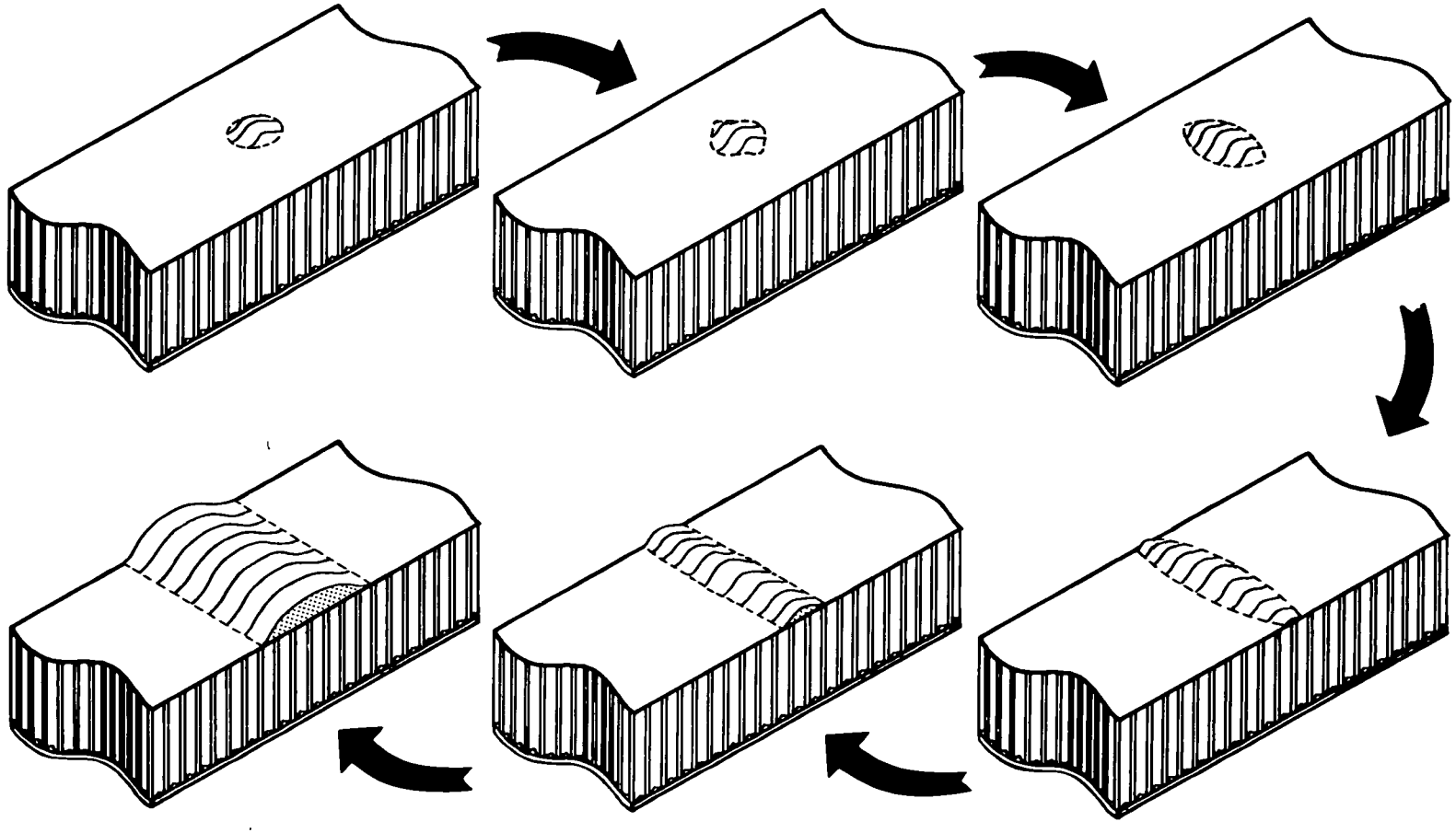

FIGURE 2.6 DISBOND PROPAGATION SEQUENCE

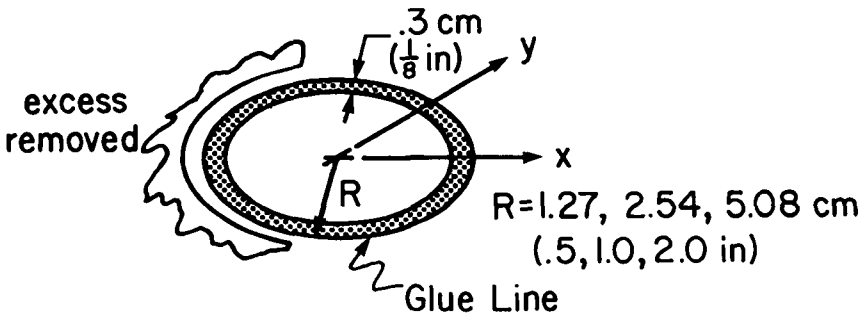

FIGURE 3.1 KAPTON BAG DEFECT GEOMETRY

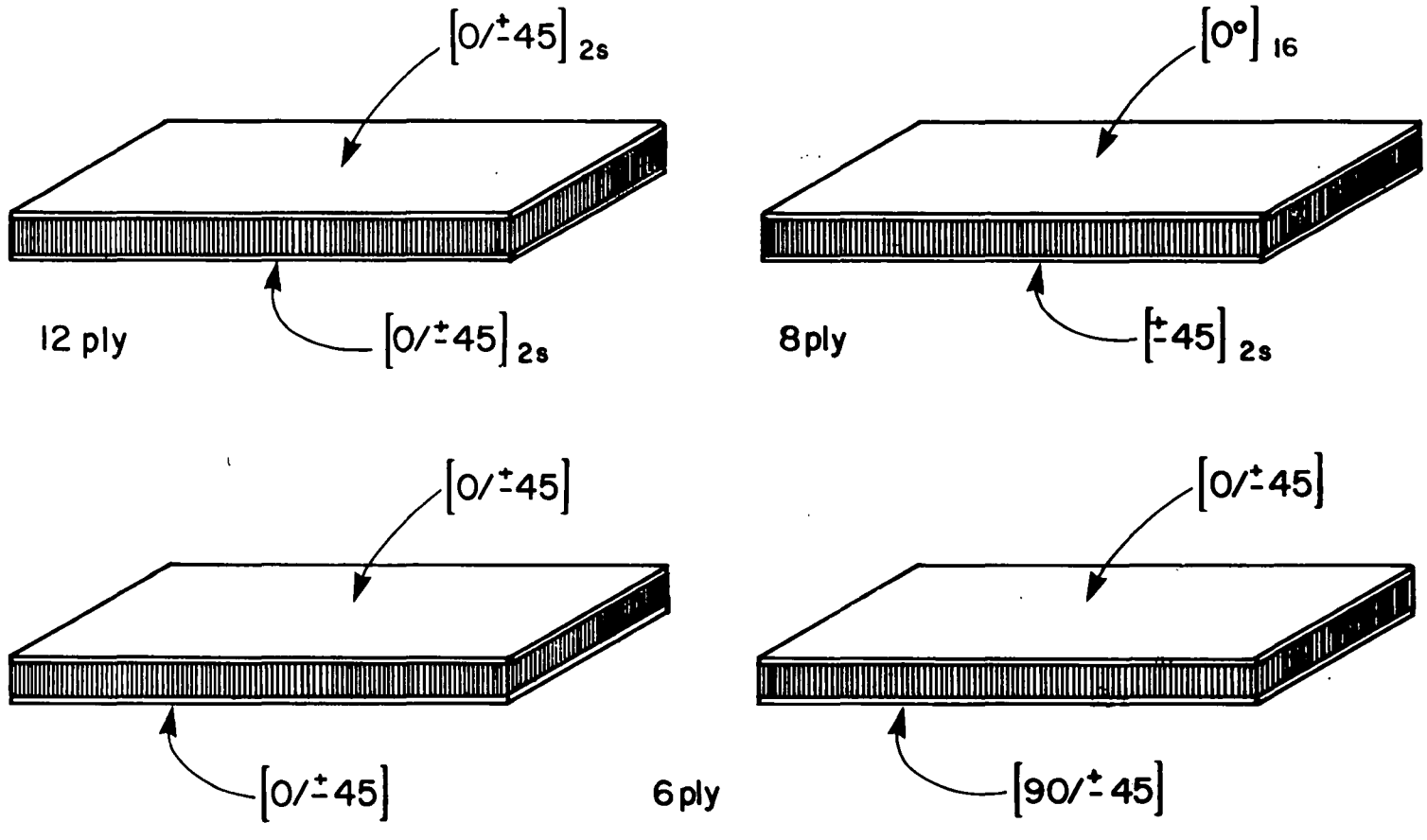

FIGURE 3.2 FACING PAIRS FOR EXPERIMENTAL PROGRAM
(Compressive face on bottom)

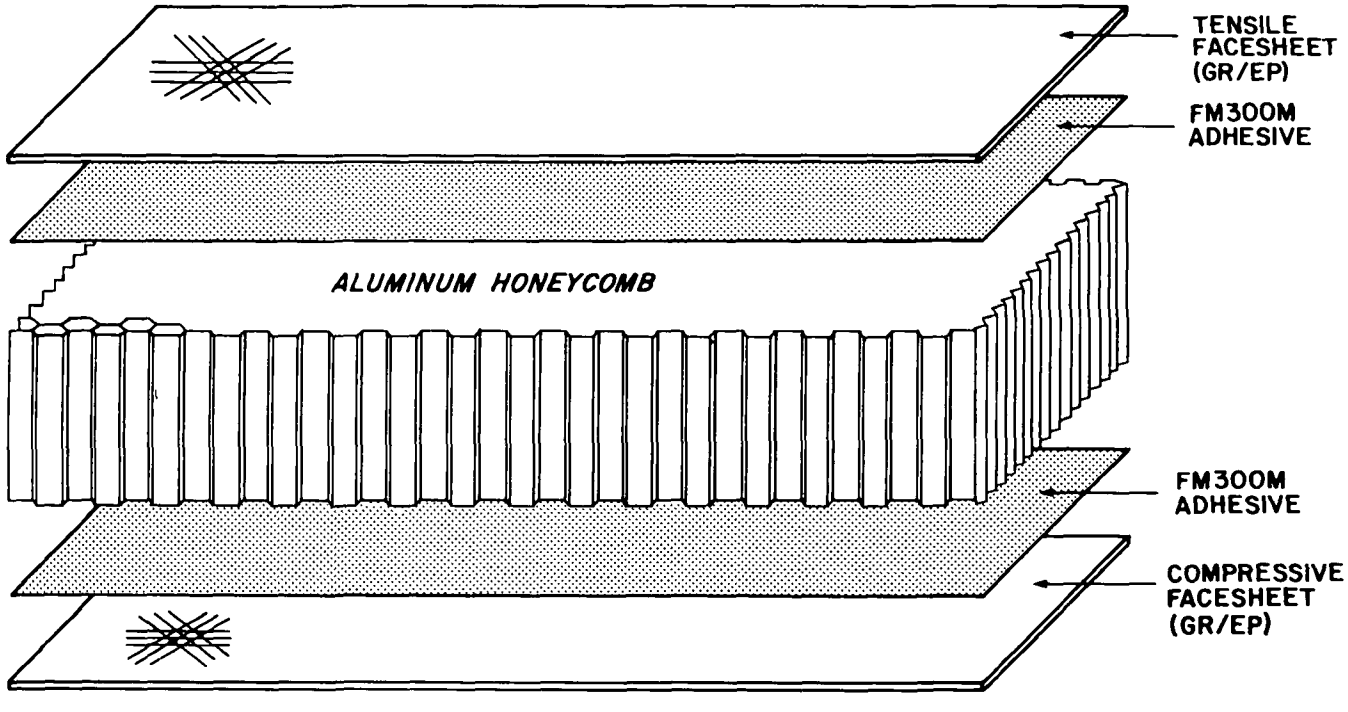

FIGURE 3.3 SANDWICH CONSTRUCTION

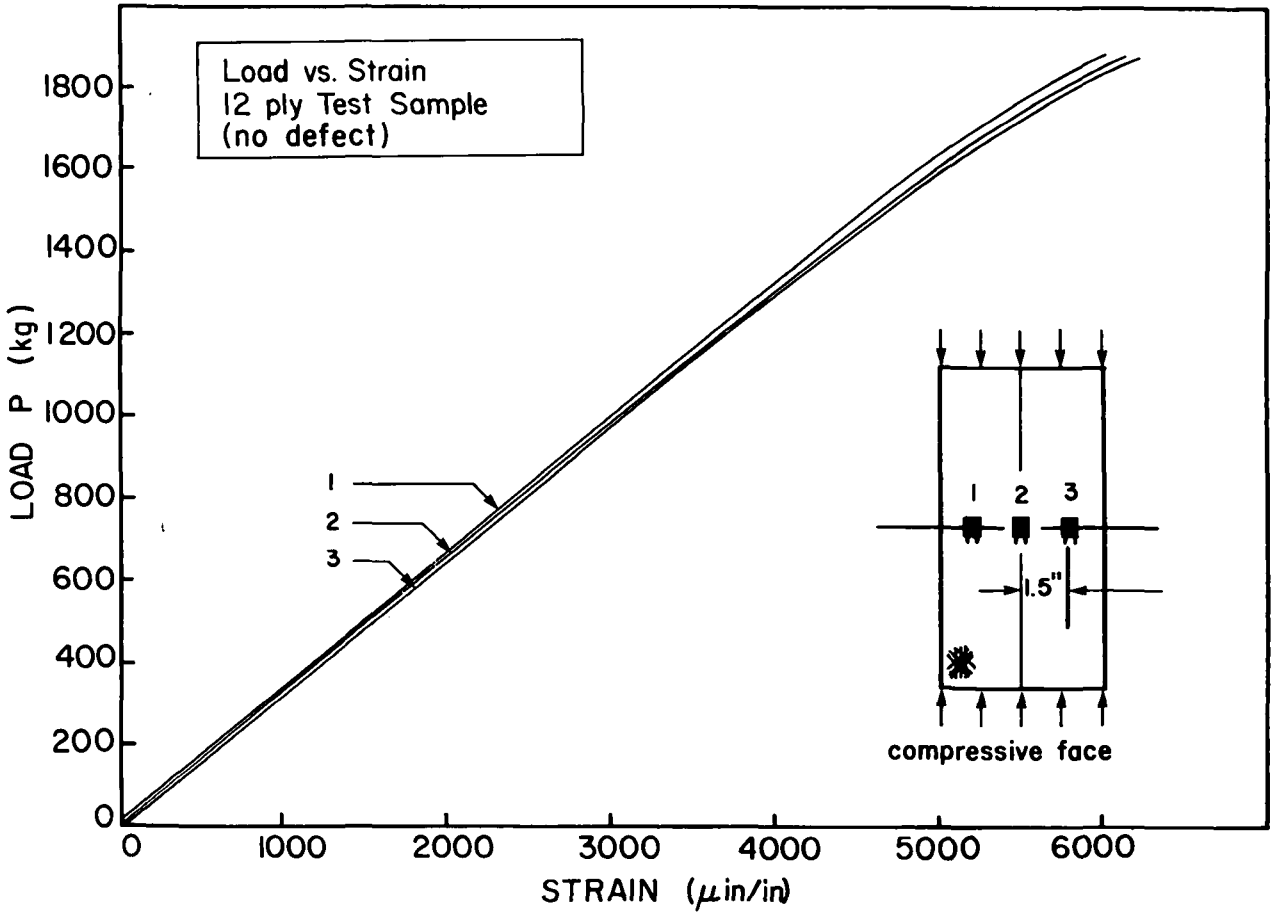

FIGURE 3.4 VERIFICATION OF LOAD UNIFORMITY -- TRANSVERSE TO CENTERLINE OF TEST SECTION

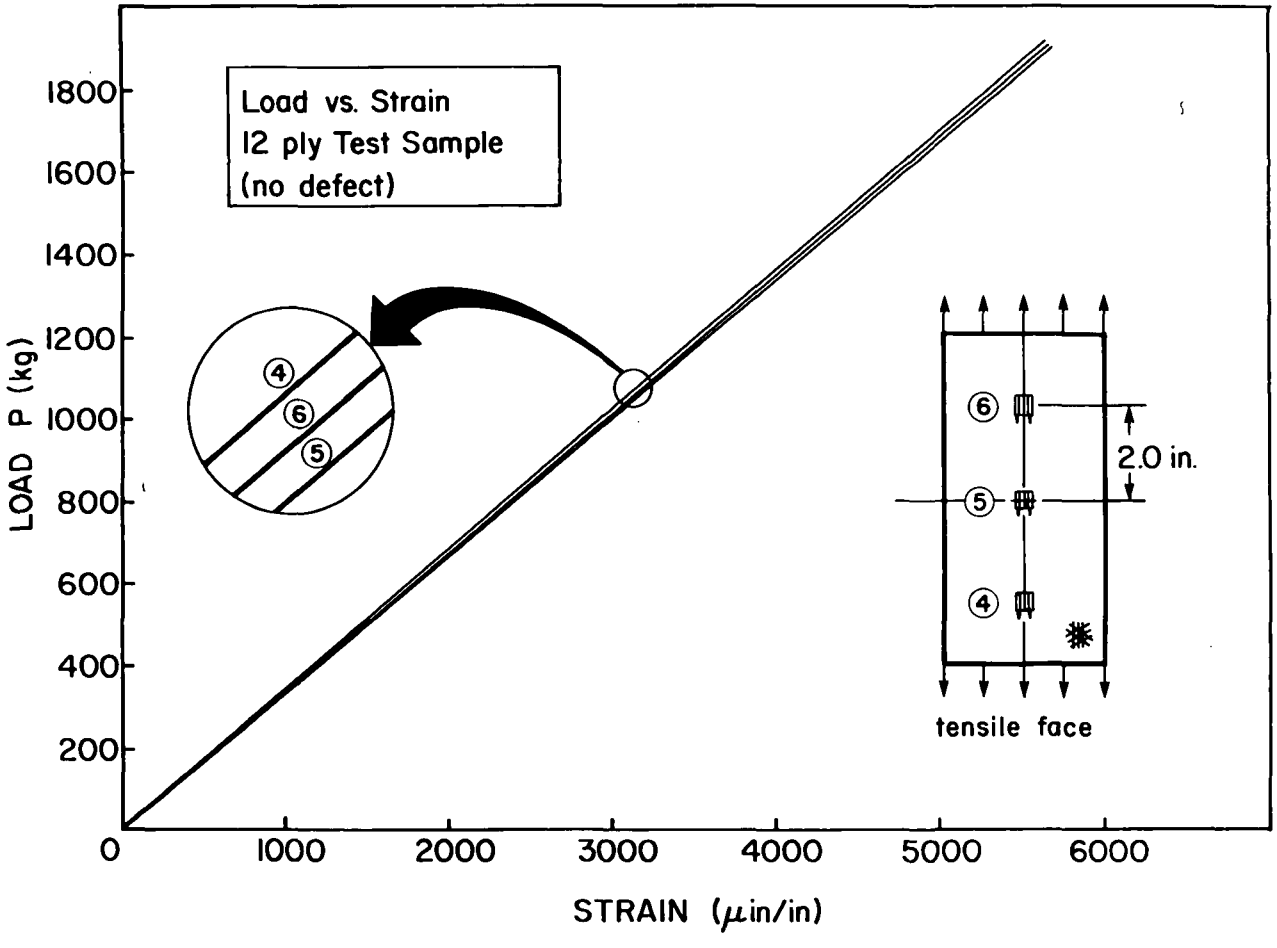

FIGURE 3.5 VERIFICATION OF LOAD UNIFORMITY -- ALONG CENTERLINE OF TEST SECTION

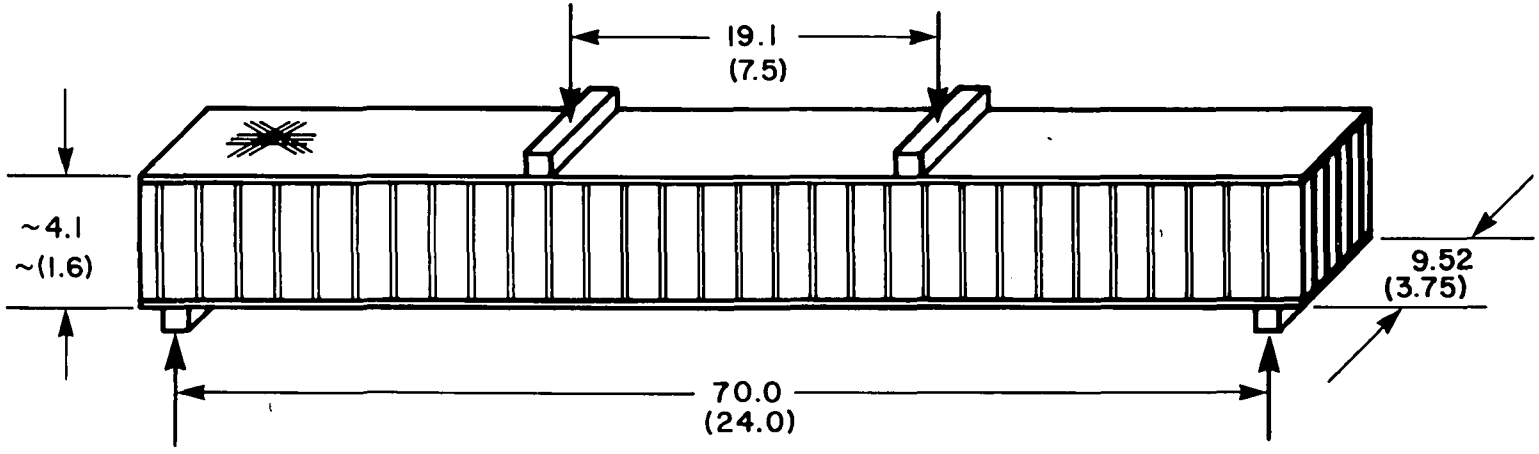

NOTES: 1. LOADING PADS ARE 1.905 cm (.75 in) WIDE ALUMINUM
2. ACTUAL HEIGHT IS DETERMINED BY FACE THICKNESS
3. OVERALL BEAM LENGTH (PLUS OVERHANG) IS 66.0 cm (26.0 in)

FIGURE 3.6 TEST SAMPLE LOAD GEOMETRY

FIGURE 3.7 EXPERIMENTAL SET-UP

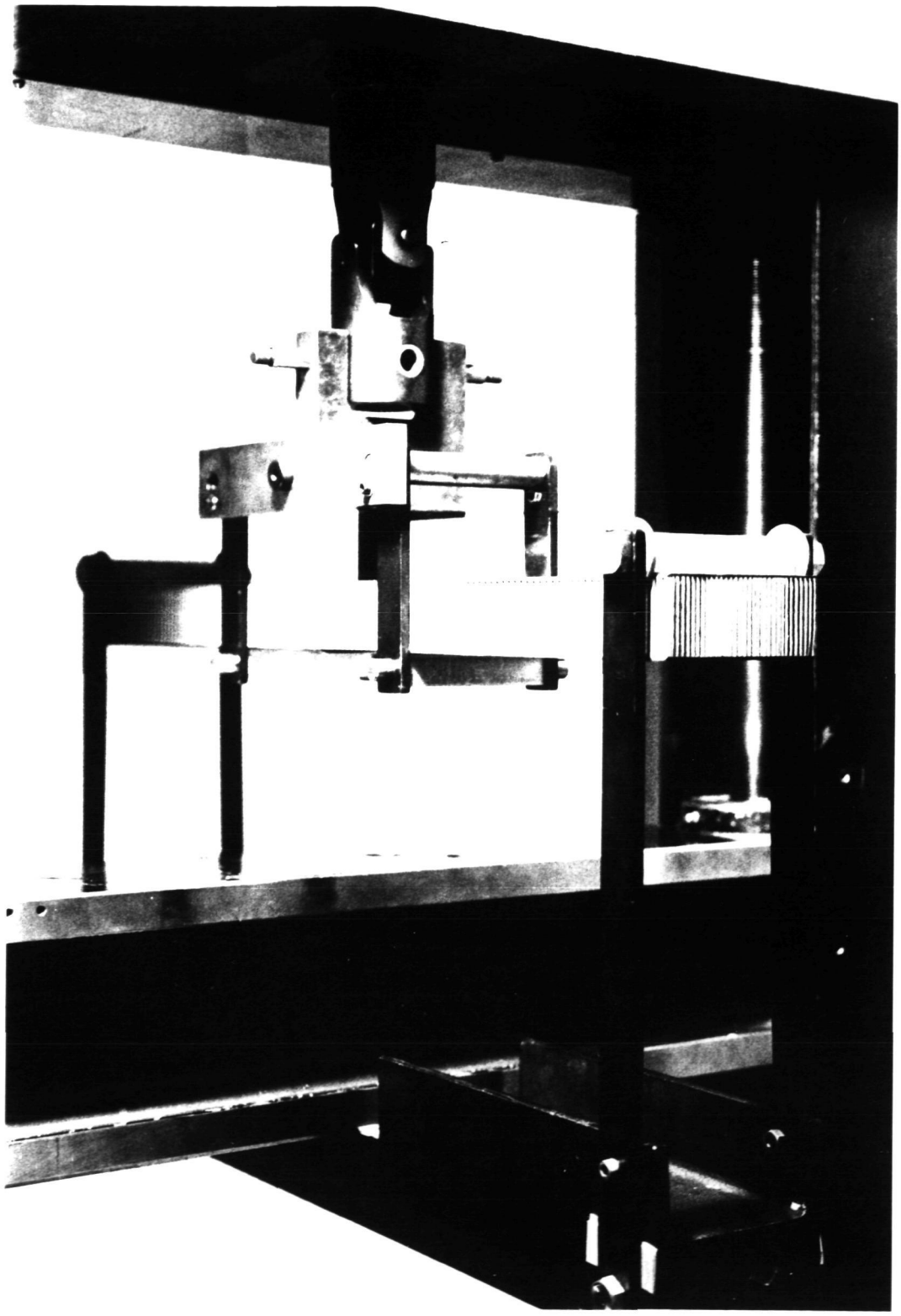

FIGURE 3.8 CLOSE-UP OF TEST FIXTURE

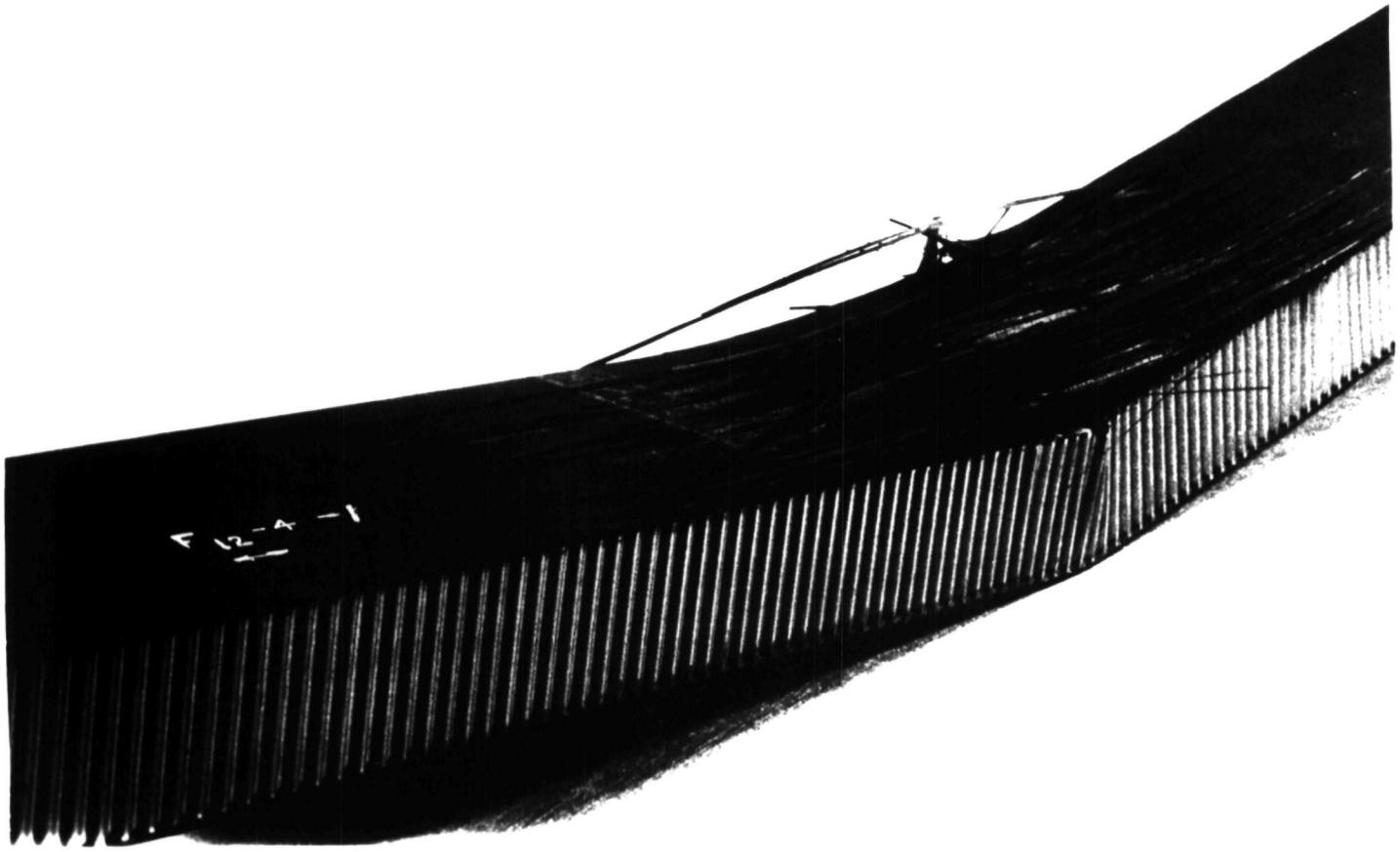

FIGURE 3.9 CHARACTERISTIC COMPRESSION FAILURE MODE
(12-PLY FACESHEET)

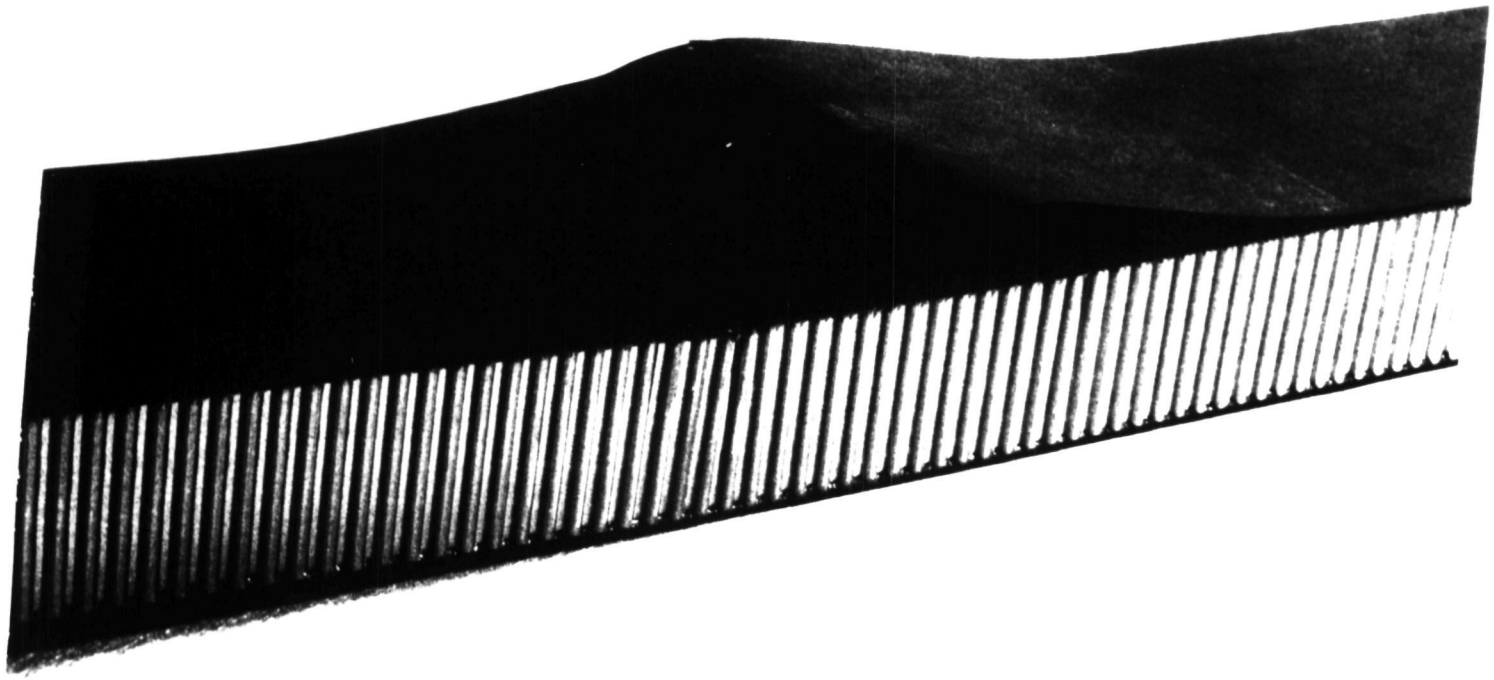

FIGURE 3.10 CHARACTERISTIC COMPRESSION BUCKLING FAILURE MODE (12-PLY FACESHEET)

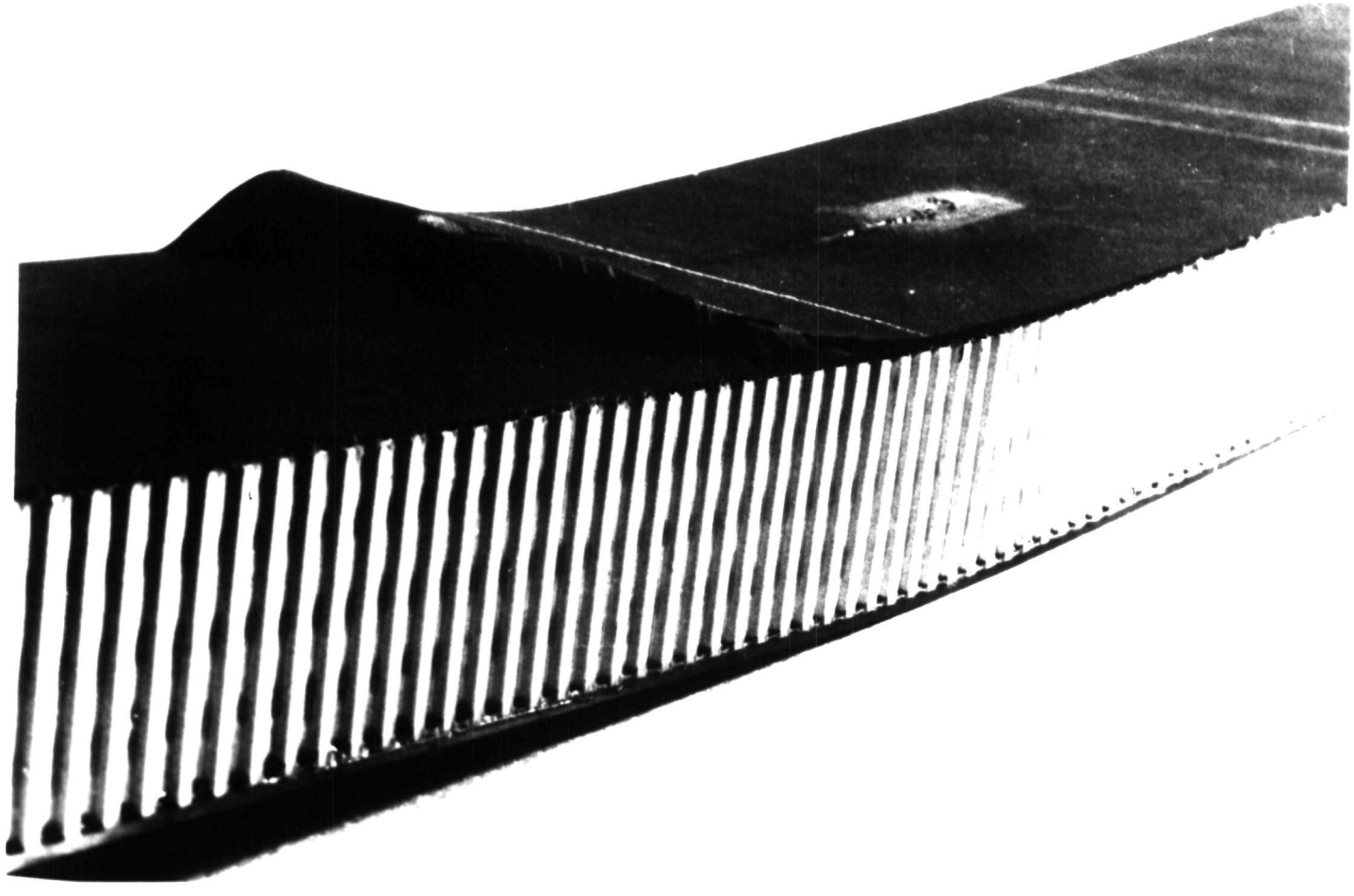

FIGURE 3.11 CHARACTERISTIC CONCENTRATED LOAD FAILURE MODE (8-PLY FACESHEET)

Page Intentionally Left Blank

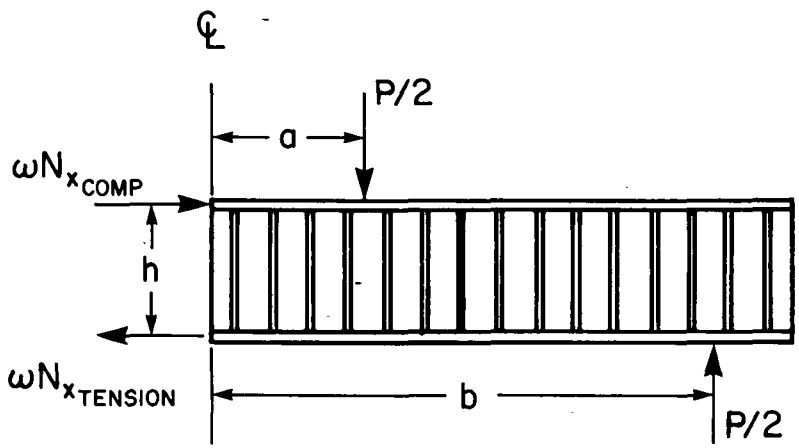

FIGURE 4.1 FREE BODY DIAGRAM OF HALF A SANDWICH BEAM

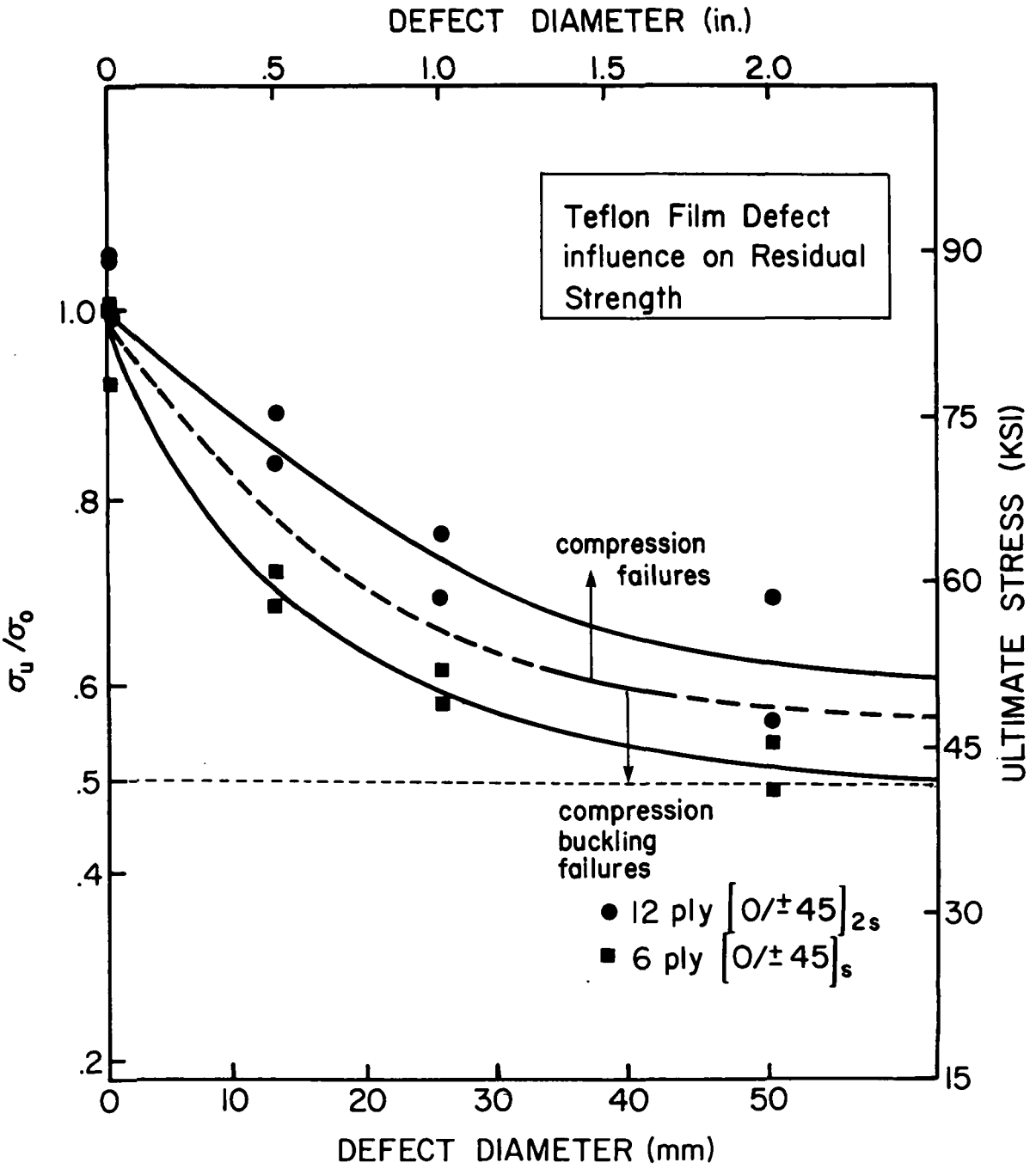

FIGURE 4.2 EFFECT OF LAMINATE THICKNESS ON RESIDUAL STRENGTH OF THE $[0/\pm45]_{ns}$ LAMINATE

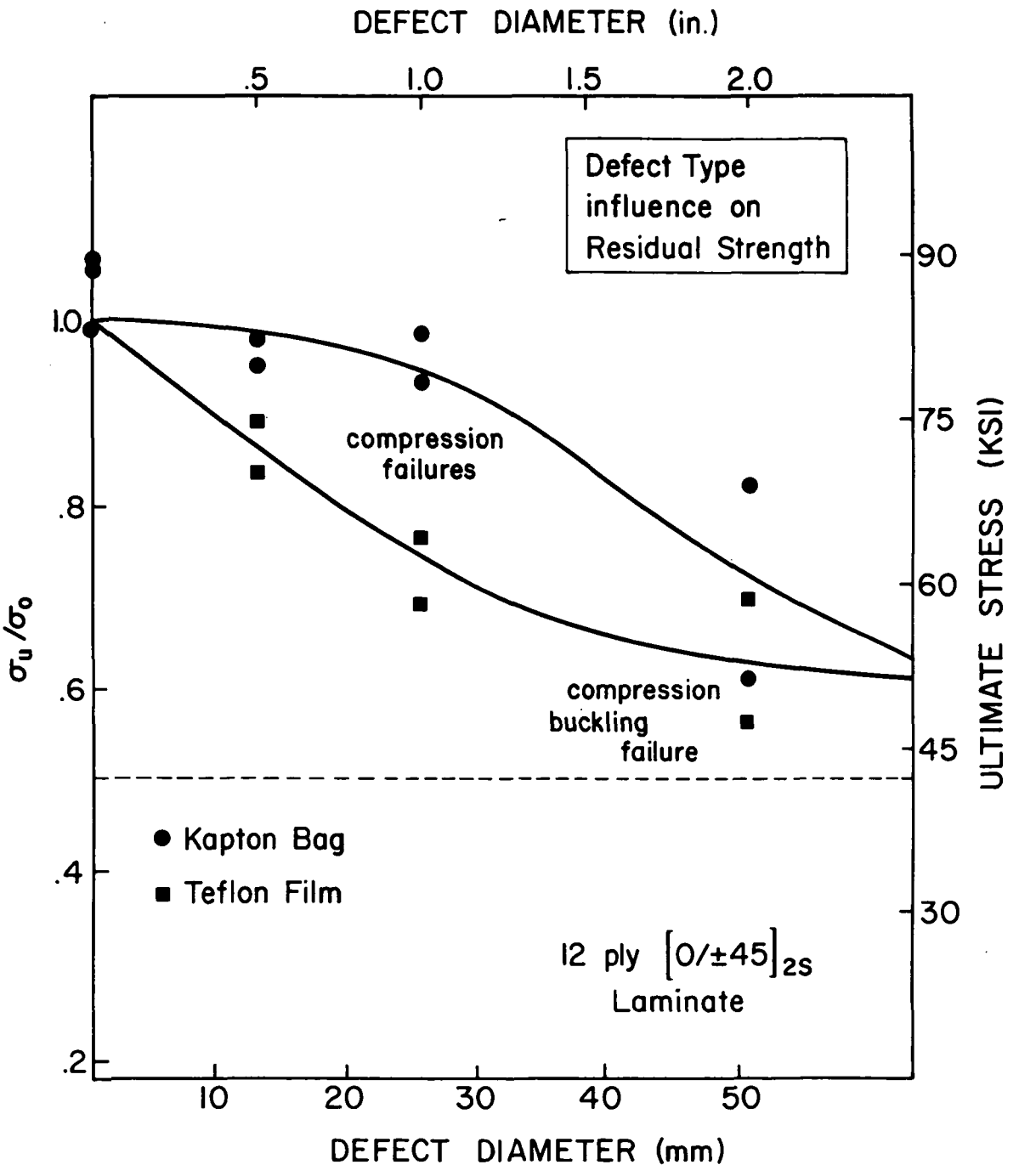

FIGURE 4.3 EFFECT OF DEFECT TYPE ON RESIDUAL STRENGTH OF THE $[0/\pm45]_{2s}$ LAMINATE

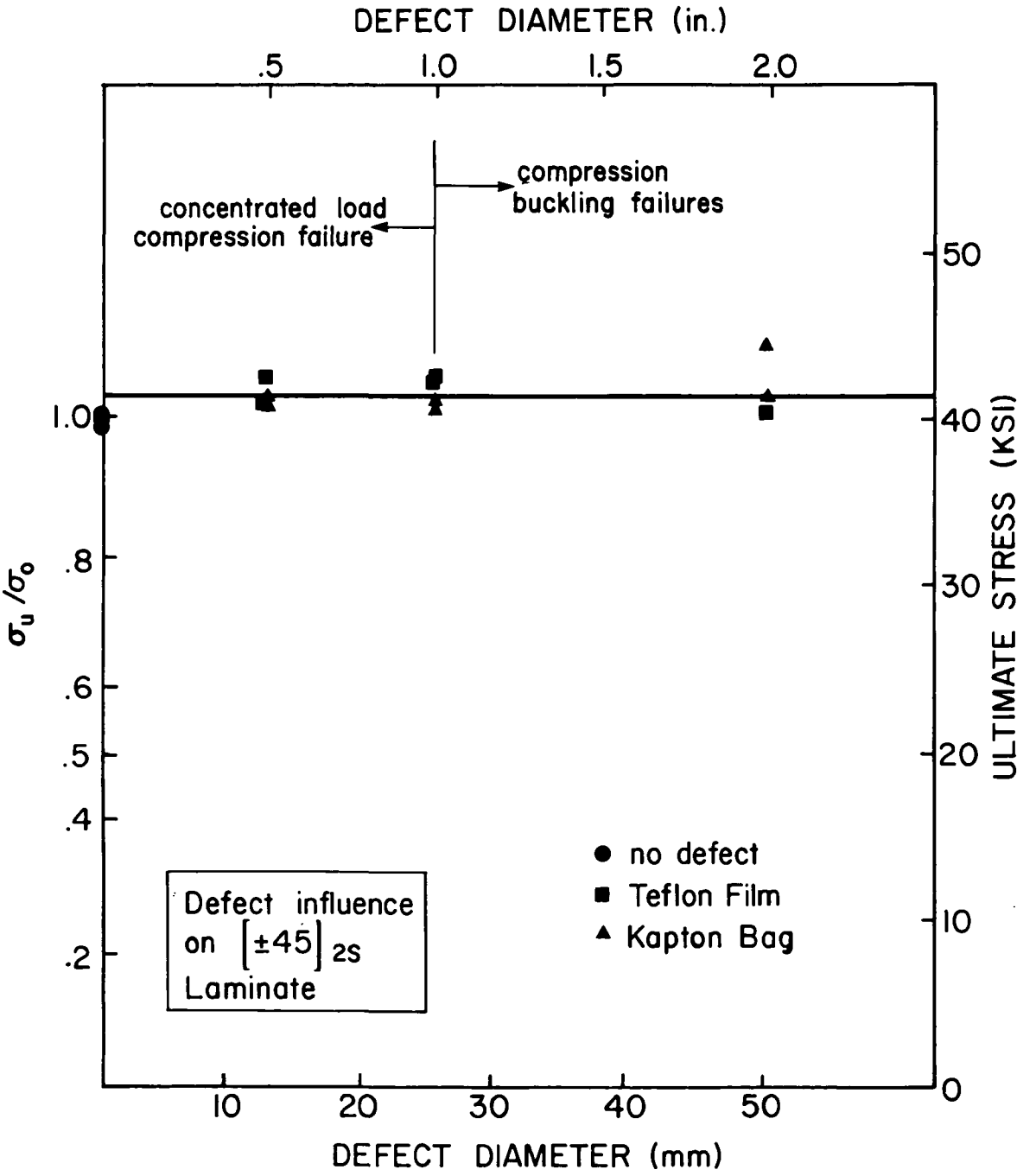

FIGURE 4.4 INFLUENCE OF KAPTON BAG AND TEFLON FILM DEFECTS ON RESIDUAL STRENGTH OF THE $[\pm 45]_{2s}$ LAMINATE

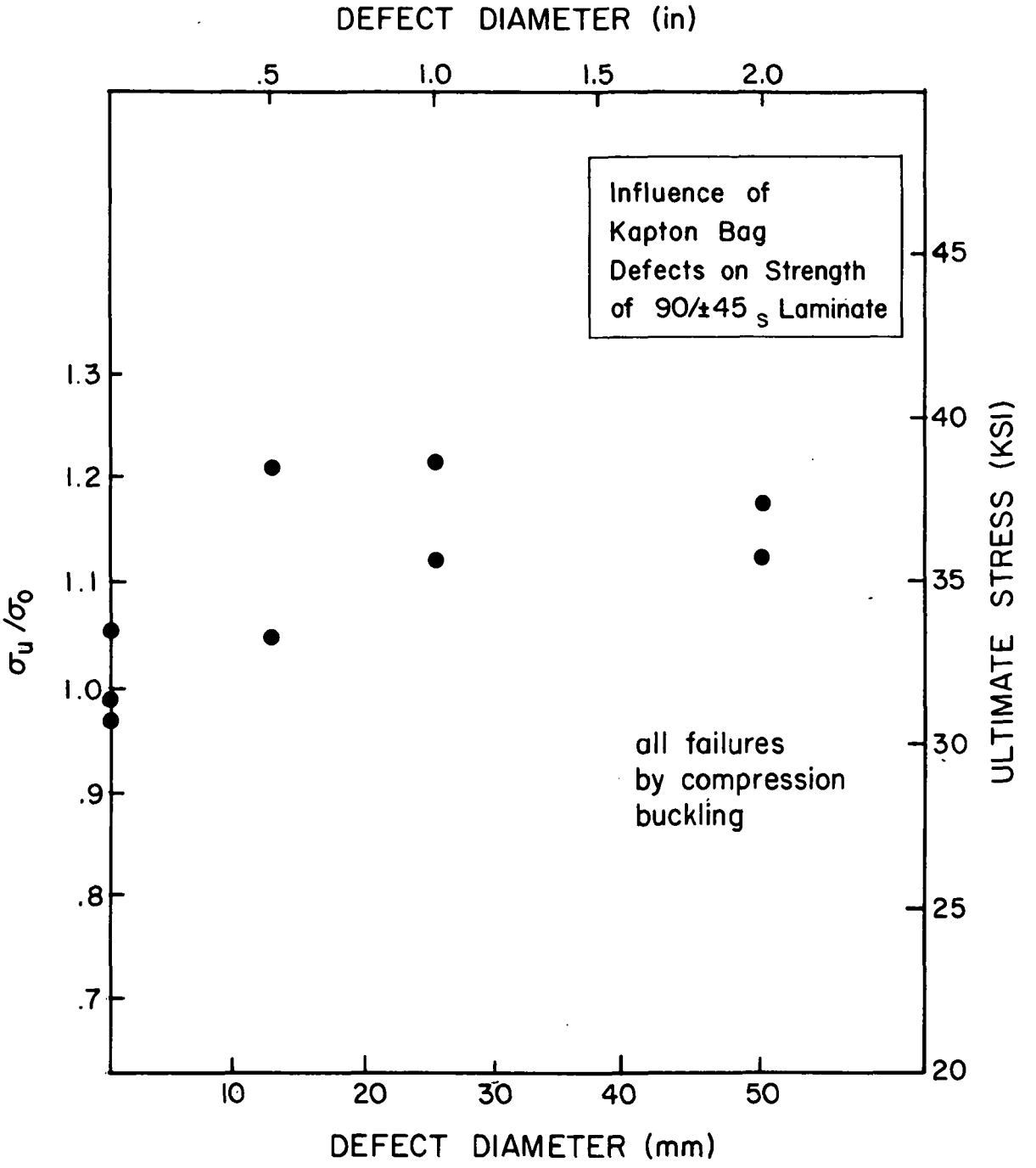

FIGURE 4.5 RESIDUAL STRENGTH OF THE $[90/\pm45]_s$ LAMINATE

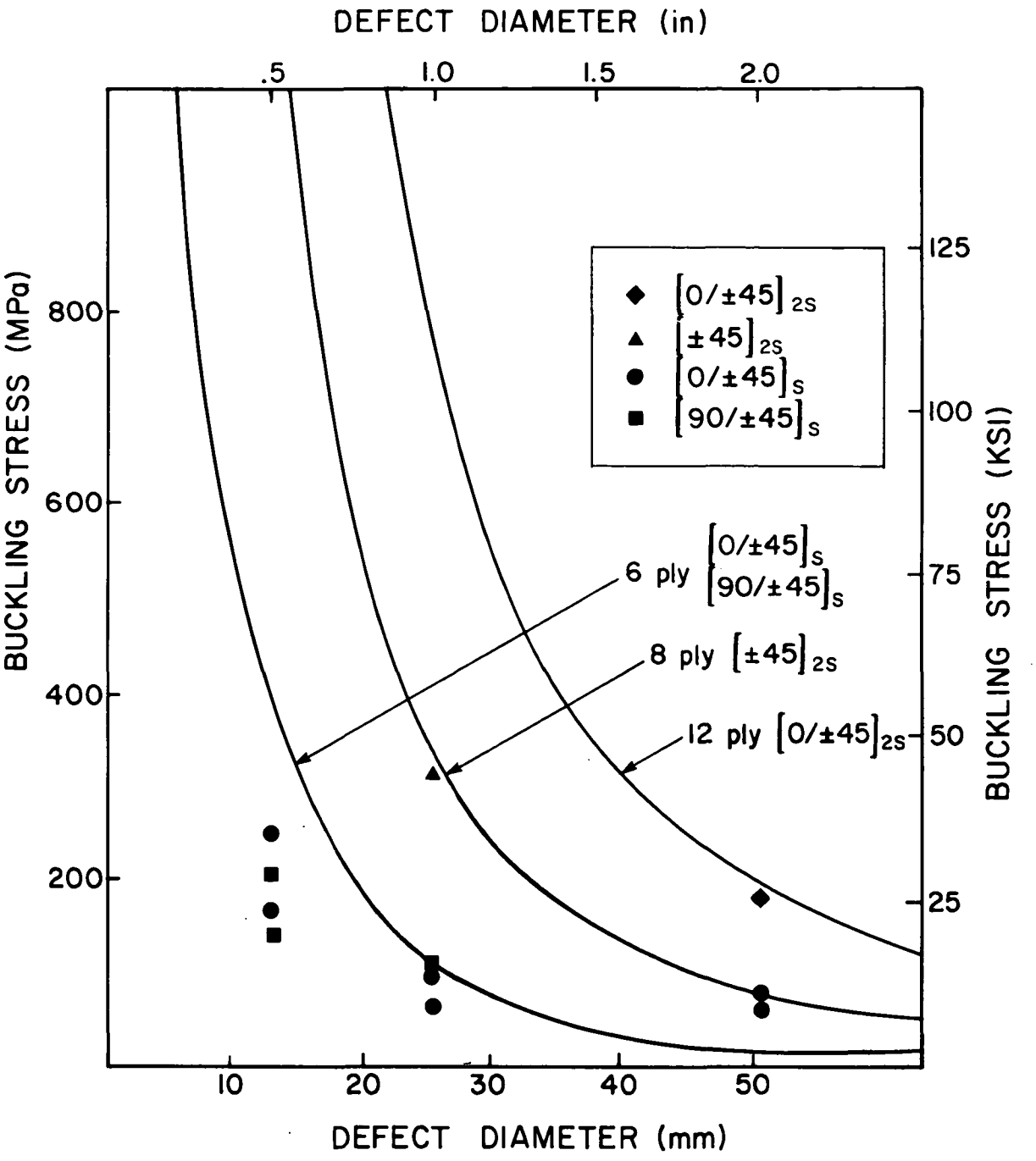

FIGURE 4.6 BUCKLING STRESS VS. DEFECT DIAMETER FOR ALL LAMINATES

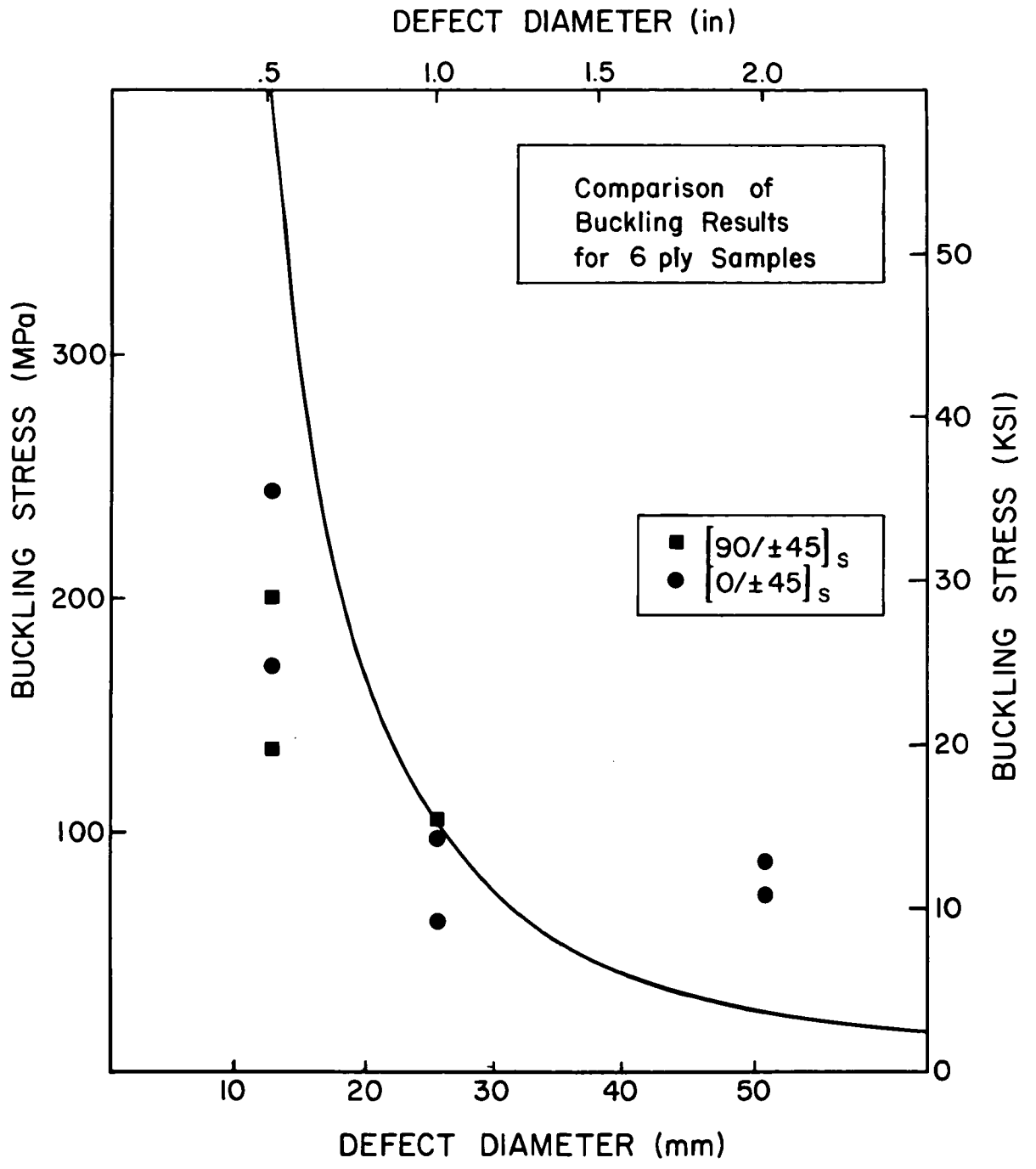

FIGURE 4.7 BUCKLING RESULTS FOR 6-PLY LAMINATES

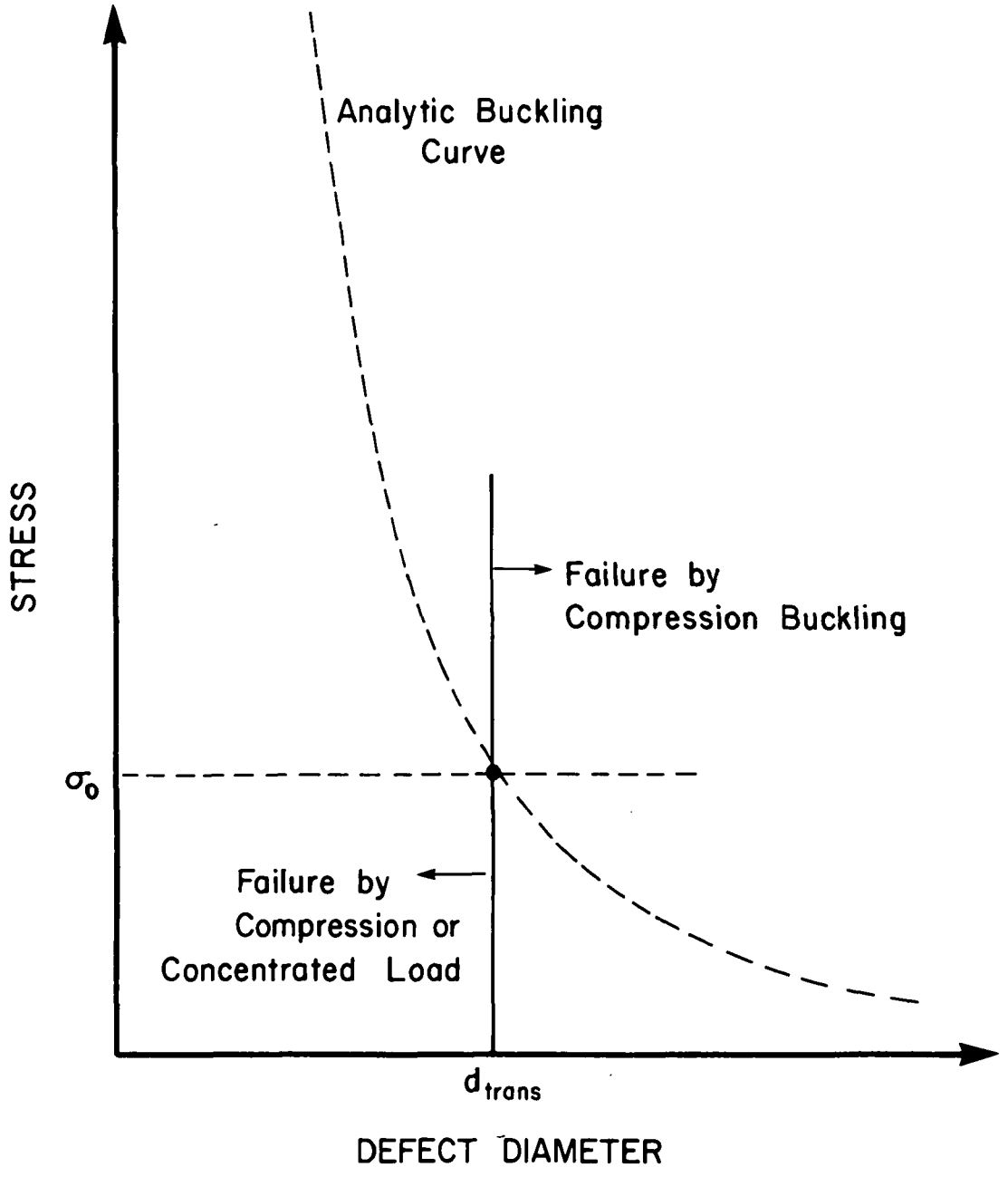

FIGURE 4.8 TECHNIQUE FOR DETERMINING FAILURE MODE TRANSITION

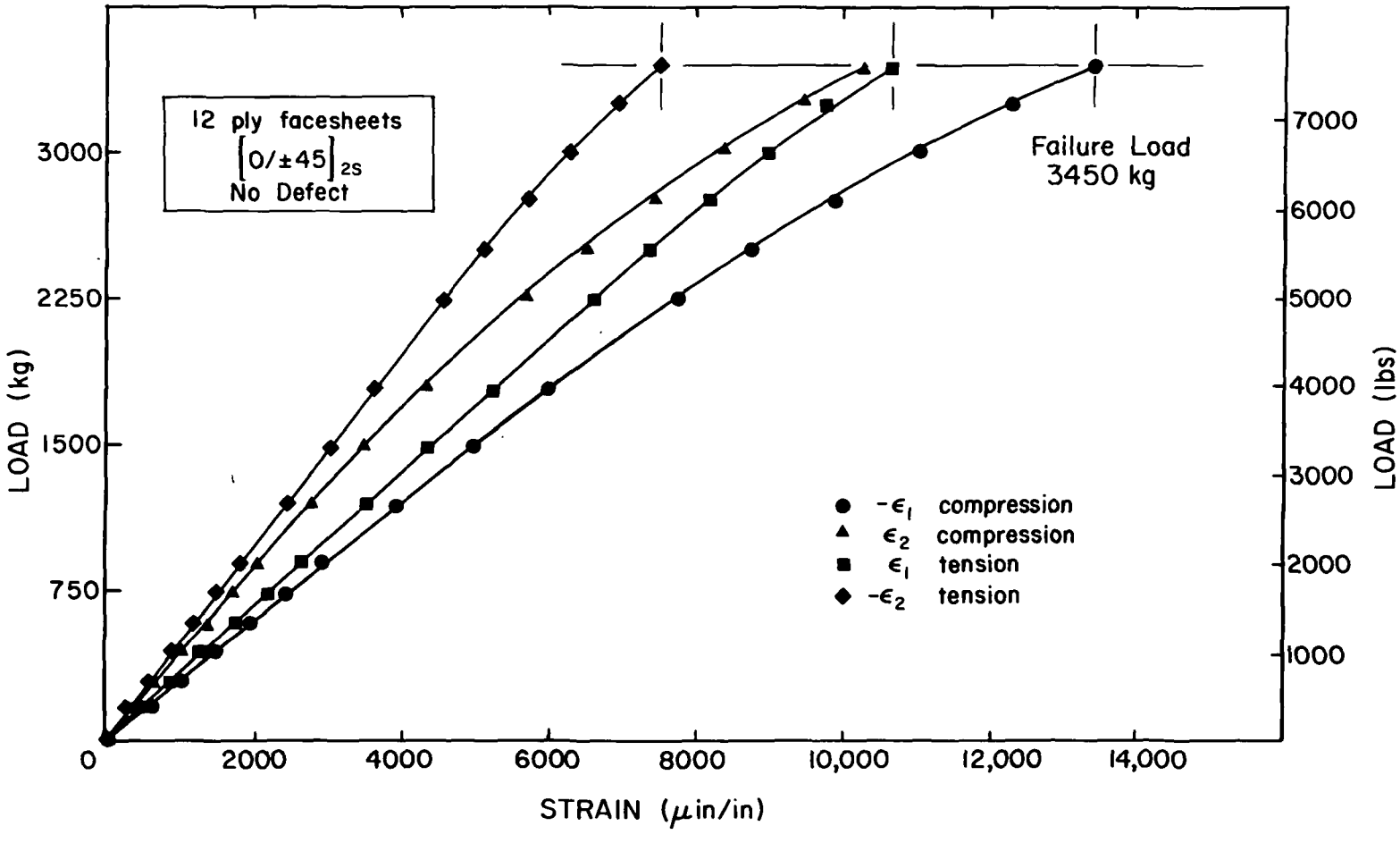

FIGURE C.1 LOAD VS. STRAIN - SAMPLE F_{12}-0-2

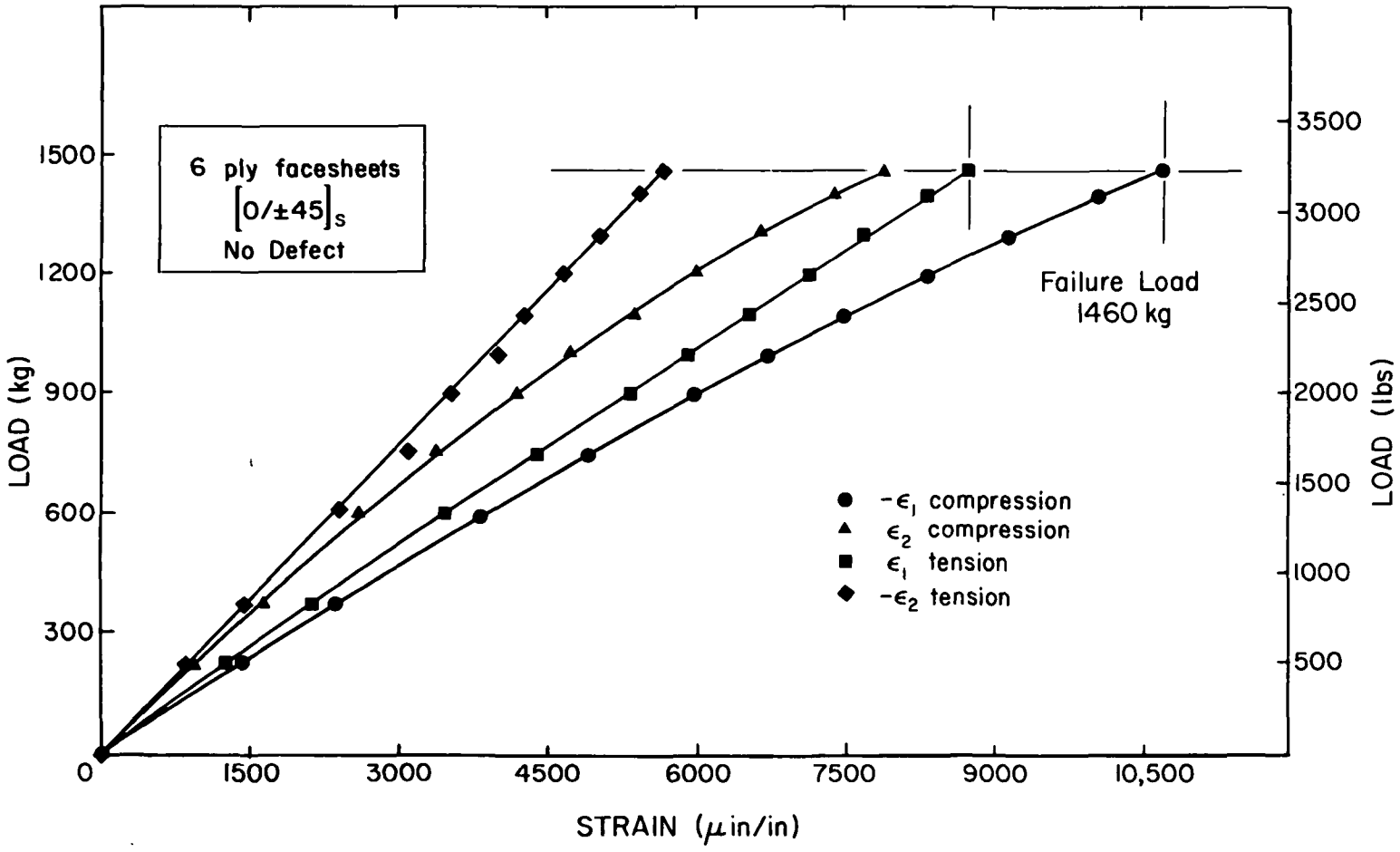

FIGURE C.2 LOAD VS. STRAIN - SAMPLE F_6-0-6

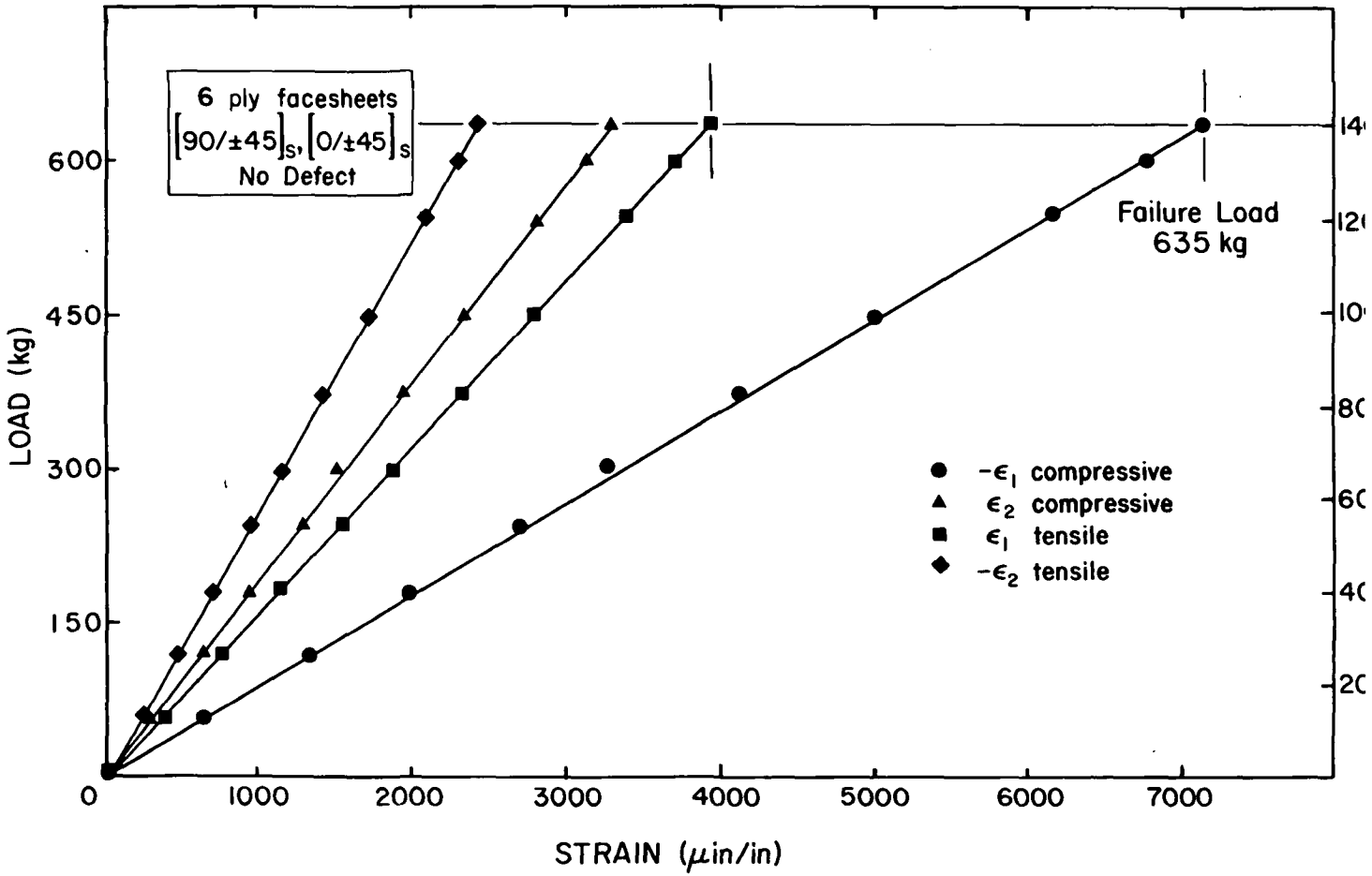

FIGURE C.3 LOAD VS. STRAIN - SAMPLE F_6-0-2

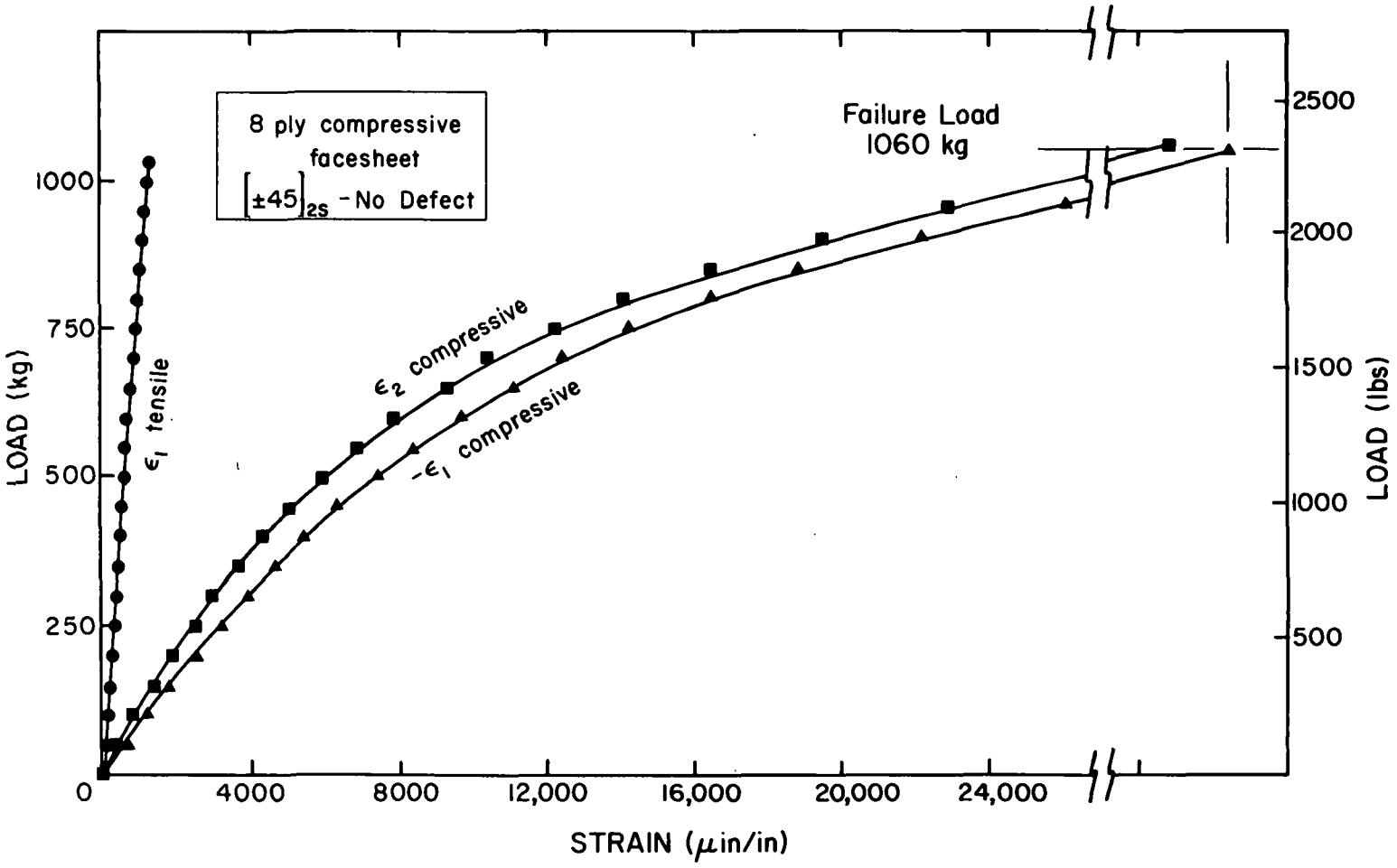

FIGURE C.4 LOAD VS. STRAIN - SAMPLE F_8-0-1

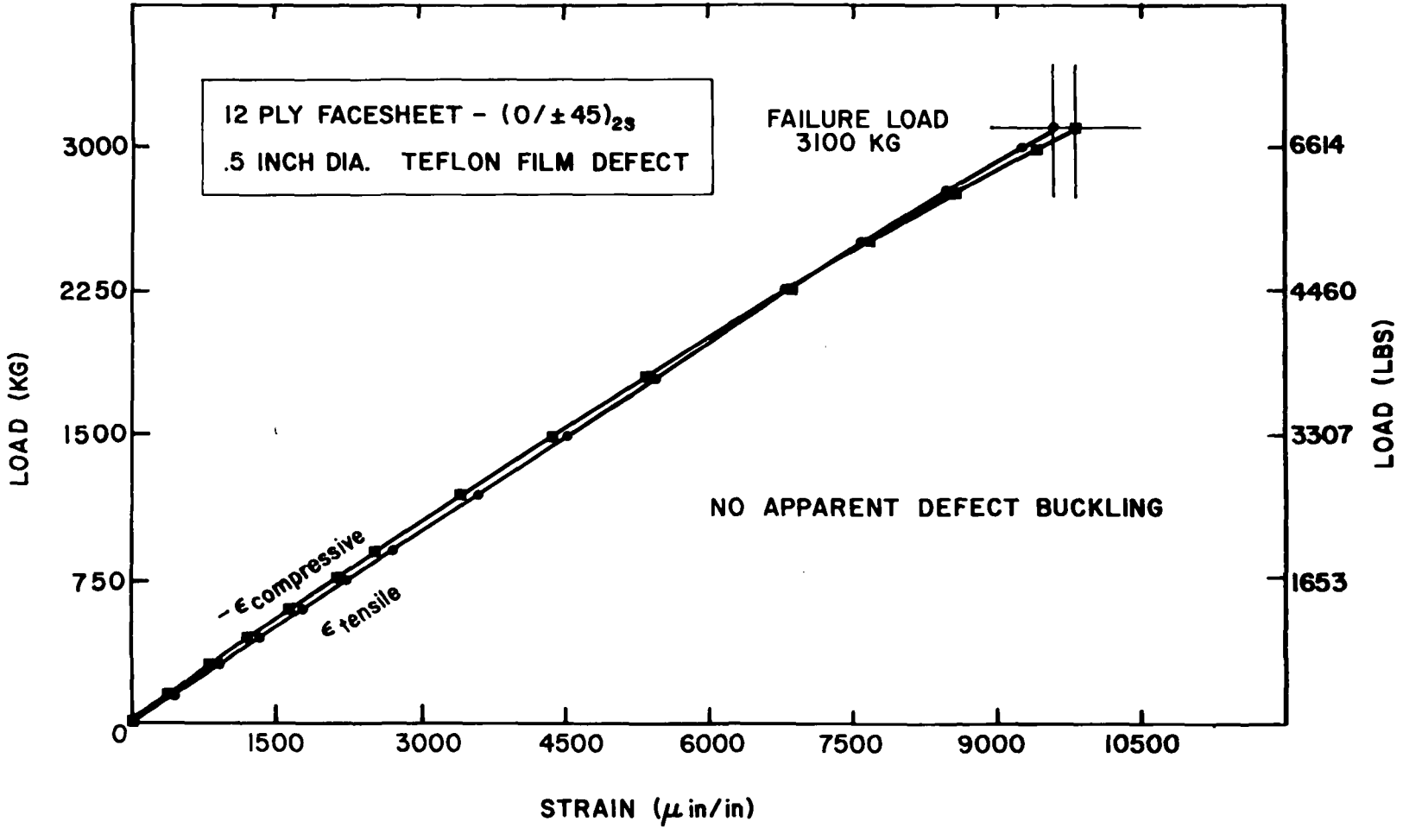

FIGURE C.5 LOAD VS. STRAIN - SAMPLE F_{12}-3-1

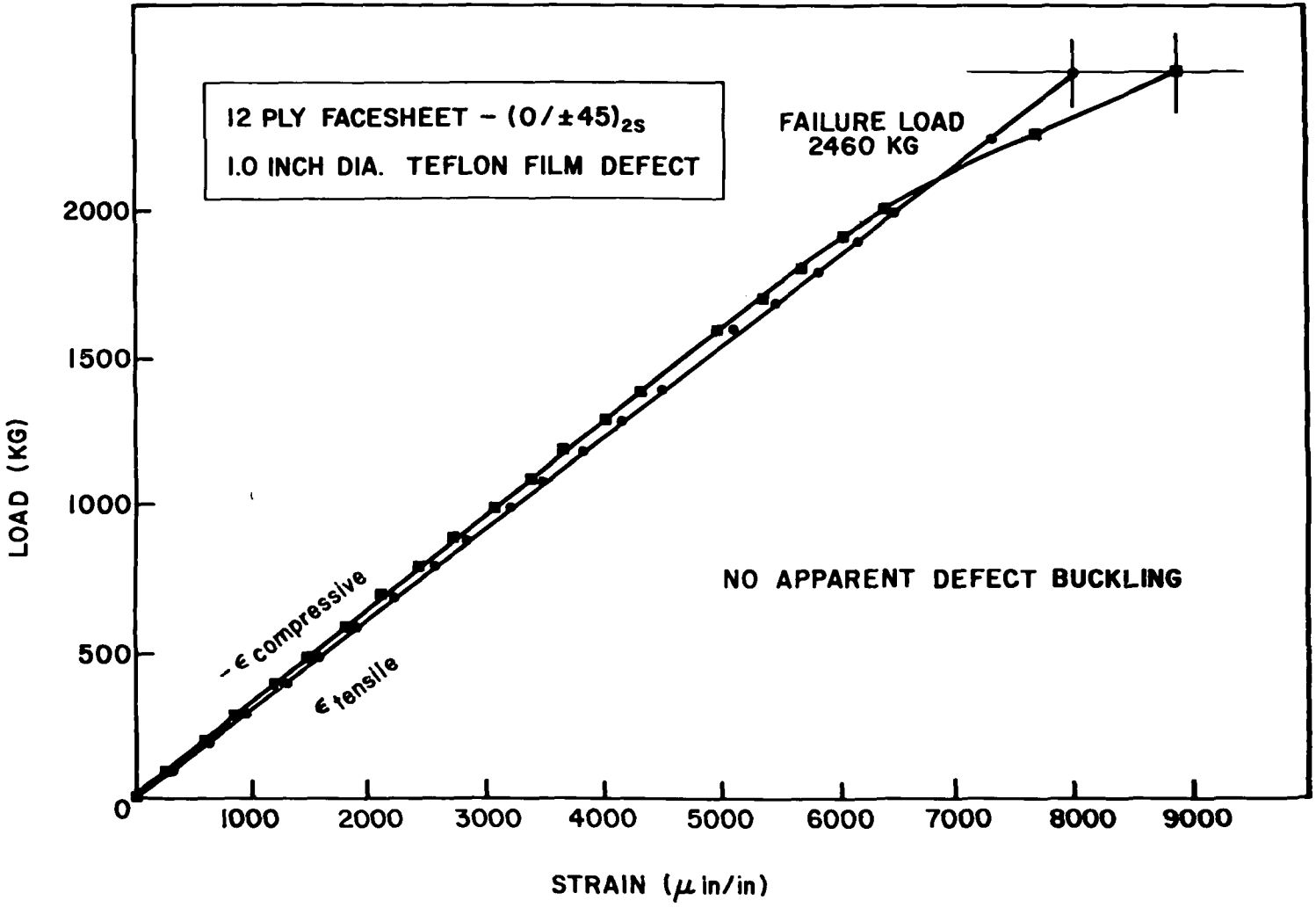

FIGURE C.6 LOAD VS. STRAIN - SAMPLE F_{12}-2-2

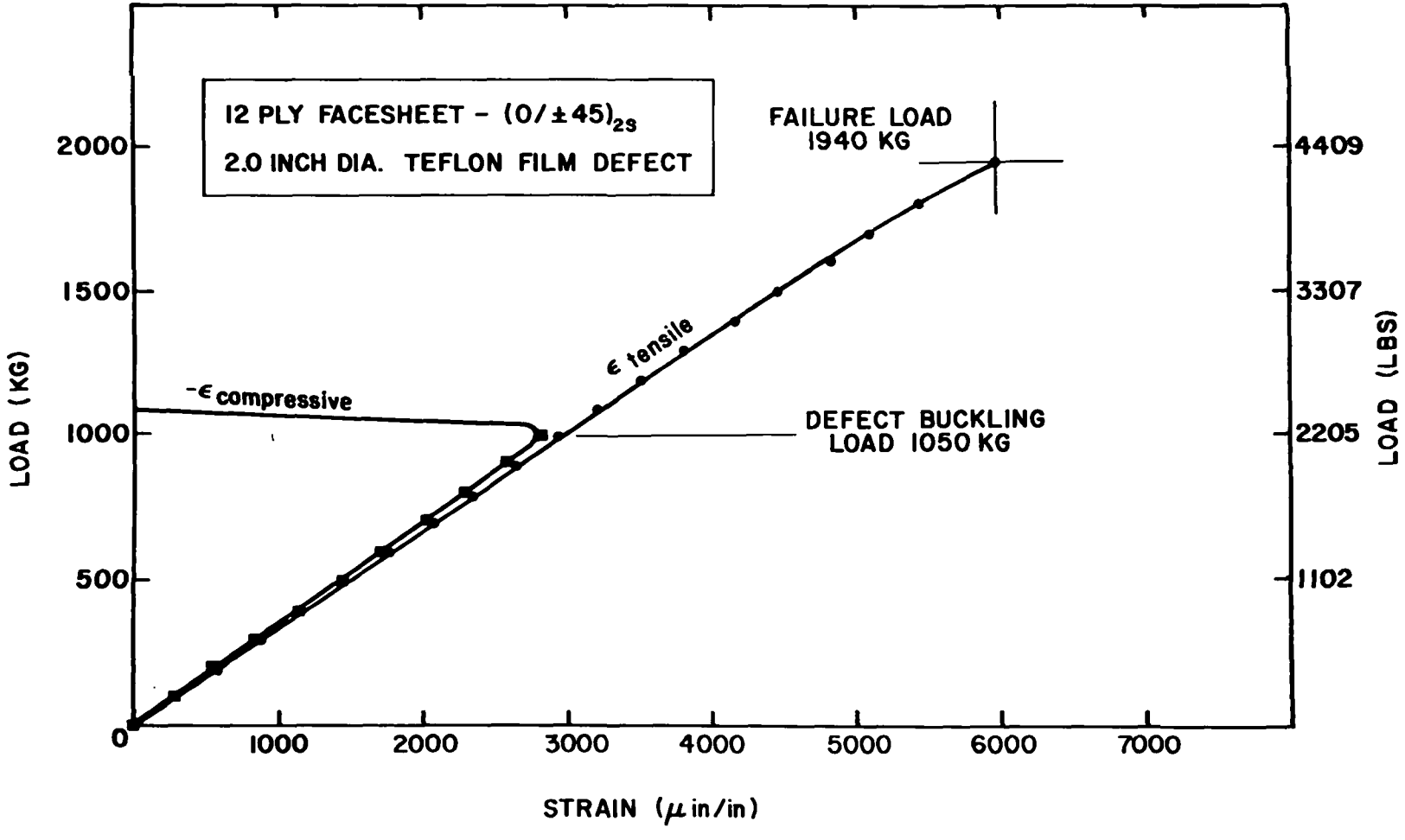

FIGURE C.7 LOAD VS. STRAIN - SAMPLE F_{12}-1-1

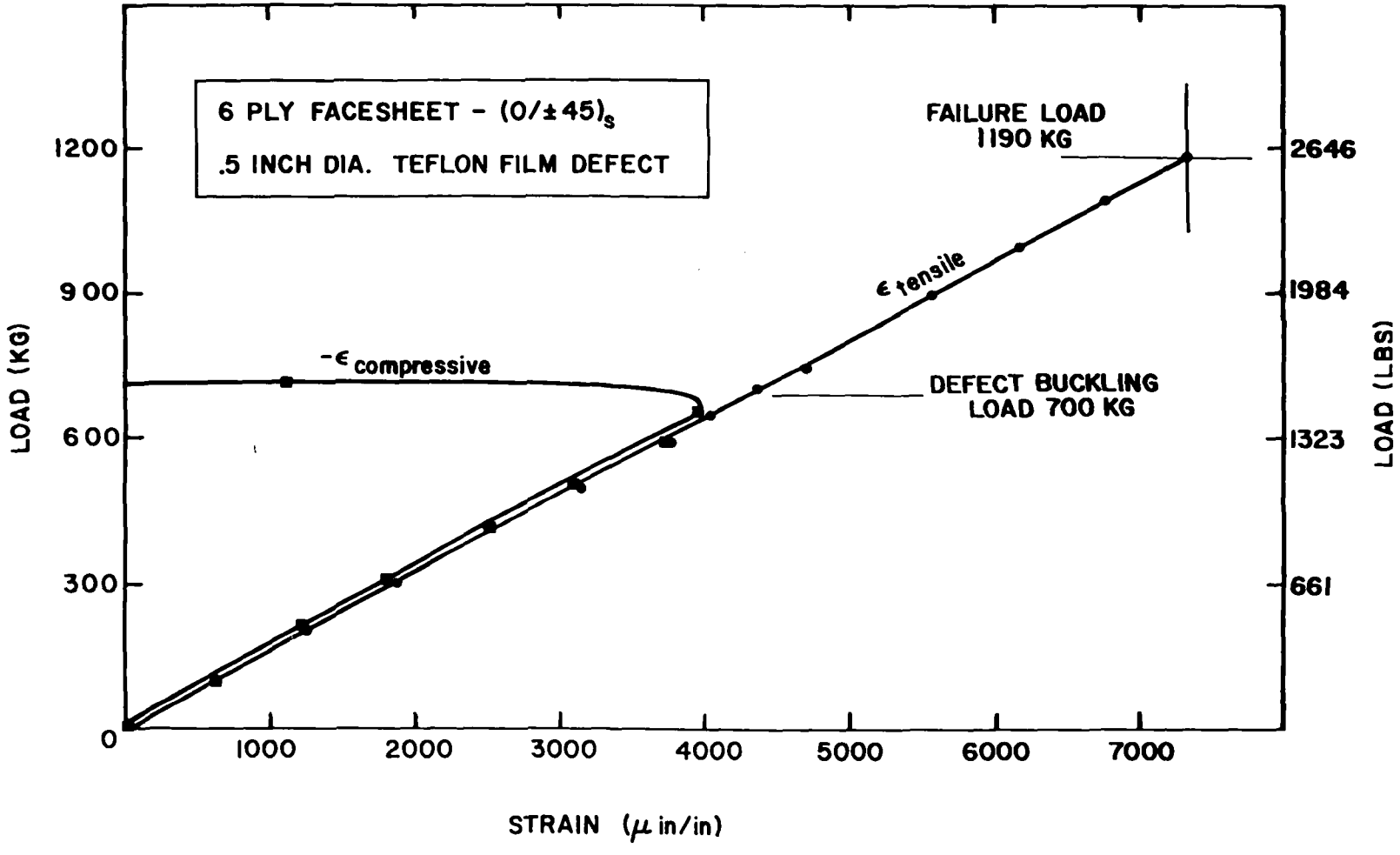

FIGURE C.8 LOAD VS. STRAIN - SAMPLE F_6-1-2

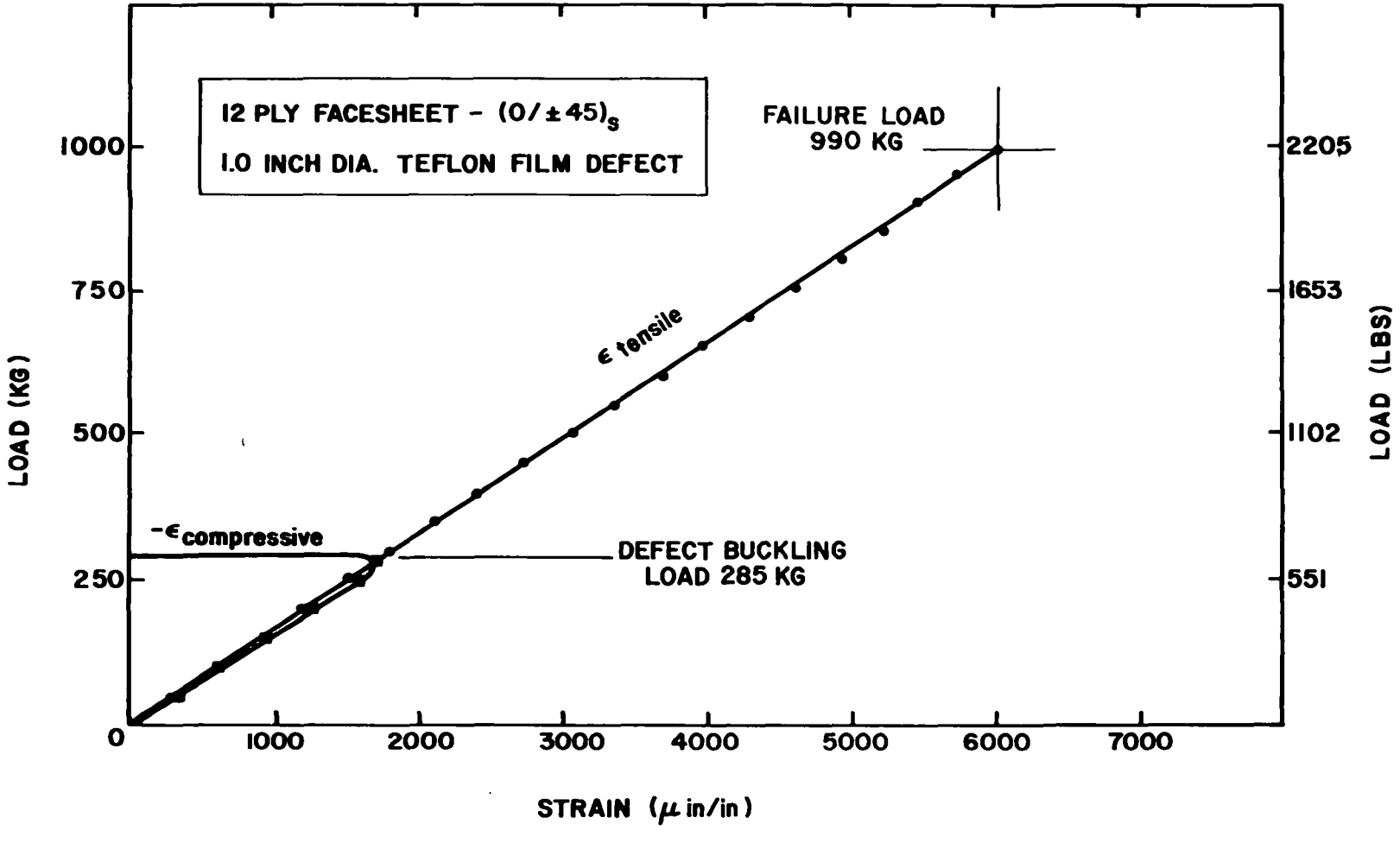

FIGURE C.9 LOAD VS. STRAIN - SAMPLE F_6-2-1

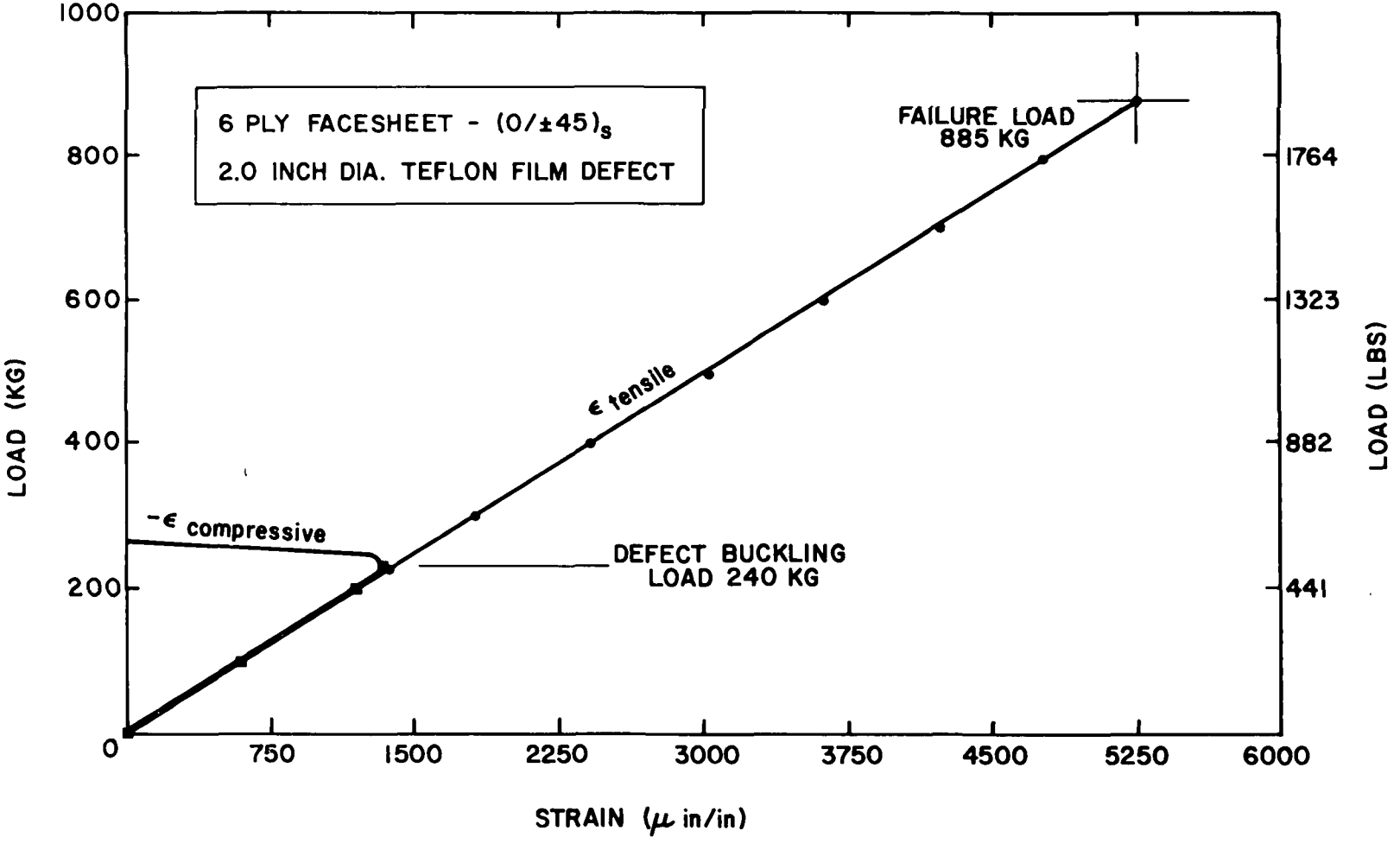

FIGURE C.10 LOAD VS. STRAIN - SAMPLE F_6-3-2

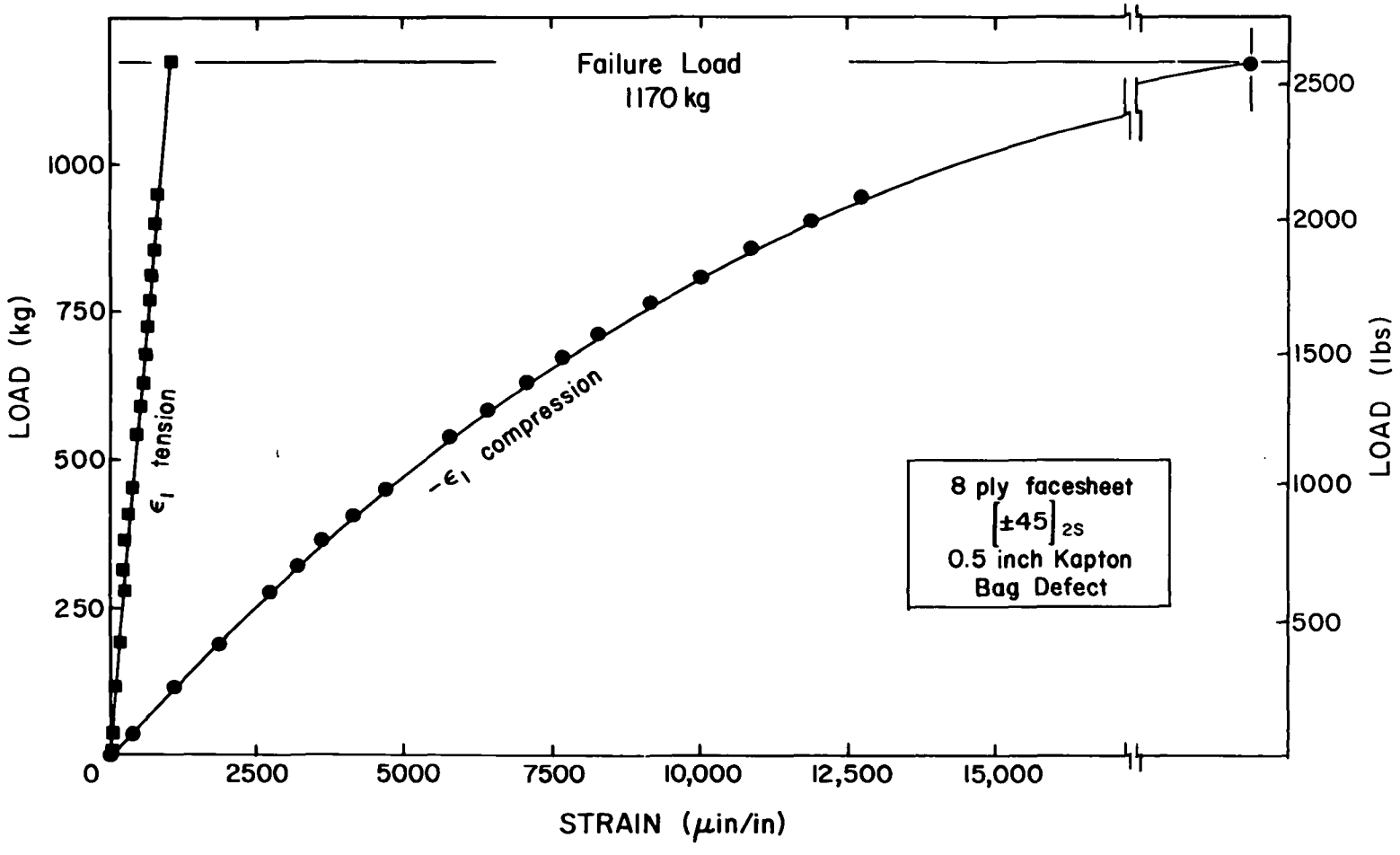

FIGURE C.11 LOAD VS. STRAIN - SAMPLE F_8-4-1

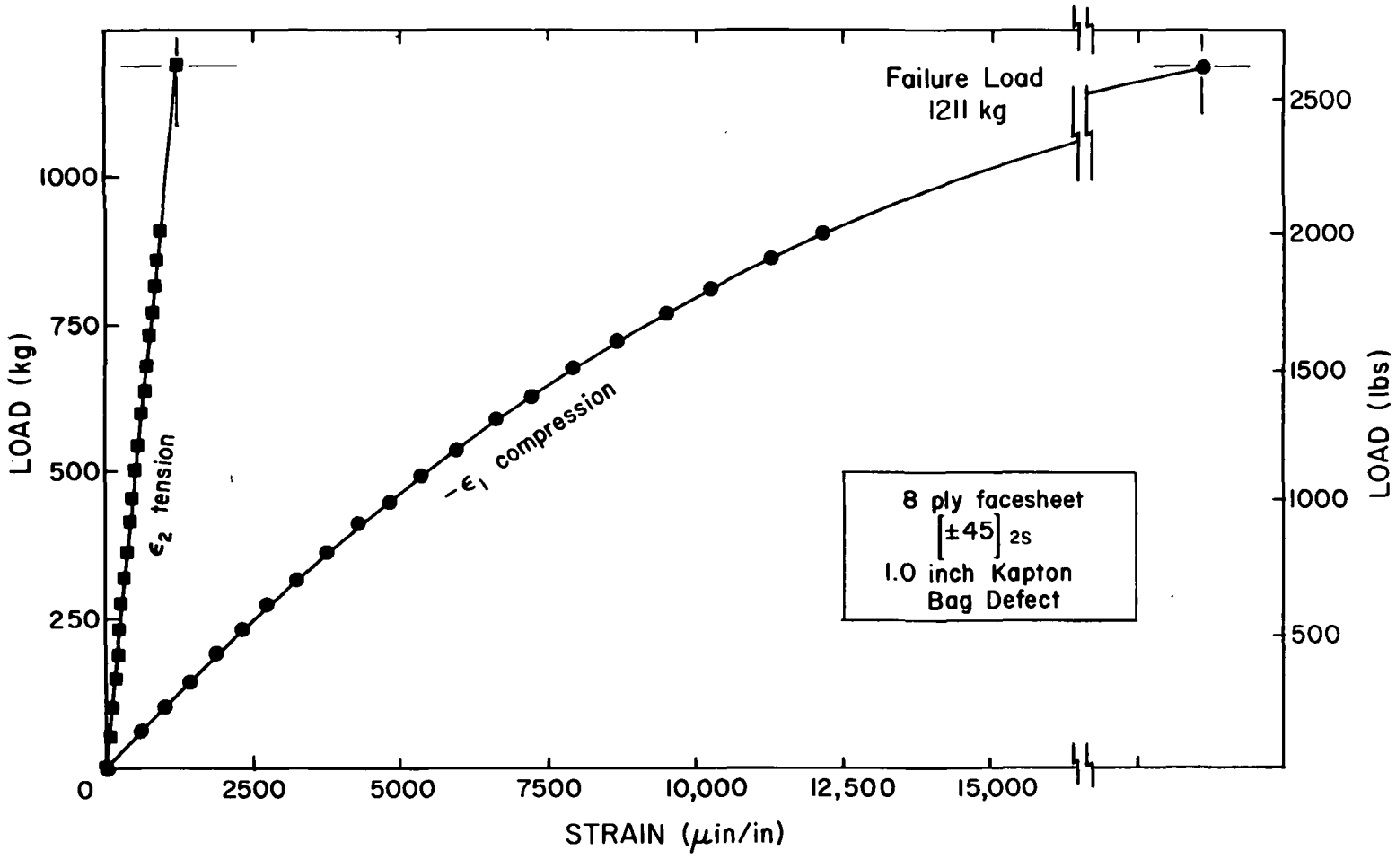

FIGURE C.12 LOAD VS. STRAIN - SAMPLE F_8-5-1

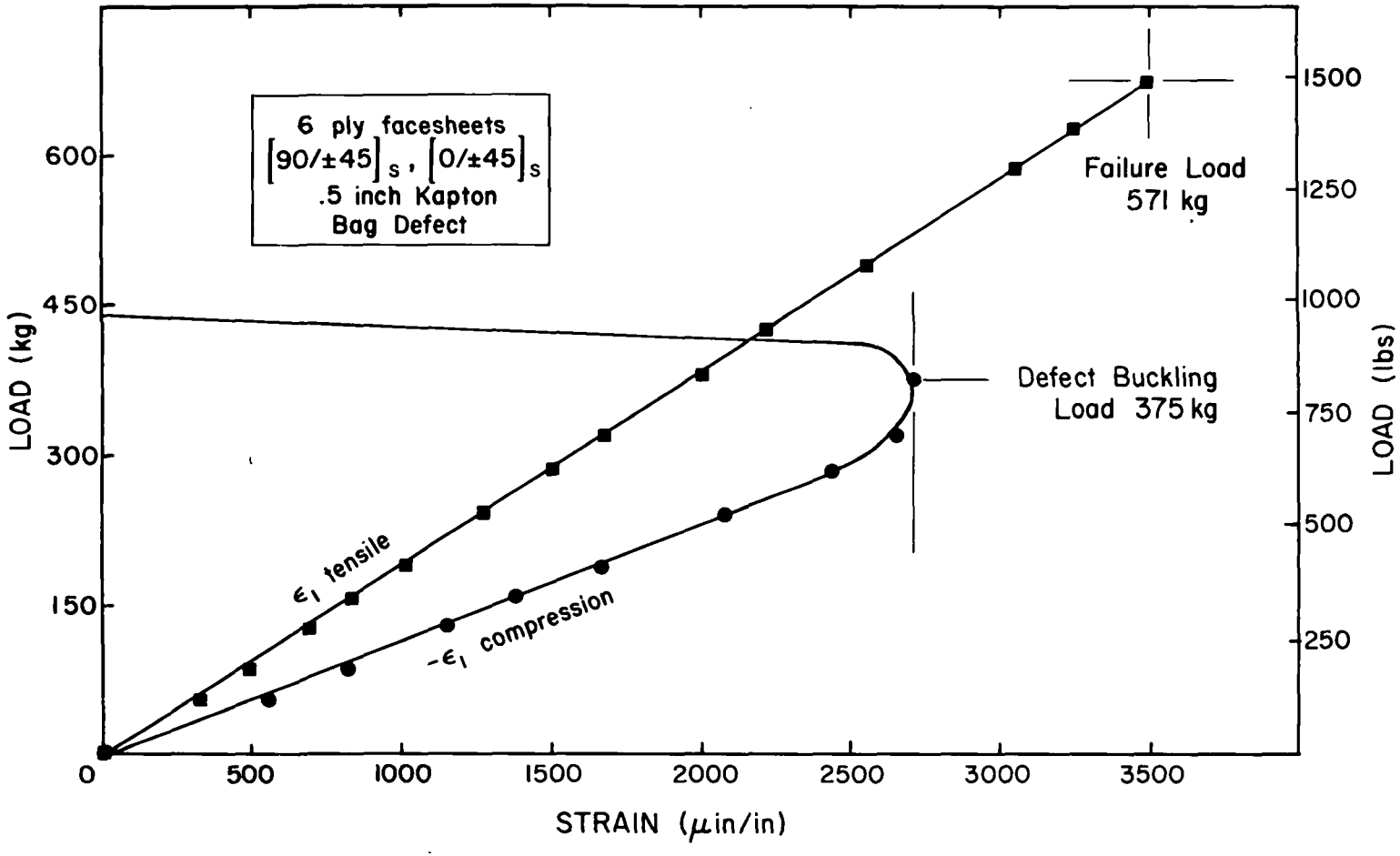

FIGURE C.13 LOAD VS. STRAIN - SAMPLE F_6-4-2

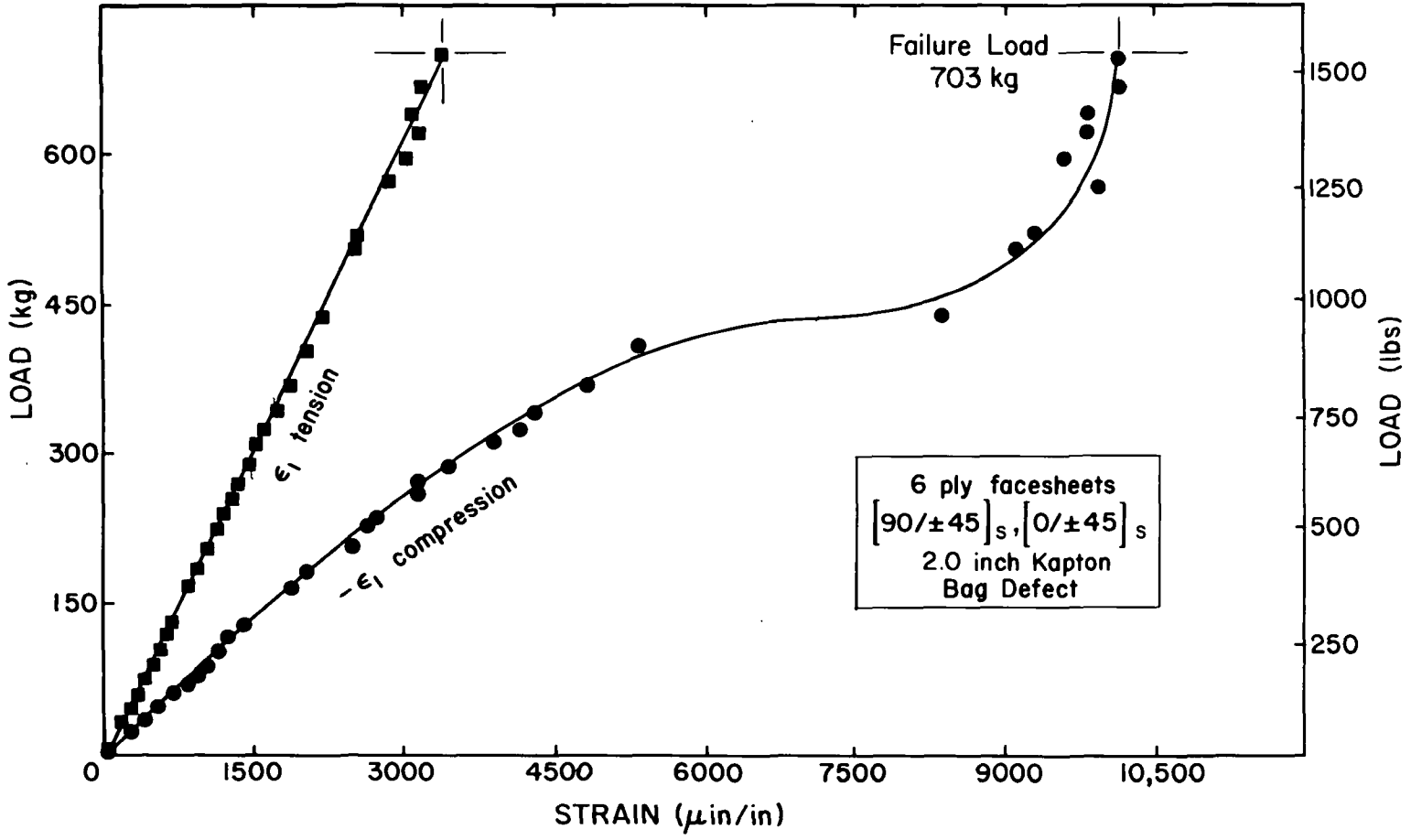

FIGURE C.14 LOAD VS. STRAIN - SAMPLE F_6-6-1

SECURITY CLASSIFICATION OF THIS PAGE *(When Data Entered)*

REPORT DOCUMENTATION PAGE

READ INSTRUCTIONS BEFORE COMPLETING FORM

1. REPORT NUMBER	2. GOVT ACCESSION NO. / 3. RECIPIENT'S CATALOG NUMBER
4. TITLE *(and Subtitle)* Flaw Criticality of Circular Disbond Defects in Compressive Laminates. 1980-81 Interim Report	5. TYPE OF REPORT & PERIOD COVERED 1980-81 Interim Report 6. PERFORMING ORG. REPORT NUMBER CCM-81-03
7. AUTHOR(s) John D. Webster	8. CONTRACT OR GRANT NUMBER(s) NASA Grant 1304
9. PERFORMING ORGANIZATION NAME AND ADDRESS Center for Composite Materials 208 Evans Hall, University of Delaware Newark, DE 19711	10. PROGRAM ELEMENT, PROJECT, TASK AREA & WORK UNIT NUMBERS
11. CONTROLLING OFFICE NAME AND ADDRESS National Aeronautics & Space Admin. Materials Div., Langley Research Center Hampton, VA 23665	12. REPORT DATE June 1981 13. NUMBER OF PAGES 113
14. MONITORING AGENCY NAME & ADDRESS*(if different from Controlling Office)*	15. SECURITY CLASS. *(of this report)* Unclassified 15a. DECLASSIFICATION/DOWNGRADING SCHEDULE

16. DISTRIBUTION STATEMENT *(of this Report)*

Approved for public release; distribution unlimited.

17. DISTRIBUTION STATEMENT *(of the abstract entered in Block 20, if different from Report)*

18. SUPPLEMENTARY NOTES

Report prepared as Thesis for partial fulfilment of the requirements for a Masters in Mechanical and Aerospace Engineering.

19. KEY WORDS *(Continue on reverse side if necessary and identify by block number)*

Composite, Flaw Criticality, Damage Repair, Buckling, Interlaminar Flaw, Graphite-Epoxy

20. ABSTRACT *(Continue on reverse side if necessary and identify by block number)*

Inherent material flaws in composite laminates may result in substantial performance loss. The complex nature of this strength loss is influenced by several parameters including loading, laminate stacking sequence and thickness, flaw size, and defect type. These various effects have not, however, been fully characterized and hence there exists a need for establishing flaw criticality data. An experimental and analytical study of the compressive behavior of T300/5208 graphite/epoxy laminates

DD FORM 1 JAN 73 1473

SECURITY CLASSIFICATION OF THIS PAGE *(When Data Entered)*

20. Abstract (continued)

containing circular delaminations is performed to determine the flaw criticality of two types of implanted defect, Kapton bag and Teflon film, on several laminate configurations: $[0/\pm45]_{2s}$, $[0/\pm45]_{s}$, $[90/\pm45]_{s}$ and $[\pm45]_{2s}$. Defect size is varied and results are presented in the form of residual strength curves. Results indicated that the Teflon film defect reduced strength more than the Kapton bag defect in the 12-ply samples, but that two laminates, $[\pm45]_{2s}$ and $[90/\pm45]_{s}$ were insensitive to any implanted defect. A clear thickness effect was shown to exist for the $[0/\pm45]_{ns}$ laminate and was attributed to failure mode transition. The analytically predicted buckling loads show excellent agreement with experimental results and are useful in predicting failure mode transition.